



February 2011 V2.1

## **TROPISAR 2009**

# **TECHNICAL ASSISTANCE FOR THE DEVELOPMENT OF AIRBORNE SAR AND GEOPHYSICAL MEASUREMENTS DURING THE TROPISAR 2009 EXPERIMENT**

Prepared for  
European Space Agency  
Centre National d'Etudes Spatiales

## **FINAL REPORT**

Prepared by  
ONERA /Departement Electromagnétisme etRadar  
and  
Université Paul Sabatier/ CESBIO  
and  
Université Paul Sabatier/ Evolution et Diversité Biologique  
and  
CIRAD , UMR « Ecologie des Forêts de Guyane »

February, 17th 2011  
Version 2.1



## ESA/CNES STUDY CONTRACT REPORT : TROPISAR – FINAL REPORT

**ESA contract N° 22446/09**
**CNES contract N° 92929 03/08/09**
**Subject**
**FINAL REPORT**
**Contractors**
**ONERA-CESBIO- EDB**

### Abstract:

The TropiSAR campaign was conducted in French Guiana in the summer 2009 in the framework of the Phase A studies pertaining to the BIOMASS mission, one of the three for Earth Explorer candidates. Its main objectives were the evaluation of P-Band radar imaging over tropical forests for biomass and forest height estimation.

An extensive in-situ database, acquired over several decades, was made available by the Guyafor Project. Two main forest sites have been studied: Nouragues and Paracou. New plots were identified and measured under this contract. All together, the dataset includes 157 ha of forest plots, for which all trees with a diameter larger than 10cm have been tagged, positioned and measured. This totals more than 98000 trees. Over these plots, the biomass ranges from 10t/ha for a Coco plantation to 490t/ha for a plot of undisturbed forest.

Seven SAR flights were conducted with the SETHI system from ONERA during the 23 days of the SAR campaign which lasted from August 10<sup>th</sup> to September 1<sup>st</sup> 2009. The selected waveform is characterised by P and L simultaneous acquisitions with a range resolution of around 1.5m. During these flights, a temporal dataset characterised with a zero spatial baseline was acquired to allow the quantification of the temporal decorrelation, one key parameter for the performance evaluation of the PolInSAR technique in a single-satellite configuration. A PolInSAR and tomographic database was also acquired with vertical baselines of 50, 100, 150, 200 and 250 feet.

The processing of the SAR data included a crosstalk removal step at P-Band resulting from a double bounce effect on the wings. The overall calibration accuracy was found to be  $\pm$ :-0.5db, with a NE sigma0 better than -30dB and a cross-talk level better than -25dB. The geometric accuracy of the SAR data was measured to be better than 10m, which is the level of accuracy of the reference points used in the evaluation.

The in-situ error analysis identified three main sources of error in the in-situ measurements: the error in the field measurements, the error in the allometry and the error linked to the size of the measured plot. The field measurements (mostly DBH) are precise and are not contributing significantly to the error in the biomass estimations. The allometric equation is the major source of uncertainty and it was evaluated to be around 5%. The plot size is of major importance and the estimation accuracy for a plot size of 1 ha is estimated to be 10%. This uncertainty drops to 5% if the plot size exceeds 4 ha. Furthermore, the in-situ biomass estimation does not include the small trees (diameter less than 10cm), the lianas and the dead trees. This creates a bias estimated to be of the order of 10%.

The TropiSAR backscatter coefficients have been analyzed in terms of polarimetric, temporal and incidence behavior. The following observations were made on the Paracou test site:



- The high correlation between polarized backscatter coefficients, at HH, VV and HV polarizations denote the specific scattering mechanisms of tropical forests as compared to boreal or temperate forests previously under study.
- The backscatter coefficients were observed to have a high temporal stability during the campaign.
- The effect of elevation angle of these dense medium is better compensated by a new normalized coefficient  $\alpha^0$ , as compared to the classical  $\gamma^0$ .
- The topographic effect needs to be accounted for. In the absence of DEM whose resolution is compatible with the SAR data spatial resolution, interpolated SRTM DEM can be used to correct for the topography.
- The relationships between the backscattering coefficients  $\alpha^0_{HV}$  with in situ biomass are in good agreement with the trend derived from previous experiments in other forest sites (temperate, boreal). However, the sensitivity to biomass in the high range of biomass (300 t/ha) is relatively small, and this requires appropriate analysis and processing prior to biomass inversion.
- The preliminary inversion using HV backscattering coefficients has provided mapping results with RMSD of less than 20%.
- The combination of different SAR measurements derived from intensity and PolInSAR, e.g. using a Bayes inversion approach, was found to improve the inversion performance.

The PolInSAR analysis dealt with two different aspects, the temporal decorrelation analysis and the PolInSAR vegetation height estimation. The following conclusions were reached:

- The loss of coherence due to temporal baseline was shown to be small even after 22 days. We observed for one date a more pronounced loss of coherence certainly linked to weather conditions with a recovery in the coherence for the later dates. The coherence variation with respect to temporal baseline is not monotonously decreasing.
- The PolInSAR height inversion based on a single baseline approach was evaluated against the LiDAR derived canopy height model. The overall behaviour of the estimator is good with a RMS error of 5m with zero bias. The attenuation coefficient, which in the case of a single baseline inversion at P-band needs to be set (in tropical forest 0.4dB/m) is shown to have little effect on the inversion. A proper selection of the baseline is essential for good estimation.

As a summary, the preliminary analysis of the TropiSAR has shown that it is possible to retrieve biomass of the dense tropical in French Guiana, using appropriate data analysis and inversion approaches. Current works are undertaken to analyze the data of the Nouragues test site, and to derive information on PolInSAR and tomography which can be used to improve the inversion results.

<b>Name of the authors:</b> P Dubois-Fernandez ONERA T le Toan CESBIO J Chave EDB L Blanc ECOFOG	S Daniel ONERA H Oriot CESBIO A Arnaubec ONERA-Fresnel M Réjou-Méchain EDB	L Villard CESBIO Y Lasne CESBIO T Koleček CESBIO/CNES
<b>Name of Study Manager:</b> Malcolm Davidson ESTEC Selma Cherchali CNES		<b>ESA budget heading</b>

# TROPISAR-FINAL REPORT

ESA CONTRACT N° 22446/09/NL/CT  
CNES CONTRACT N° 92929 03/08/09



-4-




February 2011 V2.1





## TROPISAR FINAL REPORT

Tuesday, February 15th

Name	Project Manager	Test Site Coordinator	Data Analysis Coordinator
	P Dubois-Fernandez ONERA	J Chave and L Blanc EDB / ECOFOG	Thuy le Toan CESBIO
Signature			
	GEN-F45-4(GEN-CLI-001)		

Office National d'Études et de Recherches Aérospatiales



The authorship of this report are listed below :

Pascale Dubois-Fernandez	SAR measurements, processing, calibration, PolInSAR
Sandrine Daniel	SAR processing, calibration, PolInSAR analysis
Thuy Le Toan	Polarimetric analysis
Ludovic Villard	Polarimetric analysis
Yannick Lasne	Polarimetric analysis
Thierry Koleček	Polarimetric analysis
Jérôme Chave	In-situ measurements and error analysis
Lilian Blanc	In-situ measurements and error analysis
Maxime Réjou-Méchain	In-situ measurements and error analysis
Hélène Oriot	SAR processing, calibration
Aurélien Arnaubec	PolInSAR analysis



## TABLE OF CONTENT

<b>1. INTRODUCTION .....</b>	<b>12</b>
1.1. Campaign Objectives .....	13
1.2. Campaign institutions.....	14
1.3. Campaign participants.....	15
<b>2. OVERVIEW OF THE CAMPAIGN.....</b>	<b>16</b>
2.1. The forest test sites .....	16
2.2. The different geodesic system in French Guiana .....	17
2.3. Digital elevation model of the areas.....	19
<b>3. TROPISAR AIRBORNE SAR ACQUISITION .....</b>	<b>23</b>
3.1. SAR data acquisition schedule .....	23
3.2. The SETHI SAR system and acquisition radar parameters .....	23
3.3. SAR data acquisition flight description .....	28
3.4. Processing workflow .....	32
<b>4. FOREST SITE DETAILED DESCRIPTION AND GROUND MEASUREMENTS.....</b>	<b>47</b>
4.1. General description of Nouragues and Paracou .....	47
4.2. Tree measurements and inventories .....	52
4.3. Weather conditions.....	53
4.4. Soil moisture data.....	54
4.5. LiDAR data .....	56
4.6. Illustrations.....	57
<b>5. TROPISAR DATASET .....</b>	<b>63</b>
5.1. Ground measurement data set .....	63
5.2. Radar dataset .....	64
5.3. Description of the summary file.....	76
<b>6. TROPISAR DATA ANALYSIS – GROUND MEASUREMENTS – ERROR ANALYSIS .....</b>	<b>77</b>
6.1. Methods for above ground biomass estimation.....	77
6.2. Above-ground biomass in the ground plots .....	80
6.3. Discussion and perspectives.....	81
<b>7. TROPISAR DATA ANALYSIS – POLSAR ANALYSIS.....</b>	<b>83</b>
7.1. Extraction of the backscattered intensities from SETHI data .....	83
7.2. Analysis of the backscattering coefficients of the reference plots .....	90
7.3. Relation with in-situ biomass .....	95



7.4. Preliminary biomass inversion mapping .....	101
7.5 Summary and current works .....	106
<b>8. TROPISAR DATA ANALYSIS – POLINSAR ANALYSIS.....</b>	<b>108</b>
8.1. Temporal decorrelation analysis .....	108
8.2. Forest height inversion result validation from PolInSAR data .....	111
<b>9. CONCLUSIONS.....</b>	<b>129</b>
<b>10. REFERENCES .....</b>	<b>130</b>
<b>11. ACKNOWLEDGMENTS .....</b>	<b>134</b>
<b>ANNEX A: GEOGRAPHIC AND IMAGE COORDINATES FOR THE REGIONS OF INTEREST.....</b>	<b>136</b>
<b>ANNEX B: TROPISAR SAR DATA FORMAT .....</b>	<b>146</b>
<b>ANNEX C: BACKSCATTER INTENSITIES VERSUS IN-SITU BIOMASS.....</b>	<b>157</b>
<b>ANNEX D: ARBORESCENCE OF THE SAR DATABASE .....</b>	<b>160</b>



## FIGURES

Figure 2-1: The overall location of the different sites imaged during the TropiSAR campaign 16

Figure 2-2: SRTM DEM over French Guiana. The coordinates of the upper left corner are: Lon = -56.000 & Lat=7.000. The coordinates of the lower right corner are: Lon = -52.000 & Lat= 1.000. The color scale ranges between [-100m , 300m].....19

Figure 2-3: Paracou site: the upper left coordinates are E[m], N[m], 279844., 605120., lat, long -52.912083, 5.2437500; Lower right corner E[m], N[m], lon,lat : 288078 , 579931, -52.987083, 5.4712500. The reference for height is the NGG77 with a sea level reading at 0m. The color scale ranges [-5m, 65m]. The precise LiDAR DEM was inserted into the SRTM DEM on the right image. The overall structures are kept. However, there is a height difference between both DEM of around 30m. On the right, a histogram of the DEM over the studied site.....20

Figure 2-4: Height difference between SRTM and the LiDAR derived DEM over the Paracou site. The color scale ranges [0m ,40m], The difference is certainly linked to the vegetation height.....21

Figure 2-5: Nouragues site: the upper left coordinates are E[m], N[m]: 310000, 455000; Lower right corner E[m], N[m], 32000, 440000. The reference for height is the NGG77 with a sea level reading at 0m. The color scale ranges [0m, 400m]. The precise LiDAR DEM was inserted into the SRTM DEM on the right image. The overall structures are kept. However, there is a height difference between both DEM of around 30m. On the right, a histogram of the DEM over the studied site. ....21

Figure 2-6: Height difference between SRTM and the LiDAR derived DEM over the Nouragues site. The color scale ranges [0m ,60m], The difference is certainly linked to the vegetation height. ....22

Figure 3-1: The Falcon 20 carrying the SETHI system. The two pods contain the radar antennas.....24

Figure 3-2: The left pod containing the P-Band and the L-Band antennas.....25

Figure 3-3: The right pod containing the L band antenna and the two X band antennas. ....25

Figure 3-4 : Example of a dataset over the Marais de Kaw with a color composite image at P-band.....26

Figure 3-5: SETHI L- and P-band acquisition geometry.....26

Figure 3-6: Paracou image coverage: Note that tropi0506 extends significantly to the North...30

Figure 3-7: Nouragues SAR data coverage. Three different lines were acquired over Nouragues. They are identified on this figure.....31

Figure 3-8: The Arbocel site is close to the Paracou one.....31

Figure 3-9: The coverage of the SAR data acquisition over the Kaw area.....32

Figure 3-10: Quegan's parameter  $\alpha$  as a function of range in the X axis, and frequency Y axis on the TropiSAR data.....34

Figure 3-11: Quegan's parameter  $v$  estimated over range before aircraft-attitude compensation (left image) and after aircraft-attitude compensation (right images). The different curves correspond to different data with different aircraft attitudes. ....35

Figure 3-12: Computing the geographic position of the i,j,h pixel. First identifying the upper and lower layers, then on both layers, from the four corner points, compute the geographic



position of the point located at the center of the face, then interpolate between these two points.....	37
Figure 3-13: The 5 reference targets T1, T2, T3, T4, T5 and Dr. ....	38
Figure 3-14: The setup for the reference targets. T1 is in the near range while T5 is in the far range.....	39
Figure 3-15: Radar image of the calibration site Rochambeau airport. ....	39
Figure 3-16 : Radar cross section responses over the trihedral in HH polarisation and VV polarisation at P Band. ....	40
Figure 3-17: Radar cross section responses over the trihedral in HH polarisation and VV polarisation at L-Band.....	41
Figure 3-18: P-Band ,NEsigma0 analysis , Image , Range profile, NE sigma0 histogram. ....	43
Figure 3-19: L-Band, NEsigma0 analysis , Image , Range profile, NE sigma0 histogram. ....	43
Figure 3-20: Polarisation isolation levels at P band.....	44
Figure 3-21: Polarisation isolation levels at L band.....	45
Figure 3-22: IGN orthophoto of Paracou allowing a precise geo localization. ....	46
Figure 3-23: Tropi0509_Pprop8Hh_proj_wgs84.dat.....	46
Figure 4-1: Location of the Nouragues and Paracou Research Stations in French Guiana. ....	48
Figure 4-2: Localization of the 5 plots at the Nouragues research station.....	49
Figure 4-3: Location of the Paracou permanent plots and additional plots established for the TropiSAR project.....	51
Figure 4-4: Rain fall, Air moisture and air temperature in Nouragues. ....	53
Figure 4-5: Air temperature, rainfall and air moisture at Paracou during the TropiSAR campaign. ....	54
Figure 4-6: Calibration curve for the soil moisture measurement. ....	55
Figure 4-7: Soil moisture content in Paracou.....	56
Figure 4-8: Forest view from the Inselberg.....	57
Figure 4-9: Grand Plateau Area (Note the lianas and the Chablis area). ....	58
Figure 4-10: Petit Plateau area. ....	59
Figure 4-11: Plot 6 (no Treatment) ; Vouacapoua americana on the right. ....	60
Figure 4-12: Bois cathédrale (Chimarrhis turbinata) on Plot 1, Plot 15 and Plot 11. ....	60
Figure 4-13: Plot 9, Plot 2, Plot 2, (Treatment 1). ....	61
Figure 4-14: Plot 10 (Treatment 2). ....	61
Figure 4-15: Plot 12 with a Cecropia tree, pioneer species in the left picture (Treatement 3). ..	62
Figure 4-16: Plot 4 (Treatment 3). ....	62
Figure 5-1: Example of map that illustrates the variation in space in biomass (tons per ha) at different spatial resolution (25 × 25 m, 50 × 50 m, 100 × 100 m). Similar maps have been provided to the TropiSAR project for each plot.....	63
Figure 5-2: Example of the text file based on the ROI_Nouragues1_tropi0201_Pcons.....	67
Figure 6-1: Steps of above ground biomass estimation and their bias and/or errors associated.	78
Figure 6-2: Histogram of the AGB values in the 624 0.25-ha subplots.....	79
Figure 6-3: Errors associated to the sampling size in percent (CV). ....	80
Figure 7-1: Geometry of the backscattering from a forest canopy. The figure explains the volume normalization used in the definition of $\alpha^0$ (Equation 7.8).....	85
Figure 7-2: Illustration of the dependency of the scattering volume on the elevation angle defined. The use of this volume as a normalization factor leads to the definition of the backscattering coefficient $\alpha^0$ .....	86





- Figure 7-3:  $\beta^0$  and  $\gamma^0$  images of the Paracou region, corresponding to the "tropi0007\_Pcons\_Hv\_slc" files. Red line: across range transect where backscatter profiles are analyzed in Figure 7-5.....86
- Figure 7-4:  $\beta^0$  and  $\gamma^0$  images of the region of Nouragues, corresponding to the "tropi0101\_Pcons\_Hv\_slc" files. Red line: across range transect where backscatter profiles are analyzed in Figure 7-6.....87
- Figure 7-5: Range profiles of backscattering coefficient  $\beta^0$ ,  $\gamma^0$  and  $\alpha^0$  from a transect in Figure 7-3 on the image from "tropi0007\_Pcons\_qp\_slc" over Paracou. HH, VV and HV are respectively in red, blue and green colour. The coefficients are computed using spatial averaging over windows of 60 x 4 pixels respectively in azimuth and range. The profile size is reduced from 4000 to 1000 (x axis). .....88
- Figure 7-6: Range profiles of backscattering coefficients  $\beta^0$ ,  $\gamma^0$  and  $\alpha^0$  from a transect in Figure 7-4 on the image from "tropi0007\_Pcons\_qp\_slc" over Nouragues. HH, VV and HV are respectively in red, blue and green colour. The coefficients are computed using spatial averaging over windows of 60 x 4 pixels respectively in azimuth and range. The profile size is reduced from 4000 to 1000 (x axis). .....89
- Figure 7-7: Radar backscattering coefficient expressed in  $\sigma^0_{HH}$  as function of  $\sigma^0_{VV}$  (top) and  $\sigma^0_{HV}$  (bottom) corresponding to the 16 stands of the Paracou test site, at different acquisition dates. ....94
- Figure 7-8: a (top) 90m SRTM DEM over the Paracou test site, and b (bottom), interpolated SRTM DEM at 30m resolution (color scale for the elevation is between 0 and 125 m)...97
- Figure 7-9: Angle images derived from the SRTM DEM and used in the topographic correction. From left to right, angle with the vertical, local incidence angle and angle ' $\psi_v$ ' defined above. ....98
- Figure 7-10: The HV backscattering coefficients, expressed in  $\alpha^0$ , as a function of biomass for the 15 reference plots of 250 m x 250 m in the Paracou site. For each data point, the number denotes the number of the plot. The curve is the relationship between  $\gamma^0_{HV}$  and biomass established from multiple datasets [Le Toan et al., 2010]. RMSD = Root Mean Squared Difference, MPE= Mean percentage error,  $r_P$  and  $r_S$  are Pearson and Spearman coefficients. ....100
- Figure 7-11: HV backscattering coefficients, expressed in  $\gamma^0$  from the Landes forests [Le Toan et al., 1992], Remningstorp forest [Sandberg et al., 2010] and La Selva forest [Saatchi et al., 2010] and expressed in  $\alpha^0$  at the Paracou test site. The pink curve is the relationship between  $\gamma^0_{HV}$  and biomass established from multiple datasets [Le Toan et al., 2010]. The dashed blue curves materialize 20% of error in biomass. ....100
- Figure 7-12: Retrieved biomass versus in situ biomass of the plots in Paracou, from inversion of  $\alpha^0_{HV}$  using the topographic correction derived from SRTM DEM. ....102
- Figure 7-13: Biomass map of the Paracou site, obtained by inversion of  $\alpha^0_{HV}$  (corrected with the SRTM DEM) using a window of 15 x 15 pixels at the top (a) and 25 x 25 pixels below (b). White values are either non estimated (masked with the 600 t/ha threshold) or zero biomass regions. ....103
- Figure 7-14: Relationship between the Pol-InSAR indicator  $\Phi$  and the in-situ biomass. ....105
- Figure 7-15: Comparison of the in situ biomass and the biomass retrieved based on Bayes inversion of  $\alpha^0_{HV}$  and the Pol-InSAR indicator  $\Phi$ . ....106
- Figure 8-1: Interferometric coherence image for HH, HV and VV channels between tropi0007 and tropi0104, tropi0208, tropi0305, tropi0402, tropi0503, tropi0603, scaled between 0





and 1 for 6 time intervals (2 days, 4 days, 7 days, 14 days, 20 days, 22 days) The red box indicates the area which was explored in the histogram analysis. ....	108
Figure 8-2: Image of the kz or ( $2\pi/H\alpha$ ) for the six interferometric images presented in Figure 8-1. ....	108
Figure 8-3: Histogram of the interferometric coherence corresponding to the red box in the interferograms presented in Figure 8-1. ....	109
Figure 8-4: Soil moisture measured in the Paracou site. The green dots represent the seven acquisition flights. Flight 4 was acquired after a rain event and correspond to a 14 day delay with respect to Flight 0. ....	109
Figure 8-5: Illustration of the indicators –Ro_0 (red dot) is the most populated bin, Ro_1 (blue dot) and Ro_2 (green dot) correspond to the coherence for 1/2 the population of the max. ....	110
Figure 8-6: Interferometric coherence circle for an area inside the ROI 16. ....	114
Figure 8-7: LiDAR derived DEM (color bar =[0,40m]), radar image [HH,V,VV], LiDAR derived canopy height (color bar =[0,60]) Note that the topography is marked and that the vegetation height is mostly between 25 and 35 m. ....	115
Figure 8-8: Over the study area, the slope image - color bar=[-10°,30°], the altitude of ambiguity - color bar=[40m,80m], the interferometric coherence (HH,HV,VV). ....	115
Figure 8-9: PolInSAR estimated vegetation height maps over the study zone (color bar=[20,45m]) for three attenuation coefficients 0.3dB/m, 0.4dB/m and 0.5dB/m. ....	116
Figure 8-10: A 2-D histogram comparing the PolInSAR height obtained with 2 different attenuation coefficients, 0.4 dB/m and 0.5dB/m. There is a 0.8m bias and a 0.16m RMS between the two estimations. The red line is the 1:1 line. ....	117
Figure 8-11: PolInSAR vegetation height map from 100 feet vertical baseline on the left, 150feet vertical baseline on the right. The altitude on ambiguity is between 61 and 76m on the left and is between 32 and 49m on the right. The color bar ranges from 0 to 60m. ...	118
Figure 8-12: 2D histogram between the vegetation estimated heights from tropi0404 and tropi0405. The two axis range between 0 and 60m. The color indicates the population of the 3D histogram with the red color corresponding to the most populated bin. ....	119
Figure 8-13: Remark about the projection of tree height into the radar geometry. One should take into account the ground height + vegetation height to match the foreshortening observed in the radar image. ....	120
Figure 8-14: LiDAR data: top row : Filter 1 (max) with a 3x3 box, Filter 1(max) with a 19x19 box, bottom row: Filter 2 (mean) with a 3x3 box, Filter 2 (mean) with a 19x19 box. For the PolInSAR estimation evaluation, we selected the mean filter with a 19x19 box (bottom right map). The color bar is similar on all map and ranges from [20-45m]. ....	122
Figure 8-15: Comparing the LiDAR canopy height on the left to the PolInSAR vegetation height on the right. ....	123
Figure 8-16: 2-D Histogram with the PolInSAR retrieved height as X axis and the LiDAR canopy height as Y axis. The color indicates the number of pixel in the bin where red is the most populated bin. The bias is less than 1m and the RMSE is around 4m. ....	123
Figure 8-17: Zoom from Figure. 8-16 over a flat area. The RMSE is 3.0m. ....	124
Figure 8-18: Zoom from Figure 8-16 over a relief area. The RMSE is 4.3m. ....	124
Figure 8-19: PolInSAR mean height versus LiDAR mean height for the sixteen zones. ....	128



## TABLES

Table 1-1: BIOMASS science objectives, measurement and instrument requirements [Le Toan et al 2010].....	13
Table 1-2: TROPISAR team .....	15
Table 2-1: Characterisation of the different geodesic system used over French Guiana.....	18
Table 2-2: Parameterisation of the CIRCE® freeware in order to perform transformation between the two reference systems. ....	18
Table 2-3: Geographic system over French Guiana.....	19
Table 3-1: Main characteristics of the SETHI system. ....	24
Table 3-2: Radar system parameters. ....	27
Table 3-3: Radar data acquisitions per flight. ....	30
Table 3-4: Geocoding process.....	36
Table 3-5: Beginning of a transformation grid file ( grille). ....	36
Table 3-6: Survey of the calibration targets. ....	37
Table 3-7: Incidence angle for the trihedrals. ....	40
Table 3-8: Summary of estimated calibration accuracy in the TropiSAR data set. ....	41
Table 3-9: $\sigma^0$ as a function of incidence angle for P and L Band. ....	44
Table 3-10: Localisation accuracy analysis using SLC and the file .grille. ....	45
Table 3-11: Accuracy of geolocation over Paracou from SLC and file .grille. ....	46
Table 3-12: Geometric accuracy analysis. ....	47
Table 3-13: SAR data quality parameters. ....	47
Table 4-1: Summary of the plots considered in the TropiSAR project.....	52
Table 4-2: Mean soil moisture measurements on two dates .....	55
Table 5-1: Example of file that contains estimation of the above ground biomass (Mg) stored in each plot. Geographical coordinates of the center of each subplot follow the UTM WSG 84 22N. The different spatial resolution of biomass estimation can be assessed within each sheet of the file. ....	63
Table 5-2: Processed Radar data per site. ....	64
Table 5-3: Recommendation of SAR format as a function of applications. ....	66
Table 5-4: Geocoded images at P band.....	66
Table 5-5: Geocoded images at L-Band.....	66
Table 6-1: Estimation of the above ground biomass (Mg.ha <sup>-1</sup> ) stored in each plot, with error estimates. ....	81
Table 6-2: AGB estimation based on DBH, and based on both DBH and total tree height. Ntree is the number of trees measured in each plot. % Error is the error between the two measurements (in %). ....	81
Table 7-1: Stand identifier, number of stand pixels, stand biomass and elevation angles corresponding to the "tropi0007_Pcons_Xx_slc" acquisition files.....	90
Table 7-2: Radar Backscatter coefficients derived from the "tropi0007_Pcons_Xx_slc" acquisition files. ....	91
Table 8-1: Statistics on the temporal decorrelation histograms presented in Figure 8-3.....	110



## 1. INTRODUCTION

One of the most unequivocal indications of man's effect on climate is the continual and accelerating growth of carbon dioxide (CO<sub>2</sub>) in the atmosphere. The principal contribution to this growth is emissions from fossil fuel burning. However, the rate of growth is substantially less and much more variable than the emissions because of a net flux of CO<sub>2</sub> from the atmosphere to the Earth's surface. This net flux can be partitioned into atmosphere-ocean and atmosphere-land components, whose mean values for the 1990s are  $2.2 \pm 0.4 \text{ GtC y}^{-1}$  and  $1.0 \pm 0.6 \text{ GtC y}^{-1}$  respectively (International Panel on Climate Change (IPCC), 2007). More than 98% of the land use change flux should be due to tropical deforestation (IPCC, 2007), which converts carbon stored as woody biomass (of which around 50% is carbon) into emissions. The most basic methods of calculating this flux simply multiply the area deforested (derived from national statistics or remote sensing) by the average biomass of the deforested area, expressed in carbon units (IPCC, 2003). More complete methods of carbon accounting include carbon fluxes from the soil, differential decay rates of carbon depending on how the biomass is used, and regrowth fluxes. Both methods are severely compromised by lack of reliable information on levels of biomass actually being lost in deforestation; this uncertainty alone accounts for a spread of values of about 1 GtC y<sup>-1</sup> in different estimates of carbon emissions due to tropical deforestation. Assessing the future conditions of the Earth system requires better quantification of the significance of both direct deforestation and changes in carbon stocks, compared with background 'reference' conditions.

*Tropical forests play a key role in the global carbon cycle, and hence global climate. Despite their importance, they remain poorly characterized compared to other ecosystems on the planet.*

The BIOMASS mission [Le Toan et al., 2010] is retained in January 2009 as one of the three candidates for the next Earth Explorer Core mission to go to phase A. BIOMASS will meet a pressing need for information on the carbon sinks and sources in the forests globally, which will be of essential value for climate modelling and policy adaptation, e.g. REDD. Table 1 summarises the primary science objectives, the measurements and instrument requirements of BIOMASS as defined during the mission pre-feasibility study phase (Phase 0) which finished in January 2009.



Primary science objectives	Measurement requirements	Instrument requirements
Quantify magnitude and distribution of forest biomass globally to improve resource assessment, carbon accounting and carbon models	Above-ground forest biomass from 70° N to 56° S with accuracy of $\pm 20\%$ at spatial scale of 100-200 m.  Forest height with accuracy of $\pm 4$ m.  Forest mapping at spatial scales of 100-200 m.	P-band SAR (432-438 MHz)  Polarimetry for biomass retrieval and ionospheric correction  Pol-InSAR capability to measure forest height  Constant incidence angle (25°-35°)  25-45 day repeat cycle for interferometry  Dawn-dusk orbit to reduce ionospheric effects  1 dB absolute accuracy in intensity measurements  0.5 dB relative accuracy in intensity measurements  5 year mission lifetime
Monitor and quantify changes in terrestrial forest biomass globally, leading to improved estimates of:  (a) terrestrial carbon sources (primarily from deforestation) using accounting methods;  (b) terrestrial carbon sinks due to forest regrowth and afforestation	Biomass loss due to deforestation and forest degradation, annually or better, at spatial scales of 100-200 m.  Biomass accumulation from forest growth, at spatial scale of 100-200 m; 1 estimate per yr in tropical forests, 1 estimate over 5 yrs in other forests.  Changes in forest height caused by deforestation.  Changes in forest area at spatial scales of 100-200 m, annually or better.	

Table 1-1: BIOMASS science objectives, measurement and instrument requirements [Le Toan et al 2010]

### 1.1. Campaign Objectives

During phase 0, biomass retrieval algorithms have been developed and validated for the range of biomass up to 300 t/ha. The methods are based on combining SAR intensity and SAR Polarimetric interferometry (PolInSAR) which provide respectively estimates of biomass and canopy height. One of the important findings from the BIOSAR 2007 airborne campaign in boreal forest was that at P-band, the temporal coherence remains high after 20-30 days. The result indicates that forest height can be retrieved with good accuracy using interferometry and a single P-band satellite at time intervals compatible with spaceborne missions. Reversely, at L band, the loss of coherence after 20-30 days implies the use of two satellites for the height retrieval.

The questions which remain to be addressed in Phase A concern the overall performance of the retrieval algorithms in tropical forests characterized by high biomass density ( $> 300$  t/ha) and complex structure.



Among the actions to be undertaken during phase A recommended by the ESA's Earth Science Advisory Committee who reviewed the mission concepts and recommended BIOMASS for further study, the following action is of utmost importance: to conduct flight campaigns particularly in high forest density regions to verify the robustness of the height and biomass retrieval algorithm.

It is essential that BIOMASS could measure the biomass density in tropical forests, in order to estimate this large component of the terrestrial carbon pool and the carbon sources generated by deforestation in the tropics with accuracy.

The TropiSAR experiment in French Guiana has been proposed to provide feedbacks to ESA and CNES on the performances of a P-band SAR to measure biomass and canopy height of a tropical forest with high biomass stocks.

Specifically, TropiSAR is designed for the following objectives:

- to provide measurements of temporal coherence at P- and L-band over tropical forests for time intervals compatible with spaceborne missions (typically 20-30 days)
- to assess the performance of methods to convert P-Band SAR intensity and interferometric measurements into forest biomass and forest height.
- to assess uncertainties in in-situ methods for biomass estimates and tree allometry for tropical forests under consideration.

The above objectives were addressed through a set of coordinated ground and airborne SAR and LiDAR acquisitions over tropical forest and preliminary analysis of the datasets.

The TropiSAR campaign is composed of two main tasks. The first concerns the in-situ measurements and the LiDAR data analysis while the second includes the SAR data acquisitions and calibration site characterisation and SAR data analysis. The second task, the SAR data acquisition, took place in August 2009, with flight occurring between the 10<sup>th</sup> of August and the 1<sup>st</sup> of September. This report documents both aspects of the project, the acquired database and analysis.

After a rapid description of the TROPISAR team, the document starts with an overall description of the study sites. It then provides valuable information about the geographic systems in use in French Guiana and the available DEMs. The next section details the SAR data acquisition campaign, the SETHI radar system and the processing workflow, including the calibration procedure and the data quality analysis. An in-depth description of the forest sites and in-situ measurements follows.

The next section is intended as a database description. The document then goes over the analysis performed during this project, in-situ error analysis, PolSAR analysis and PolInSAR analysis. After the final discussion, several annexes are included. The first one lists the geographic coordinates of the different study plots. The second one contains the SAR format description. The last one is an exhaustive list of the delivered SAR products.

## 1.2. Campaign institutions

ONERA: ONERA was responsible for the SAR data acquisition with the SETHI system, SAR data processing and calibration and PolInSAR data analysis





**CESBIO:** CESBIO was responsible for the Polarimetric analysis of the SAR data and the evaluation of the combined methods for vegetation characterisation.

**EDB and CIRAD:** The Evolution and Diversité Biologique laboratory and CIRAD were responsible for the in-situ measurements and the LiDAR data sets over the two main forest sites as well as the error analysis on the in-situ measurements. These 2 institutions are leading the GUYAFOR project which provided logistic support and financial support for the SAR data acquisition campaign and for the in-situ data measurements in 2009 and 2010.

### 1.3. Campaign participants

ONERA	Name	Role
	Pascale Dubois-Fernandez	Project manager – SAR data validation – PolInSAR analysis
	Olivier Ruault du Plessis	SETHI manager
	Daniel Heuze	SAR campaign management
	Remi Baqué	Radar operator – Hardware engineer
	Gregory Bonin	Radar operator – Hardware engineer
	Patrick Fromage	Radar operator – Hardware engineer
	Hubert Cantalloube	SAR processing
	Helene Oriot	SAR processing and Calibration
	Sandrine Daniel	SAR processing – Database organisation – Analysis
	Colette Coulombeix	SAR processing
	Aurelien Arnaubec	PolInSAR analysis
CESBIO	Thuy Le Toan	SAR data analysis
	Yannick Lasne	SAR data analysis
	Ludovic Villard	SAR data analysis
	Thierry Koleck	SAR data analysis
EDB	Jerome Chave	In-situ measurement – ground data analysis
	Maxime Réjou-Méchain	In-situ data collection – ground data analysis
CIRAD	Lilian Blanc	In-situ measurement – ground data analysis
	Gregoire Vincent	LiDAR processing
IRD	Michel Petit	Campaign logistics - Kaw site manager – Data analysis
	Papa Sonko	Computer support
	Jean-Francois Faure	Optical imagery and logistic support
	Michel Petit	SAR data analysis and local support
AvDEF	Eric Hays	Head pilot and Commandant de bord
	Daniel Bouet	Pilot
	Jean-Christophe aka l'écresse	Airplane operation - mechanics
	Fabrice aka Tonton	Airplane operation - mechanics

Table 1-2: TROPISAR team



## 2. OVERVIEW OF THE CAMPAIGN

### 2.1. The forest test sites

The data acquisition campaign has been organised around the permanent plots managed by EDB and CIRAD, Nouragues site and Paracou site taking advantage of a long history of in-situ measurements, data collection and scientific expertise. A calibration site was installed close to the Rochambeau airport. The “Marais de Kaw” was also included as it is of major ecological importance in French Guiana and represented an interesting example of flooded forests.

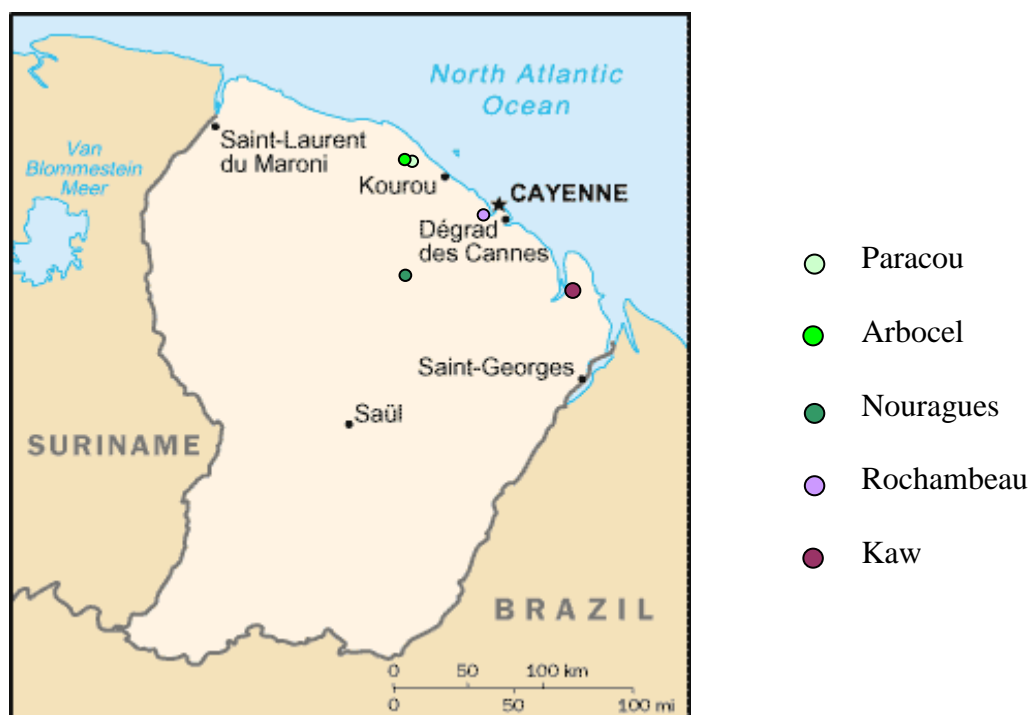


Figure 2-1: The overall location of the different sites imaged during the TropiSAR campaign

The Nouragues site is located 120 km South of Cayenne and was established in 1986. The landscape is a succession of small hills, between 60-120 m asl covered by a pristine forest. Human activity is unlikely to have induced major disturbances in the recent history. Recent floristic censuses have recorded over 200 species of trees above 10 in trunk diameter (DBH) in 2 plots of 1 ha each.

Several permanent plots are monitored among which a  $400 \times 300$ -m plot called Petit Plateau (PP) and a  $1000 \times 100$ -m plot, called Grand Plateau (GP). These plots are delineated by a grid of trails every 100 m, resulting in 10 1ha plots for PP and 12 for GP. A second site, called Nouragues-Pararé, is located 8 km South of the first one, on the North bank of the Arataye river, a tributary of the Approuague river with a  $300 \times 200$ -m permanent tree plot, called Pararé and established in the early 1980s. For the purpose of the TROPISAR project, two new plots were established: Balanfois a  $200 \times 100$ -m plot is midway between the two sites. The second, called Pararé-ridge is a  $100 \times 100$ -m plot some 1 km North of the Pararé station.





The Paracou experimental site is located in a lowland tropical rain forest near Sinnamary. More than 550 woody species attaining 2 cm diameter at breast height (*DBH*) have been described [Molino and Sabatier, 2001; Baraloto et al., unpublished data]; with an estimated 150 species per hectare [BRIDGE project, P. Petronelli, unpublished data]. Fifteen permanent 300 × 300 m plots were established in 1984. In these 9 ha square plots, a buffer zone of 25 m around the plot was created, and the present report used data on 250x250 m plots (i.e. 6.25 ha). From 1986 to 1988, nine of these 15 plots underwent three different logging treatments ranging from mild to severe. Additional permanent plots were established in 1990 (plot 13 to 15, 300 x 300 m each) and in 1991 (plot 16, 500 × 500-m) and have not experienced logging treatment. An area of 25 ha, called Arbocel and located near Paracou was initially clear-cut in 1976 to establish a pulp paper operation, but was abandoned in 1978. The natural regeneration of the forest has been subsequently studied by the CIRAD. Forest regrowth in the whole area has been monitored in a 250× 250 m permanent tree plot established since 1992 [de Foresta, 1981; Larpin, 1989; Toriola *et al.*, 1998]. For the purpose of the TropiSAR project, new plots were established to include planted forest in the plot pool.

## 2.2. The different geodesic system in French Guiana

In this report, we have decided to include this paragraph describing the different geodesic system in French Guiana. This is not intended as a tutorial but describes what we had to learn in order to work with the data coming from different sources..

There are two main reference systems in French Guiana. The oldest one corresponds to the Hayford 1909 ellipsoid, named CGS1967. This is the reference system used in the maps produced by the French National mapping agency, IGN. The corresponding altitude reference is the mean sea level.

The other one is based on the WGS84 reference system, associated to the IAG GRS80 ellipsoid, which is locally matched to the RGFG95.



The values associated with these two systems are provided in the following table extracted from the CIRCE manuel® :

IAG GRS 80	
(ellipsoïde associé aux systèmes mondiaux WGS84 et RGFG95) Ellipsoid associated to the global systems WGS84 and RGFG95	
IAG GRS 80 ellipsoid is defined by the following parameters (exact values) :	
Half major axis	a = 6 378 137,0 m
Flattening	f = 1/298,257 222 101
International HAYFORD 1909	
(Ellipsoid associated to the older systems Fort-Desaix, Sainte-Anne, Fort Marigot, CSG 1967)	
The international HAYFORD ellipsoid is defined by the following parameters (exact values) :	
Half major axis	a = 6 378 388,0 m
Flattening	f = 1/297

Table 2-1: Characterisation of the different geodesic system used over French Guiana.

The transformation between one system and the other one can be performed using the CIRCE® freeware available for download on the IGN official site or at: <http://geodesie.ign.fr/index.php?page=circe>

Table 2-2: Parameterisation of the CIRCE® freeware in order to perform transformation between the two reference systems.

One example is provided above where we can see how to parameterize CIRCE® to transform geographic coordinates from CGS67 to RGFG95 (WGS84). The example point has a 0 altitude in the first reference system and a -34.5m ellipsoidal height in the WGS84 reference system. Note also that a misuse of coordinates between the two systems can create a non-negligible spatial shift if proper care is not taken.



Geographic system	Ellipsoid	Height reference	Terminology	Sea level
WGS84	GRS80	RGFG95	Ellipsoidal height	-34.5m
CSG67	Hayford 1909	NGG1977	Altitude	0 m

Table 2-3: Geographic system over French Guiana.

**One must be aware that contrarily to what is expected, Google Earth® over French Guiana is not in the WGS84 coordinate system but in CGS1967. So beware of the apparent spatial shift.**

### 2.3. Digital elevation model of the areas

In order to perform the SAR processing, we have identified and evaluated several Digital Elevation Models available over the different sites.

The first one is extracted from the global SRTM DEM. The pixel spacing is every 3" of arc, around 90m. The coordinate system is the WGS84 geographic (Lat, Lon) associated with a reference ellipsoid GRS80. It is presented in the next figure.

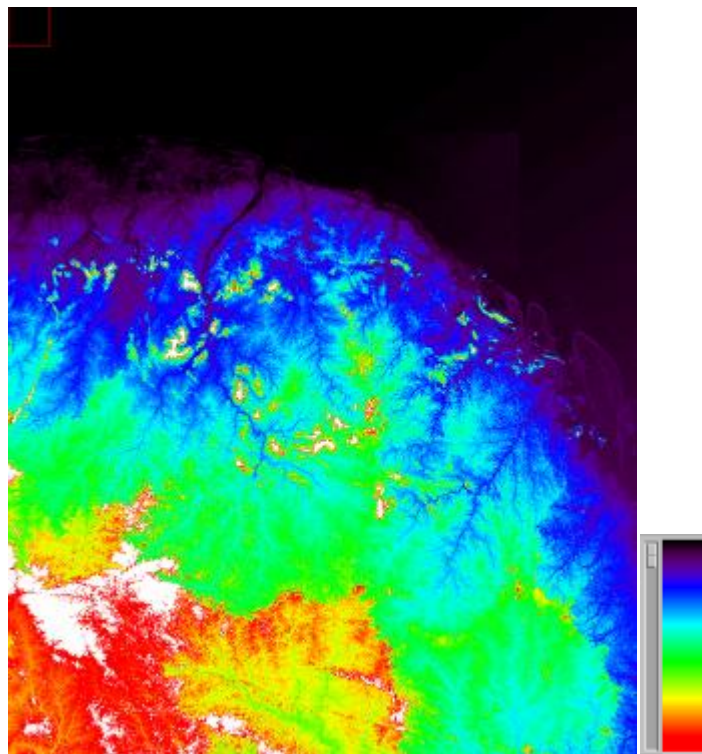


Figure 2-2: SRTM DEM over French Guiana. The coordinates of the upper left corner are: Lon = -56.000 & Lat=7.000. The coordinates of the lower right corner are: Lon = -52.000 & Lat= 1.000. The color scale ranges between [-100m , 300m].

This DEM has an averaged value over the sea of -95m. It was therefore translated to read -34m over the sea to match the RGFG95 which is the WGS84 reading over the sea,



according to the IGN site. One can note that the overall behaviour of this DEM seems good except a phase wrapping artefact in the lower left corner.

The other DEMs are local, associated with the two main forest sites Paracou and Nouragues. Both DEMs were acquired using a LiDAR, operated by ALTOA, an operator located in Cayenne, French Guiana.

These DEMs are available in UTM coordinates associated with the WGS84 reference system, but with respect to a local reference ellipsoid (NGG67) such that the sea level is at 0m.

The LiDAR DEMs and canopy model over Nouragues and Paracou remain the property of CIRAD as they were acquired under the project GUYAFOR and will not be delivered as part of this contract. Special request for these products can be filed directly with CIRAD, Point of contact Lilian Blanc, Principal Investigator for GUYAFOR (Lilian.Blanc@ecofog.gf).

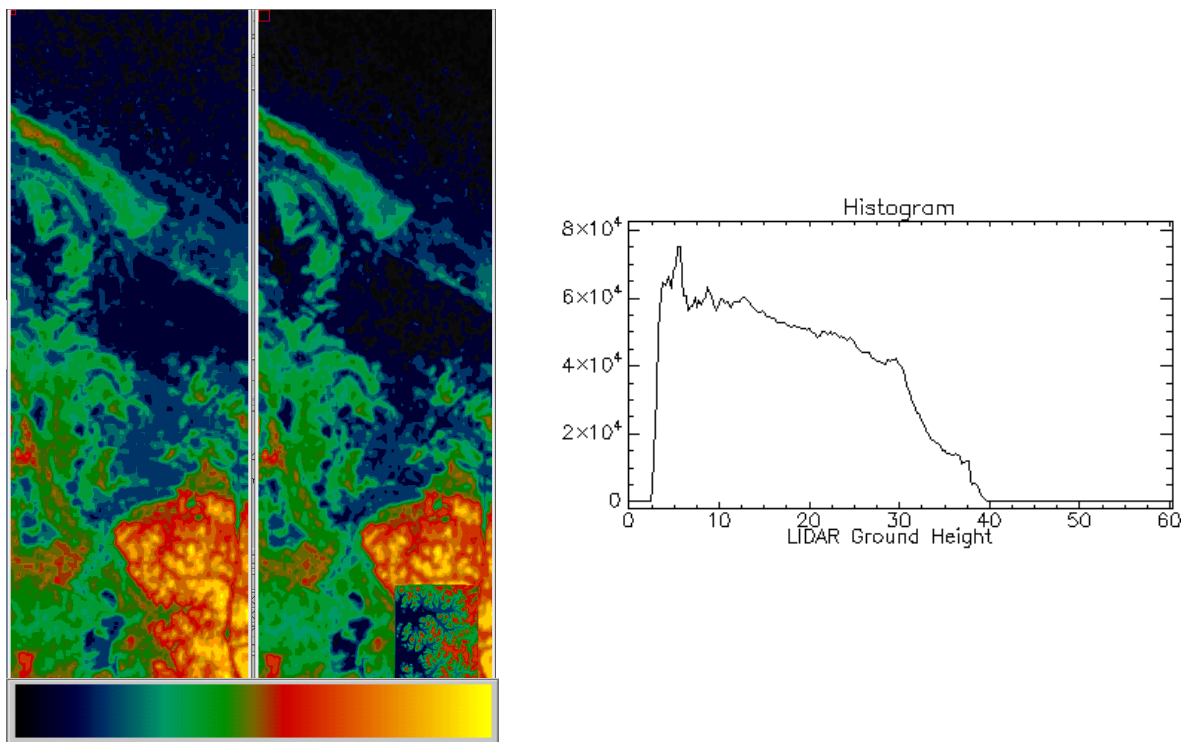


Figure 2-3: Paracou site: the upper left coordinates are E[m], N[m], 279844., 605120., lat, long -52.912083, 5.2437500; Lower right corner E[m], N[m], lon,lat : 288078 , 579931, -52.987083, 5.4712500. The reference for height is the NGG77 with a sea level reading at 0m. The color scale ranges [-5m, 65m]. The precise LiDAR DEM was inserted into the SRTM DEM on the right image. The overall structures are kept. However, there is a height difference between both DEM of around 30m. On the right, a histogram of the DEM over the studied site.

The precise LiDAR DEM over the Paracou site is only local. It is 2952mx 4370m. The SAR images cover a larger extend. Therefore, we decided to compute a compound DEM combining the SRTM DEM for a large coverage and the ALTOA DEM for precision over the forest plots. In order to do that, we shifted the SRTM DEM to put it in the same height reference system as the ALTOA DEM (95m) such that the sea level is around 0. The resulting DEM is presented in Figure 2-4. The precise DEM can clearly be identified in the lower part of this DEM because there is a definite shift in height estimated to be around 30m. This shift can





be explained by the forest height. The SRTM height refers to the top of the vegetation layer as it was computed from interferometric measurement at C band, whether the ALTOA DEM characterises the ground layer. The overall topography is mild with a height excursion over the studied area of around 30m.

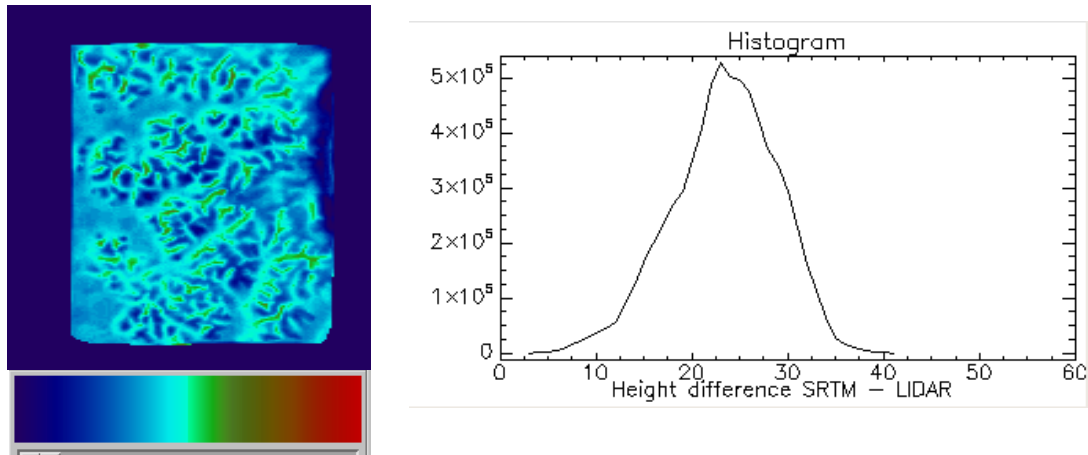


Figure 2-4: Height difference between SRTM and the LiDAR derived DEM over the Paracou site. The color scale ranges [0m,40m], The difference is certainly linked to the vegetation height.

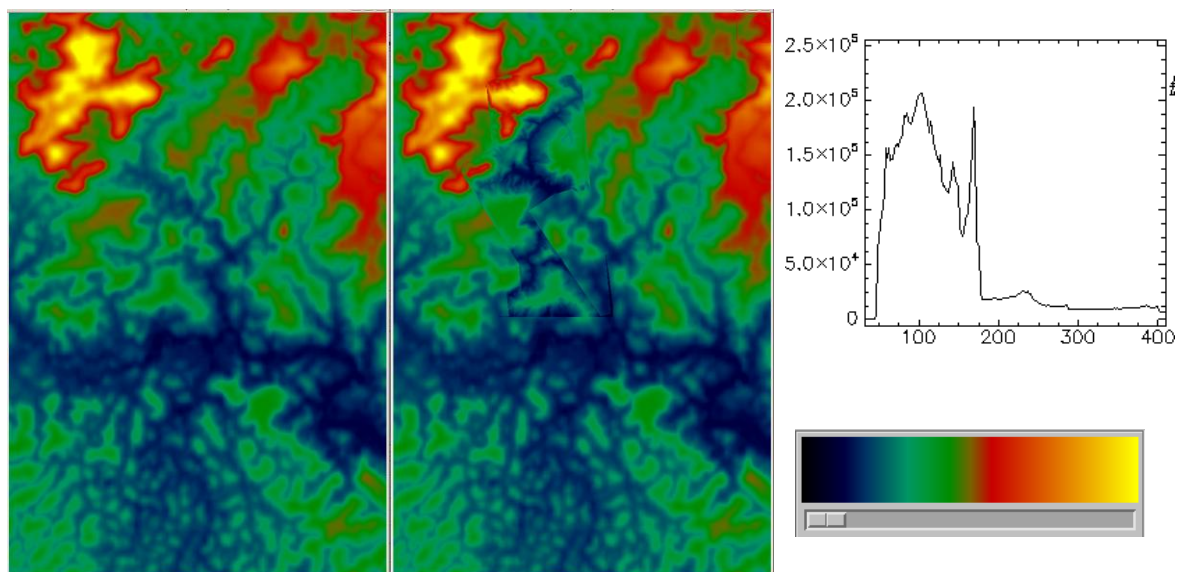


Figure 2-5: Nouragues site: the upper left coordinates are E[m], N[m]: 310000, 455000; Lower right corner E[m], N[m], 32000, 440000. The reference for height is the NGG77 with a sea level reading at 0m. The color scale ranges [0m, 400m]. The precise LiDAR DEM was inserted into the SRTM DEM on the right image. The overall structures are kept. However, there is a height difference between both DEM of around 30m. On the right, a histogram of the DEM over the studied site.

The same procedure was applied to the DEM over the Nouragues site and we could make the same conclusion which is that the SRTM DEM is around 35 to 40m above the LiDAR DEM. The difference is less visible on Figure 2-6, just because the color scale covers a much larger range.

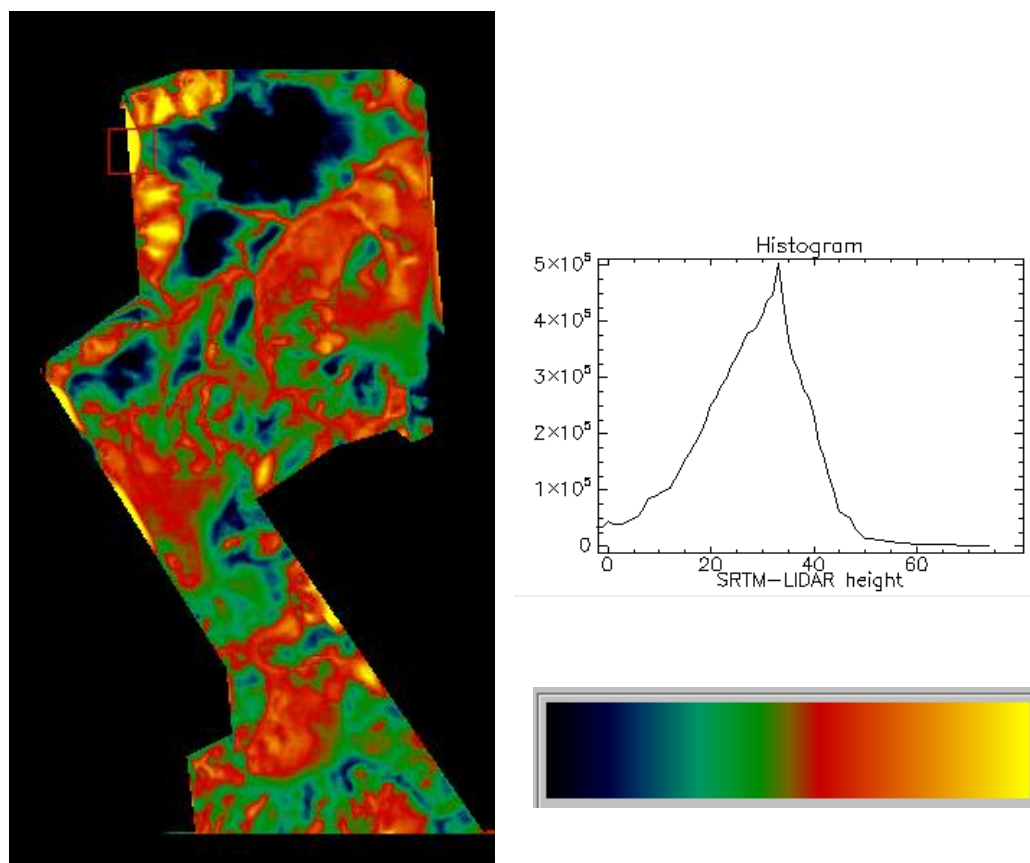


Figure 2-6: Height difference between SRTM and the LiDAR derived DEM over the Nouragues site. The color scale ranges [0m, 60m], The difference is certainly linked to the vegetation height.

This comparison had two purposes. The first one was to present the underlying topography of the two sites, Nouragues and Paracou and the available DEMs. The second purpose was to justify the decision made during the projection of the SAR data. We do not have a global DEM with an adequate accuracy. The SRTM DEMs is signing inside the vegetation, resulting in an apparent error in the range of 30m. The topography in both cases is characterised by rolling hills with amplitude of around 30m in the case of Paracou, a little more in the case of Nouragues. Therefore, we decided to use a flat earth model for the processing and projection of the radar images. The effect of using a flat terrain for processing has no impact on the quality of the resulting SLC data as the topography is mild and the trajectories straight. The flat earth model has an impact on the accuracy of the geocoded data. We selected the flat earth height to be well suited to the site, minimising the localisation errors. The resulting accuracy is of the same order as if we had based our projection on a top of the canopy DEM (SRTM). Our approach has the advantage of not introducing another source of errors.

We also provide a file which allows the user to compute accurately the image position of a point from its geographic coordinates and its ellipsoidal height.



### 3. TROPISAR AIRBORNE SAR ACQUISITION

#### 3.1. SAR data acquisition schedule

The TropiSAR SAR acquisition campaign was designed around two specific sites in French Guiana. These two sites are Paracou and Nouragues. These sites were first defined in 1982 for Paracou and 1986 for Nouragues and have been extensively monitored and characterised since then under the responsibilities of CIRAD and CNRS.

The Airborne campaign took place in August 2009 with the SETHI airborne SAR system from ONERA. The plane, a Falcon 20 operated by AvDef, is usually based in Garons, the Nîmes Airport in Southern France. The plane transited to Cayenne via Northern Europe, the US and the Caribbeans as it does not have the necessary autonomy to cross the Atlantic in a direct route. The TropiSAR campaign was organised around one validation flight and 6 data acquisition flights. The following table provides the schedule of the different flights.

Flight Identifier	Flight Description	Flight date	Frequency bands
VOL0	Validation	10/08/2009	P + L
VOL1	Standard Zero-baseline	12/08/2009	P + L
VOL2	Tomo Nouragues	14/08/2009	P + L
VOL3	Standard	17/08/2009	P + L
VOL4	Tomo-Paracou	24/08/2009	P + L
VOL5	Standard + marais de Kaw	30/08/2009	P + L
VOL6	Standard Zero-baseline	01/09/2009	P + L

Table 3-1: SAR data acquisition calendar.

#### 3.2. The SETHI SAR system and acquisition radar parameters

ONERA, the French Aerospace Laboratory has been designing and operating airborne SAR systems for the past two decades. The airborne system proposed for this experiment is SETHI, a new generation SAR developed over the last four years, to be compatible with small/medium aircrafts for remote sensing applications.

SETHI combines two pods positioned under aircraft wings which are able to carry heavy and bulky payloads of different kinds ranging from VHF to Ku band and/or optical sensors with a wide range of acquisition geometries (Figure 3-1).





Figure 3-1: The Falcon 20 carrying the SETHI system. The two pods contain the radar antennas.

SETHI can be operated with 4 radar front-ends simultaneously together with two optical payloads. The architecture of the system may be viewed as “Plug-and-Play” and can integrate external instruments easily without going through extensive flight-readiness certification procedures.

Band	Centre Frequency [MHz]	Bandwidth [MHz]	Antenna	Polarimetry
UHF-VHF	225-475	250 MHz	Set of Dipole	Full
P	440	70 MHz	Array	Full
L	1300	200 MHz	Array	Full
X	9600	1200 MHz	Horn	Single Pol

Table 3-1: Main characteristics of the SETHI system.

The data recording system, inherited from RAMSES, allows up to four simultaneous channels with a maximum sampling frequency of 1.5 GHz, and a maximum data rate of 360MB/s for each recording channels.

The on-board installation is composed of five standard bays and two operator seats. Electronic boards were developed to control and command all the new racks. Each board uses a PIC18 microcontroller synchronized with the 10 MHz radar.

The pod design includes an outside envelope transparent to electromagnetism waves in a large range of frequencies and a main beam which guarantees the necessary mechanical resistance required by the aeronautical regulations. The useful length of the pod is 2.3 meters, its diameter is 0.535 meter and the payload weight can reach 120 Kg. An optical window in the nose of the pod can accommodate a camera.

A precise IMU is installed in the plane. It includes a differential GPS augmented by a OmniStar HP from IGI providing a typical real-time position accuracy of 20cm. There is a deported screen in the pilot cabin allowing the pilots to have direct access to this information.



This is a very important feature as for PolINSAR and tomography experiment the pilots are required to fly the same flight line repeatedly with a high accuracy.

The hard disk in the plane has a storing capacity of 1.7 TBytes. This is usually enough for a standard data acquisition flight.

When the plane is on the ground, the data can be downloaded to our processing machines through a direct 50m fiber optic cable providing a complete download in less than 2 hours. This feature is essential when we want to fly long flights several times during one day.

The P band antenna is in the left pod and to minimize double reflection from the belly of the plane, it is usually operated in a left looking configuration. The antenna beamwidth is  $100^\circ$  in elevation and  $60^\circ$  in azimuth with a 500W peak power.

The L-band antenna is found in the right pod. The L Band waveform is centered around 1.3 GHz and can be set to 150 MHz bandwidth. The antenna beamwidth is  $20^\circ$  in elevation and  $16^\circ$  in azimuth. The peak power is 300W.



Figure 3-2: The left pod containing the P-Band and the L-Band antennas.



Figure 3-3: The right pod containing the L band antenna and the two X band antennas.

In practice, the 4 recording channels have to be shared between all the radars. The L-Band in polarimetric mode requires 2 recording channels: On one channel, one records HH and HV, while the other channel acquires VH and VV. The UHF-VHF system is different; it requires only 1 channel as it records in sequence HH, HV, VH and VV for one PRF.

A polarimetric P-band SAR image example from TropiSAR2009 is given in Figure 3-4.



Figure 3-4 : Example of a dataset over the Marais de Kaw with a color composite image at P-band.

The typical swath width is around 5 km for simultaneous P and L acquisitions with a length of up to 10km. Note that the P Band swath width is larger as the antenna diagram is wider, as a consequence, the incidence angle excursion is larger (Figure 3-5). The corresponding system parameters for the two frequency bands are summarized in Table 3-2.

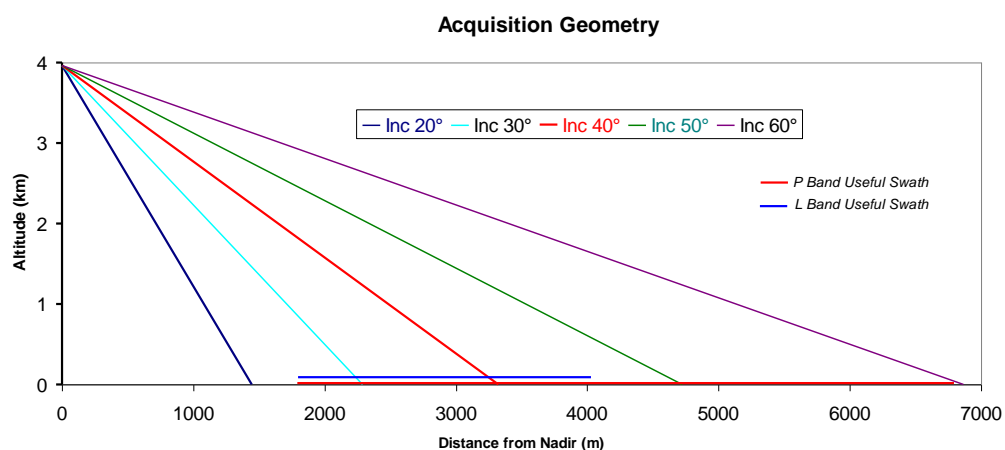


Figure 3-5: SETHI L- and P-band acquisition geometry.



Parameter	P-band	L-band
Geometry		
Altitude [ft,m]	13000/ 3962	
Velocity [m/s]	120	
Antenna		
Elevation aperture [°]	100	20
Azimuth aperture [°]	60	16
Waveform		
Mode	Full-Polar	Full-Polar
Peak Power [W]	500	200
Actual PRF [kHz]	2.5	5
Sampling rate [MHz]	500	500
Bandwidth [MHz]	260-460	1250-1400
Processed wave length [m]	0.652 – 0.896	0.214-0.24
Processed Bandwidth [MHz]	335-460	1250-1400
Relative bandwidth [%]	31	11
Range Resolution [m]	1.2	1.0
Azimuth resolution [m]	1.5	1.0
Range pixel spacing [m]	1.0	0.75
Azimuth pixel spacing [m]	1.0	0.75
Near Range [m]	4350	4350
Nb of pixels in range	4000	2600
Incidence angle range [°]	24-62	24-47

Table 3-2: Radar system parameters.



### 3.3. SAR data acquisition flight description

#### Flight 0: 10/08/2009

TEMPORAL BASELINE: -2 days

Site	Acquisition identifier	Planned line
Rochambeau	Tropi0001	ZB
Rochambeau	Tropi0002	ZB
Paracou	Tropi0007	ZB
Paracou	Tropi0008	ZB
Rochambeau	Tropi0010	ZB
Rochambeau	Tropi0011	ZB

#### Flight 1: 12/08/2009

TEMPORAL BASELINE: 0 day

Site	Acquisition identifier	Planned line
Nouragues 1	Tropi0101	ZB
Nouragues 1	Tropi0102	ZB
Nouragues 1	Tropi0103	ZB
Paracou	Tropi0104	ZB
Paracou	Tropi0105	ZB
Paracou	Tropi0106	ZB
Paracou	Tropi0107	ZB
Arbocel	Tropi0108	ZB
Arbocel	Tropi0109	ZB
Rochambeau	Tropi0110	ZB
Rochambeau	Tropi0111	ZB

#### Flight 2: 14/08/2009

TEMPORAL BASELINE: 2 days

Site	Acquisition identifier	Planned line
Nouragues 1	Tropi0201	ZB
Nouragues 1	Tropi0202	ZB
Nouragues 1	Tropi0204	B1
Nouragues 1	Tropi0205	B2
Nouragues 1	Tropi0206	B3
Nouragues 1	Tropi0207	B4
Paracou	Tropi0208	ZB
Paracou	Tropi0209	B1
Rochambeau	tropi0210b	ZB
Rochambeau	Tropi0211	ZB

**Flight 3: 17/08/2009****TEMPORAL BASELINE: 5 days**

Site	Acquisition identifier	Planned line
Nouragues 1	Tropi0301	ZB
Nouragues 1	Tropi0302	B1
Nouragues 2	Tropi0303	ZB
Nouragues 2	Tropi0304	B1
Paracou	Tropi0305	ZB
Paracou	Tropi0306	B1
Arbocel	Tropi0307	ZB
Arbocel	Tropi0308	B1
Rochambeau	Tropi0309	ZB
Rochambeau	Tropi0310	ZB

**Flight 4: 24/08/2009****TEMPORAL BASELINE: 12 days**

Site	Acquisition identifier	Planned line
Paracou	Tropi0401	ZB
Paracou	Tropi0402	ZB
Paracou	Tropi0403	B1
Paracou	Tropi0404	B2
Paracou	Tropi0405	B3
Paracou	Tropi0406	B4
Paracou	Tropi0407	B5
Arbocel	Tropi0408	ZB
Arbocel	Tropi0409	B1
Rochambeau	Tropi0410	ZB
Rochambeau	Tropi0411	ZB

**Flight 5: 30/08/2009****TEMPORAL BASELINE: 18 days**

Site	Acquisition identifier	Planned line
Nouragues 1	Tropi0501	ZB
Nouragues 1	Tropi0502	B1
Nouragues 1	tropi0502b	B2
Paracou	Tropi0505	ZB
Paracou	Tropi0506	ZB
Paracou	Tropi0507	B1
Kaw	Tropi0509	ZB
Rochambeau	Tropi0510	ZB
Rochambeau	Tropi0511	ZB



**Flight 6: 01/09/2009****TEMPORAL BASELINE: 20 days**

Site	Acquisition identifier	Planned line
Paracou	Tropi0601	ZB
Paracou	Tropi0602	ZB
Paracou	tropi0603	ZB
Paracou	Tropi0604	ZB
Nouragues 2	Tropi0605	ZB
Nouragues 2	Tropi0606	B2
Nouragues 1Bis	Tropi0607	ZB
Nouragues 1Bis	Tropi0608	B1
Nouragues 1	Tropi0609	ZB
Nouragues 1	Tropi0610	BZ
Rochambeau	Tropi0611	ZB

*Table 3-3: Radar data acquisitions per flight.*

Different planned baselines are available. ZB means Zero-baseline: the reference trajectory is flown. B1, B2, B3, B4, B5 indicates that the trajectory flown is lower than the reference line with a vertical shift of 50ft, 100ft, 150ft, 200ft and 250 ft respectively.

We chose to fly the tomographic lines in a vertical plane rather than in a horizontal plane because the resulting interferometric perpendicular baseline experiences a smaller variation across the swath with this geometry. [Dubois-Fernandez, 2010, Dubois-Fernandez, 2011]

Over Nouragues, because of some severe topography, we had selected to fly several lines: Nouragues 1, Nouragues 2 and Nouragues 1Bis. The radar image coverage is outlined on Google in the figures listed below.

*Figure 3-6: Paracou image coverage: Note that tropi0506 extends significantly to the North.*





February 2011 V2.1



Figure 3-7: Nouragues SAR data coverage. Three different lines were acquired over Nouragues. They are identified on this figure.

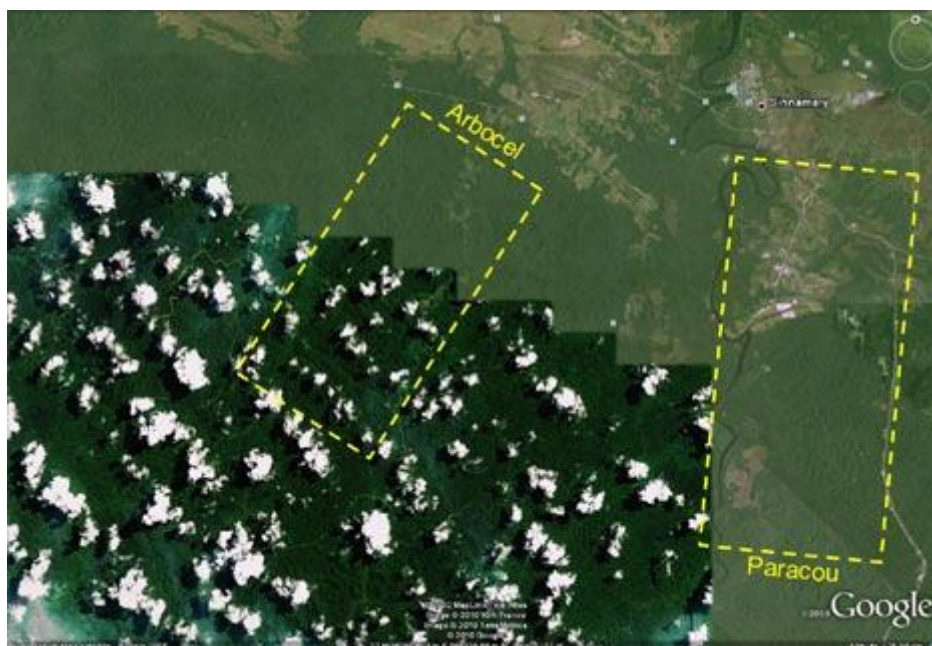


Figure 3-8: The Arbocel site is close to the Paracou one.



Figure 3-9: The coverage of the SAR data acquisition over the Kaw area.

Only a selected set of the full acquisition set was processed and delivered. The list is provided in the TropiSAR dataset section and Annex C.

### 3.4. Processing workflow

#### 3.4.1. SLC processing

The processing is performed as a series of steps which are outlined in the following paragraphs:

##### Archiving the data

The recorded data is first transferred from the airborne system to the archive machine. This can be done via a fiber optic link when the archive machine can be installed close to the plane (within 50m) or by extracting the hard disks from the plane. At this point, for each data take, the recorded data is composed of several files, in the high rate recorder proprietary format. The system also creates a TIGI file indicating the time reference associated with each data take.

##### Trajectory hybridation

The IMU + GPS trajectory information associated with each flight needs to be processed with a special software provided by IGI, the manufacturer of the IMU system.

##### Demultiplexing the data

Before the data is processed, it is necessary to demultiplex the data. This operation takes as an input the set of recorded files and creates one file of raw data per channel. For example, in the case of TropiSAR waveform, this process will create 8 raw data files, PHH, PHV, PVH, PVV, LHH, LHV, LVH and LVV files and their respective header files.

##### Extracting the data take trajectory and adapting it to the SAR antenna





The datatake trajectory is extracted from the flight trajectory based on the TIGI file and the lever arms (relative positions between the GPS antenna and the SAR antennas) are taken into account.

#### SLC processing

The SLC data is then processed with the PAMELA software, the ONERA SAR processor. It was decided to use a flat earth geometry for focusing purpose for the following reasons:

- There is no precise DEM covering the full zone
- The SRTM DEM is signing the top of the vegetation and not the ground, introducing a variable shift reflecting the vegetation height of the order of 30m or more.
- The topographic excursion is of the order of 30m, comparable to the error associated with the vegetation height.

This option doesn't have any impact on the focussing quality.

#### SLC post-processing and calibration

The SLC data is then post-processed. The post-process consists in the radiometric and polarimetric calibration. The calibration parameters are computed based on the data acquisitions over the calibration site. In this case, the calibration site was located on the Rochambeau airport and included up to 6 reference targets, distributed in the range direction. On each flight, we flew at least two calibration flights. The calibration factors are set uniquely for the whole campaign, one set of parameters for each frequency and the multiple acquisitions over Rochambeau can be used to assess the stability of the system over the campaign period. For P-Band an extra step is necessary to remove cross-talk, assumed to be linked to a reflection on the wing of the plane. The approach, based on the Quegan's method [Quegan , 1994] is performed in the frequency domain [Oriot et al, 2010]. The procedure is detailed in the next paragraph.

The crosstalk removal procedure was inspired by the Quegan's polarimetric calibration procedure described in [Quegan, 1994]. S. Quegan models the cross-talk by a Transmission and Reception matrices.

$$\begin{bmatrix} Sm_{Hh} & Sm_{Vh} \\ Sm_{Hv} & Sm_{Vv} \end{bmatrix} = \begin{bmatrix} R_{Hh} & R_{Vh} \\ R_{Hv} & R_{Vv} \end{bmatrix} \begin{bmatrix} S_{Hh} & S_{Vh} \\ S_{Hv} & S_{Vv} \end{bmatrix} \begin{bmatrix} T_{Hh} & T_{Vh} \\ T_{Hv} & T_{Vv} \end{bmatrix} \Rightarrow \begin{bmatrix} Sm_{Hh} & Sm_{Vh} \\ Sm_{Hv} & Sm_{Vv} \end{bmatrix} = \begin{bmatrix} 1 & \frac{w}{k} \\ u & \frac{1}{k} \end{bmatrix} \begin{bmatrix} S_{Hh} & S_{Vh} \\ S_{Hv} & S_{Vv} \end{bmatrix} \begin{bmatrix} \alpha k & \alpha k z \\ v & 1 \end{bmatrix}$$

$$\text{with } \alpha = \frac{R_{Hh}}{R_{Vv}} \frac{T_{Vv}}{T_{Hh}}, k = \frac{R_{Vv}}{R_{Hh}}$$

where  $S_{mij}$  stands for the measured signal for the polarization channel  $ij$ ,  $S_{ij}$  the polarized signal on the ground,  $R_{ij}$ , reception matrix  $T_{ij}$  Transmission matrix.

The R and T matrix coefficients are rewritten as a set of parameters (u,v,w,z,α,k). The complete set of parameters can be found in [Quegan, 1994].

Under the hypothesis that the co-polar and cross-polar channels are uncorrelated over natural clutter (under the assumption of reflection symmetry), and that the  $Hv$  channel and  $Vh$  channel are equal (if one neglects the noise level). The covariance matrix  $\langle S^* \cdot S \rangle$  can be written as:



$$\langle S^* . S \rangle = \begin{bmatrix} S_{Hh}^* \\ S_{Hv}^* \\ S_{Vv}^* \\ S_{Vh}^* \end{bmatrix} \begin{bmatrix} S_{Hh} & S_{Hv} & S_{Vh} & S_{Vv} \end{bmatrix} = \begin{bmatrix} \sigma_{Hh-Hh} & 0 & 0 & \sigma_{Hh-Vv} \\ 0 & \sigma_{Hv-Hv} & \sigma_{Hv-Vh} & 0 \\ 0 & \sigma_{Hv-Vh} & \sigma_{Vh-Vh} & 0 \\ \sigma_{Hh-Vv}^* & 0 & 0 & \sigma_{Vv-Vv} \end{bmatrix}$$

S Quegan shows that the parameters (u,v,w,z,α) only depends on  $\langle S_m^* . S_m \rangle$ . Therefore, they can be computed from the polarimetric covariance matrix estimated from the data.

In this experiment, we modified the Quegan's methodology by

- (1) removing the geometrical cross-talk due to attitude variation of the plane over the flight
- (2) estimating the Quegan's parameters both in range and frequency

Figure 3-10 presents an example of the α parameter estimated over frequencies (vertical axis) and range (horizontal axis) on our data. This figure shows the dependency of the parameter with both range and frequency.

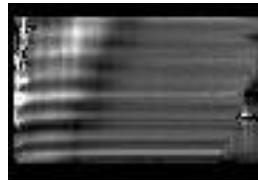


Figure 3-10: Quegan's parameter α as a function of range in the X axis, and frequency Y axis on the TropiSAR data.

During the one-month campaign, seven flights were acquired for the TropiSAR experiment, all at a 4000 m altitude. 4 other SAR data acquisition flights were also performed and for these other flights the platform altitude was lower, resulting in a different incidence angle range. Figure 3-11 is a plot of the v parameter according to the incidence angle before removing the aircraft attitude (left figure) and after removing the aircraft attitude. The different curves correspond to different acquisitions and attitude conditions. The v parameters differ if the aircraft attitude is not removed whereas they display the same behaviour when the attitude is compensated.

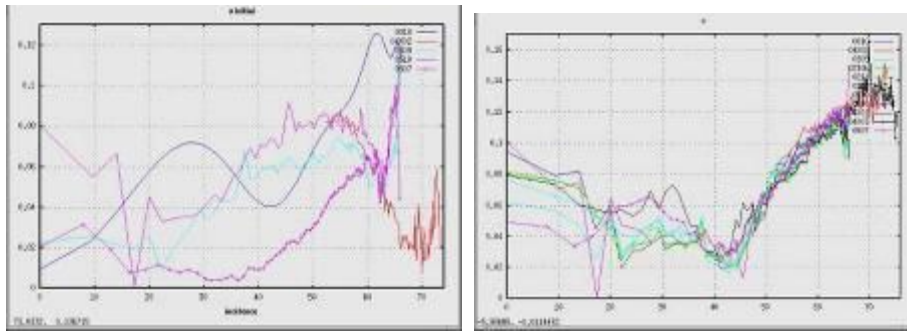


Figure 3-11: Quegan's parameter  $v$  estimated over range before aircraft-attitude compensation (left image) and after aircraft-attitude compensation (right images). The different curves correspond to different data with different aircraft attitudes.

The secondary bounce of the wave on the wing results in an antenna pattern deformation. This deformation depends on (1) the frequency, (2) the incidence angle of wave and (3) the polarization state. In order to remove this effect, we used the corner reflectors that have been placed across the swath on the calibration area. 5 corner reflectors were installed and several acquisitions were gathered using different flight configurations so that we have the frequency response of the corner reflectors for 11 incidences. By measuring the frequency response of each corner reflector on the images and interpolating these frequency responses in between, the residual radar transfer function was estimated and removed from the different channels.

### 3.4.2. Interferometric processing

The interferometric processing consists in projecting the SLC information from one image into the SLC geometry of another image. This is done based on the trajectory information and fine tuned in order to maximise the coherence. This is also performed assuming a flat earth geometry and the flat earth component is removed.

### 3.4.3. Geocoding

#### Transforming pixel position to latitude and longitude

Being able to link precisely one pixel on the image to one geographic location is essential. So is the reverse. In order to provide this correspondence independently of the altitude of the point (which we do not know precisely as we do not have any precise DEM), we provide with each SAR SLC dataset a file providing a transformation grid, called “\*.grille”. The grid file allows to link a position in the image (x,y) associated with a height to a precise latitude and longitude. It can also be used to associate an image position and a height to a geographic position.



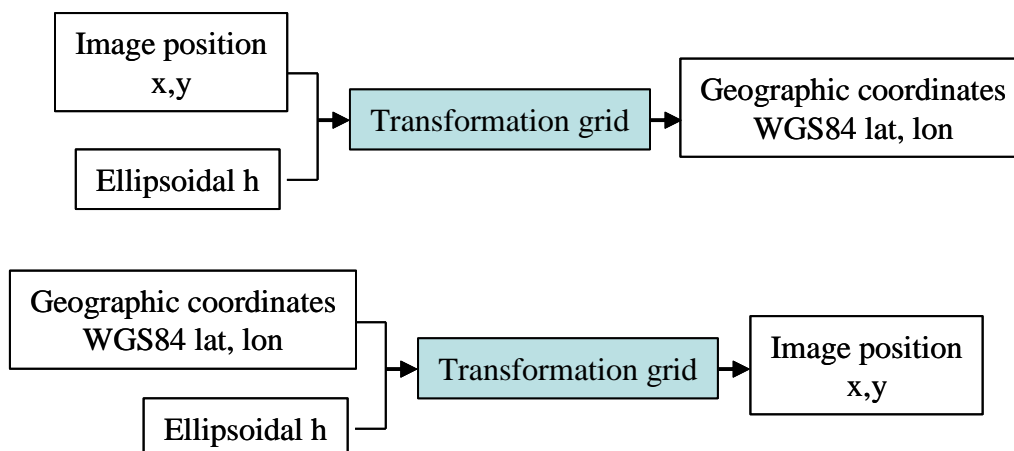


Table 3-4: Geocoding process.

This transformation grid file is a text file. The file starts with a short description indicating the relevant reference system, the desired accuracy. For this project, we have chosen 1.5m as accuracy. This value was used to compute the maximum step size in the three dimensions, range, azimuth and height such that the error resulting from a simple linear interpolation between the grid points will create an error below the requested accuracy. The first lines describe also the range of altitude as well as the number of steps in the line dimension (29 in the range direction), in the azimuth direction (129) in the altitude direction (58). The file contains then 29x129x58 lines listing x,y,h,lon,lat where x,y are the image pixel position in range and azimuth, h is the ellipsoidal height with respect to the GRS80 ellipsoid, and lon, lat are the longitude and latitude (E, N) in WGS84 system.

```

% Grille de geoereferencement de l'image tropi0402_Pcons_Hh_slc.1 calculée pour une précision de 1.500000 m entre alt = -103.758803 m et
alt = 301.638805 m
% format : ligne colonne altitude longitude latitude (longitude = latitude=0 si pas de donnée)
% Les coordonnées géographiques sont exprimées en WGS84, les altitudes sont données par rapport à l'ellipsoïde de GRS 80
nb_lig 29
nb_col 129
nb_alt 58
10 0 -103.7588 -52.9161292218770 5.2460086137288
10 0 -103.5015 -52.9161376843845 5.2460097385163
...
  
```

Table 3-5: Beginning of a transformation grid file ( grille).

In order to use the grid, one way is to identify the two height levels framing the desired height. On each height layer, the desired localisation information is computed via a linear interpolation and a final interpolation is performed in the height direction to compute the localisation information.

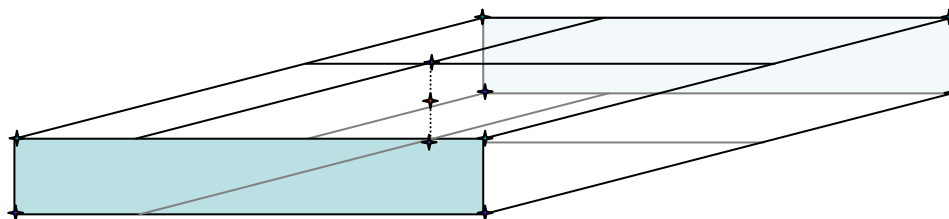


Figure 3-12: Computing the geographic position of the  $i,j,h$  pixel. First identifying the upper and lower layers, then on both layers, from the four corner points, compute the geographic position of the point located at the center of the face, then interpolate between these two points.

### Ground projected file

The SLC data is also ground projected assuming a flat earth geometry as the accuracy of the available DEM is of the same order as the topographic excursion. The ground projection reference system is in WGS84 UTM22 coordinates. The header provides information about the pixel spacing and the position of the corners of the file.

### 3.4.4. Calibration

#### 3.4.4.1. Radiometric calibration at P Band

The radiometric calibration was performed by measuring the radar crosssection of the different reference targets present on the scene.

Six reference targets were deployed on the calibration site and were used to establish and validate the radiometric and polarimetric calibration of the SETHI dataset. There were 5 trihedral corner reflectors with a wired mesh of 25mm intervals, and one dihedral reflector oriented at  $22.5^\circ$ .

The trihedrals installed on the calibration site were surveyed and a precise localisation was performed using DGPS technique. The localisation accuracy on the three surveyed trihedral is better than 50cm.

Target	N	W	Accuracy
T1	N 4°48'40.74893"	W 52°22'45.34181"	<0.5m
T2	N 04°48.748'	W 052°22.373'	7m
T3	N 4°48'54.02294"	W 52°22'00.26902"	<0.5m
T4	N 04°48.997'	W 052°21.814'	7m
T5	N 4°49'12.35357"	W 52°21'19.74087"	<0.5m
Dihedral	N 04°48.926'	W 052°21.984'	7m

Table 3-6: Survey of the calibration targets.



The trihedral were installed with respect to a geographic orientation  $263^\circ$ , corresponding to a true orientation of  $245^\circ$  (the magnetic declination in Guiana is  $17.5^\circ$ ) The flight tracks were following a route  $155^\circ$ , or a magnetic route of  $173^\circ$ .



Figure 3-13: The 5 reference targets T1, T2, T3, T4, T5 and Dr.

The trihedrals have 2.3m long vertices. The targets were shipped from France to French Guiana via sea-cargo and installed along the airport in a low vegetation area.



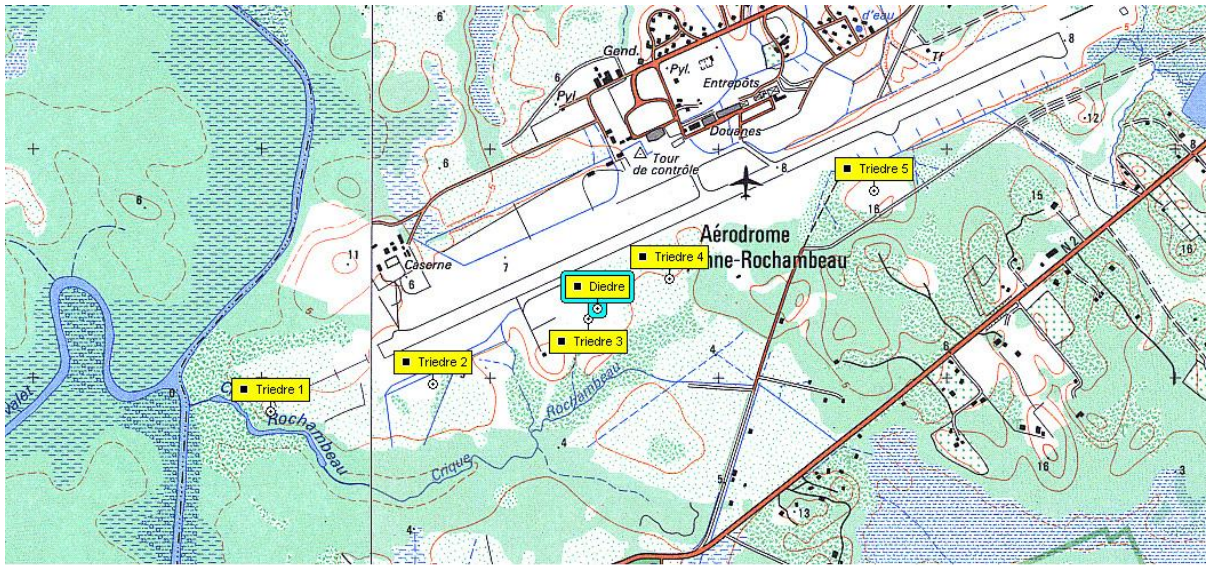


Figure 3-14: The setup for the reference targets. T1 is in the near range while T5 is in the far range.

T1 is the trihedron corresponding to the near-range and because of mechanical constraint, it was not possible to orient the base plane in order to match the radar acquisition geometry.

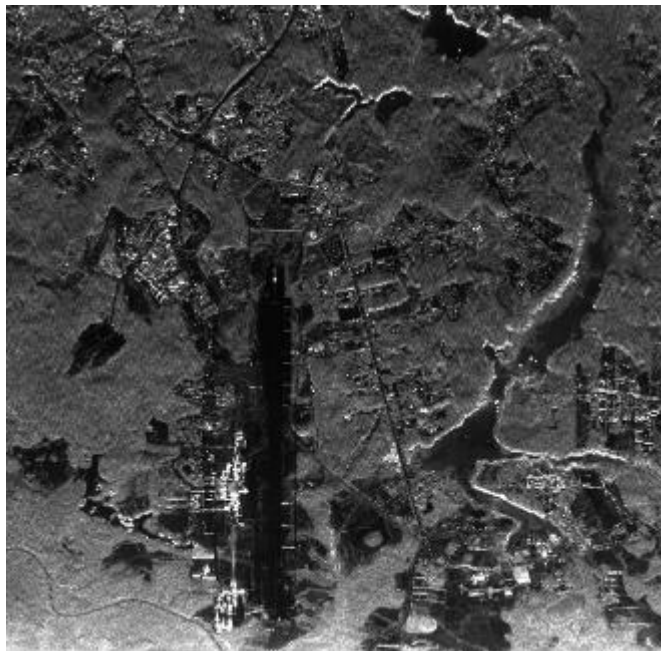


Figure 3-15: Radar image of the calibration site Rochambeau airport.

T2 and T5 were present during all the flights and were used as reference. The calibration keys were computed over one acquisition (Tropi0010: flight 0, acquisition 10) and applied to all remaining flights. The mathematical formula taking into account the attenuation in emission and reception is the following:

$$\text{Key} = \text{key\_ref} + 45\text{dB} - \text{Att\_em} + 10\log(P_{\text{em}}/500)$$



The calibration key was found to be satisfactory for Flight 1, 2, 4 and 6 and was lowered by 0.5dB on Flights 3 and 5 based on the trihedral responses. There is a good stability of the response and the absolute level varies inside a 1dB range.

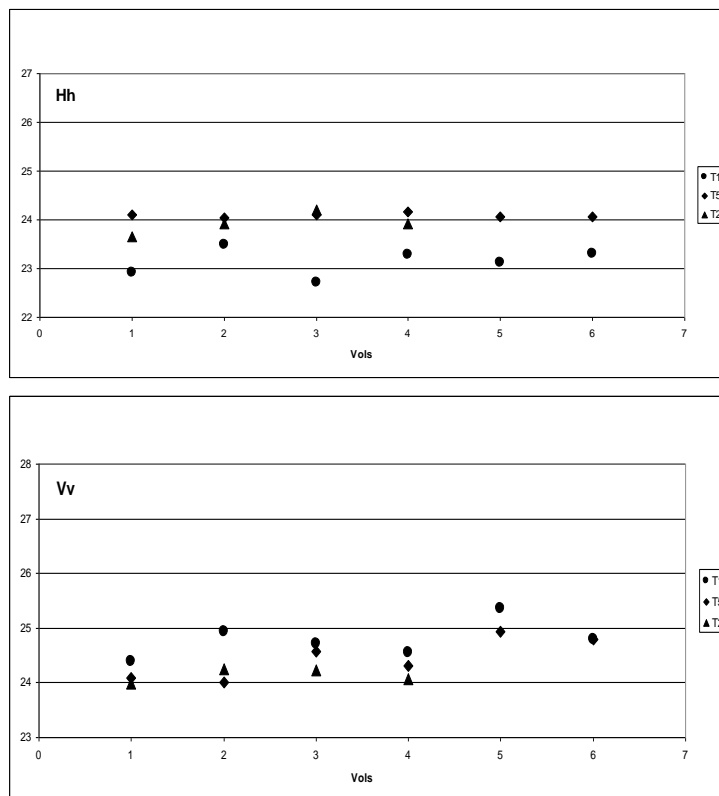


Figure 3-16 : Radar cross section responses over the trihedral in HH polarisation and VV polarisation at P Band.

Name of target	T1	T2	T5
Incidence Angle	24°	32°	49°

Table 3-7: Incidence angle for the trihedrals.

#### 3.4.4.2. Radiometric calibration at L Band



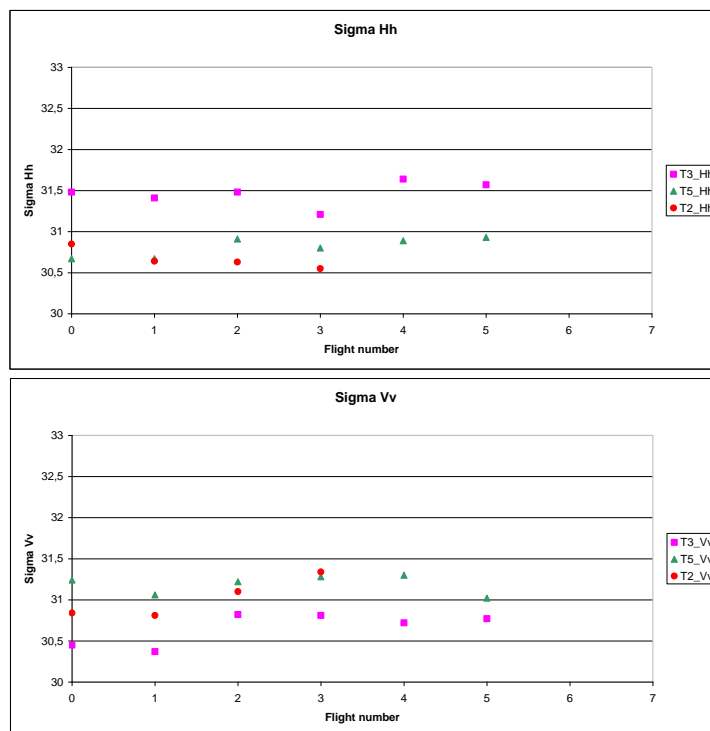


Figure 3-17: Radar cross section responses over the trihedral in HH polarisation and VV polarisation at L-Band.

$$Key = key_{ref} + 1dB - Att_{em} + 10\log(P_{em}/200)$$

with  $key_{ref}=270.13dB$ .

These calibration parameters are applied to the 7 flights.

#### 3.4.4.3. Polarimetric calibration

The phase between HH and VV was computed over the trihedrals and it was found to be close to 0 after post-processing. The mean and standard deviation of the phase of the trihedral was computed at P and L band :

P-Band: Mean  $1^\circ$  with a standard deviation of  $2.2^\circ$

L-Band: Mean  $-1^\circ$  with a standard deviation of  $4^\circ$

#### 3.4.4.4. Summary of calibration accuracy

The following table summarises the calibration accuracy based on the trihedral reflector analysis.

Incidence [30° - 50°]	P-Band	L-Band
Radiometric accuracy	+/- 0.5dB	+/- 0.5dB
Co-polar phase accuracy	$1^\circ \pm 2.2^\circ$	$-1^\circ \pm 4^\circ$

Table 3-8: Summary of estimated calibration accuracy in the TropiSAR data set.



The numbers in Table 3-8 were computed on the trihedral responses in the different acquisitions. As can be seen in Figure 3-15, the relative variation for one specific trihedral is around 0.5 dB (+/-0.25) dB and over all trihedrals this maximum variation is +/-0.5dB around the true value.

### 3.4.5. SAR data quality evaluation

SAR data quality can be assessed through several parameters, each characterising one aspect of the data. We have the Noise-Equivalent sigma0 (NEsigma0), the cross-talk levels, the residual channel unbalance.

#### 3.4.5.1. Noise-equivalent sigma0

This parameter characterises the overall noise level in the data. It includes the thermal noise, the quantisation noise, some remaining interferences. It can be interpreted as the backscatter floor in the data. How do we measure it?

Several techniques have been proposed in the literature. One is based in the analysis of the shadow areas, assuming that the only measured signal in these zones are due to noise. However, the technique is tricky to implement as shadow areas are linked to observation geometry and cannot be found in all images. We have selected one which allows to compute the variation of the NEsigma0 in the swath. It is based on the reciprocity principle. In the data set, we expect the HV signal to be exactly equal to the VH signal. The noise in these two channels is assumed to be uncorrelated. Therefore, the observed decorrelation between the two signals is due to the noise.

$$\begin{aligned}
 M_{hv} &= S_{hv} + N_{hv} \\
 M_{vh} &= S_{vh} + N_{vh} \\
 S_{hv} &= S_{vh} \\
 \langle N_{hv} N_{vh}^* \rangle &= 0 \\
 \langle N_{hv} N_{hv}^* \rangle &= \langle N_{vh} N_{vh}^* \rangle = N^2 \\
 SNR &= \frac{\langle S_{vh} S_{vh}^* \rangle}{N^2} \quad NE\sigma_0 = \frac{\langle S_{vh} S_{vh}^* \rangle}{SNR} \\
 \frac{\langle M_{hv} M_{vh}^* \rangle}{\sqrt{\langle M_{hv} M_{hv}^* \rangle \langle M_{vh} M_{vh}^* \rangle}} &= \frac{\langle S_{hv} S_{vh}^* \rangle}{(\langle S_{hv} S_{vh}^* \rangle + N^2)} = \frac{1}{1 + SNR^{-1}}
 \end{aligned}$$

This can be readily estimated across the swath for all the images.

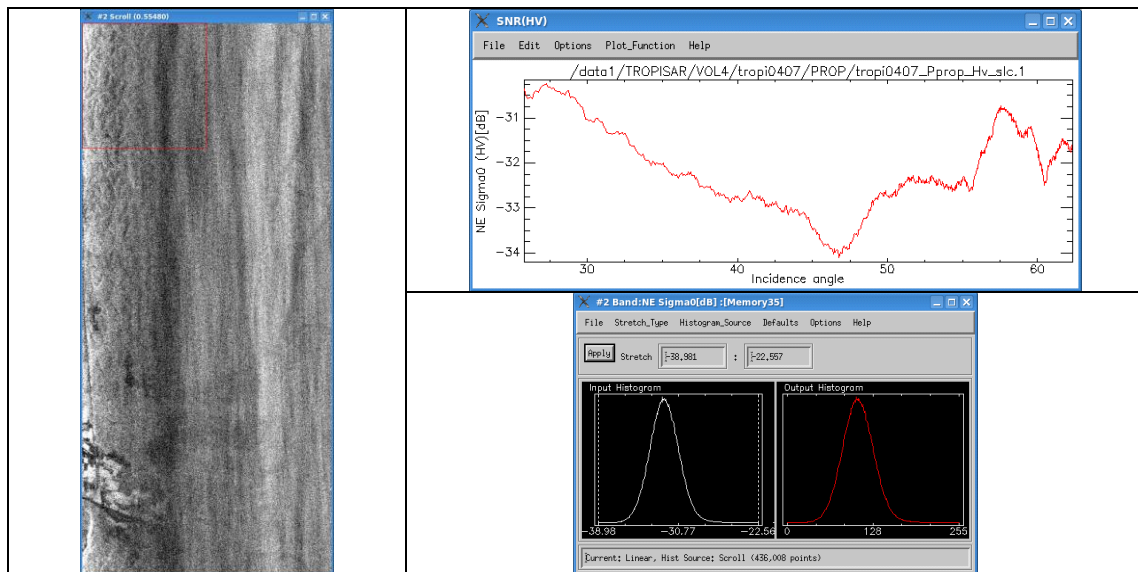


Figure 3-18: P-Band ,NEsigma0 analysis , Image , Range profile, NE sigma0 histogram.

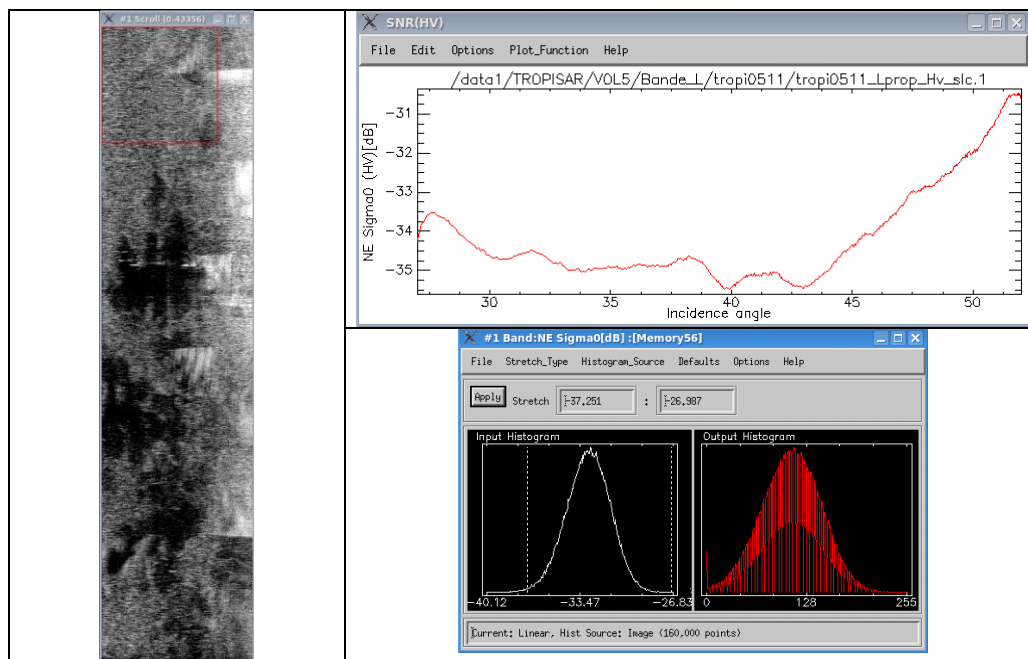


Figure 3-19: L-Band, NEsigma0 analysis , Image , Range profile, NE sigma0 histogram.

On the NEsigma0 L band image, one can clearly see interferences happening in the far range. These interferences have not been filtered on purpose in order to maintain the exact same processing parameters between all the images.

This analysis is performed systematically to all images. The results are found to be consistent from one acquisition to the next.



NE-Sigma0 [dB]	P-Band	L-Band
25-35°	-30	-33
35-45°	-32	-35

Table 3-9: NEsigma0 as a function of incidence angle for P and L Band.

### 3.4.5.2. Crosstalk level

The cross talk was computed using the Quegan's procedure [Quegan, 1994] The same notation are used. As a reminder, here is the model used.

$$C_{ct} = A \begin{pmatrix} \alpha & \alpha w & v & vw \\ \alpha u & \alpha & uv & v \\ \alpha z & \alpha wz & 1 & w \\ \alpha uz & \alpha z & u & 1 \end{pmatrix} \begin{pmatrix} k^2 & 0 & 0 & 0 \\ 0 & k & 0 & 0 \\ 0 & 0 & k & 0 \\ 0 & 0 & 0 & 1 \end{pmatrix} C$$

where  $C_{ct}$  is the measured covariance matrix and  $C$  is the true covariance matrix. The  $k$  factor represents the channel unbalanced between HH and VV and the  $\alpha$  parameter is the unbalance between the two cross-polarised channels. These two factors are corrected within the calibration step. The  $u, v, w, z$  are the cross talk parameters.

These parameters can be estimated over a flat area for which the reflection symmetry hypothesis is verified.

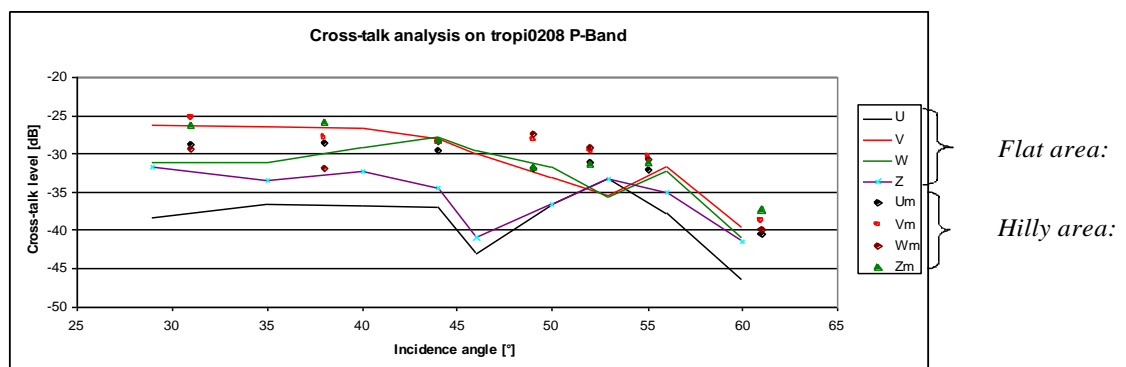


Figure 3-20: Polarisation isolation levels at P band.

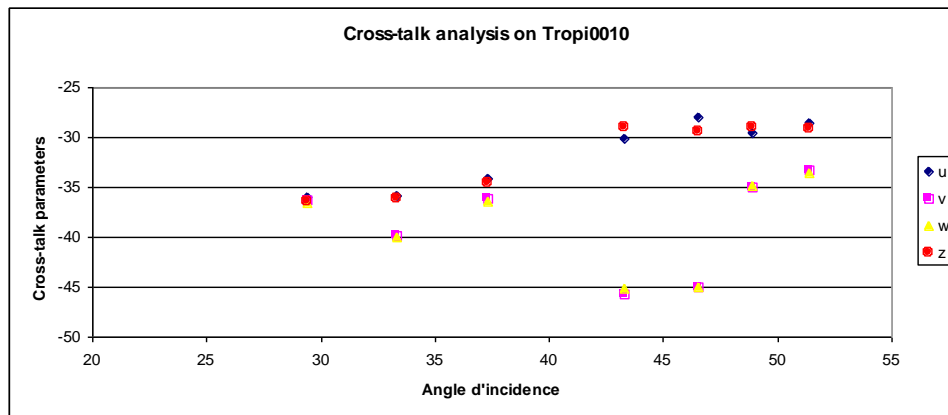


Figure 3-21: Polarisation isolation levels at L band.

### 3.4.6. Geocoding quality assessment

The geocoding quality assessment was performed over Paracou by comparing the localisation of specific targets. The first one is a corner reflector. Using the GPS coordinates (standard GPS reading, with an estimated accuracy around 10m) of a trihedral reflector deployed along the Combi Paracou road, and a trihedral altitude measured on the 1/25000 IGN map to be 9 m (estimated between 8.5 m and 10 m), we obtained the ellipsoidal height with CIRCE and using the “grille de passage”, we computed the image position of the trihedral reflector. The true image position can also be established and the two are compared in the table provided below.

Geographic coordinate		Altitude	Ellipsoidal height	Estimated radar coordinate		Measured radar coordinate		Error in pixels	
Lat	Long			Azimuth	Range	Azimuth	Range	Azimuth	Range
5,31793	-52,9398	9	-25,202	6042	2035	6039	2029	-3	-6
		8,5	-25,702	6042	2036			-3	-7
		10	-24,202	6042	2035			-3	-6

Table 3-10: Localisation accuracy analysis using SLC and the file .grille.

The error is around 3 pixels in Azimuth and 6.5 pixels in Range equivalent to 3.735 m in Azimuth and 6.5 m in Range. This is of the same order as the GPS accuracy.

This same study is done also over opportunity targets. The altitude and the UTM coordinates of these targets are determined with the IGN map.





Figure 3-22: IGN orthophoto of Paracou allowing a precise geo localization.

	UTM coordinate		Altitude	Ellipsoidal height	Estimated radar coordinate		Measured radar coordinate		Error in pixels	
	E	N			Azimuth	Range	Azimuth	Range	Azimuth	Range
1	284611	588105	9	-25,19	5961	2355	5958	2351	3	4
2	285016	588143	9	-25,20	6038	2046	6038	2044	0	2

Table 3-11: Accuracy of geolocation over Paracou from SLC and file .grille.

The quality of the georeferencing was also performed on the ground projected data. This geocoding quality assessment was performed over marais de Kaw with the projected WGS84 SAR images by comparing UTM coordinates.

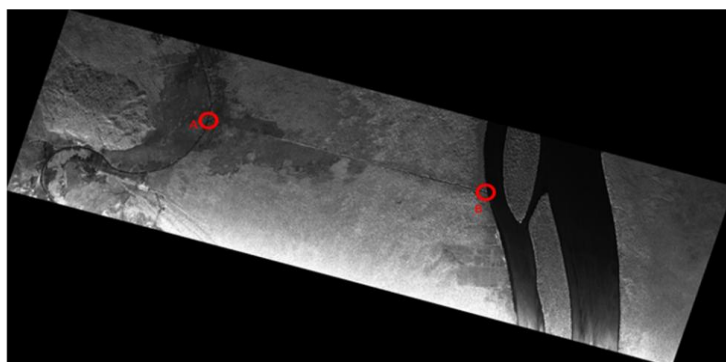


Figure 3-23: Tropi0509\_Pprop8Hh\_proj\_wgs84.dat.



Using the tropi0509\_Pprop\_\*\_proj\_wgs84.dat images, we identified two particular points A and B. From their radar coordinate and with some information available in the header, we determine their UTM coordinates which can then be compared to the UTM coordinate measured on the IGN map.

The geographic coordinate of the origin point (0,0) available in the header, is localized in Lat = 4,5349216376°, Long = -52,0697455955° and height ellipsoid = -39,7929m. To retrieve the UTM coordinate of our two particular points, we first evaluated the UTM coordinate of the origin point: E(x) = 381327.423m, N(y) = 501343.197m, then we retrieve the UTM coordinate by their radar image position.

Points	Measured radar coordinate		UTM coordinates estimated		UTM coordinates measured from IGN		Error in pixels	
	Azimuth	Range	E(x)	N(y)	E(x)	N(y)	E(x)	N(y)
A	5340	3373	386667	497970	386675	498000	8	30
B	12719	5583	394046	495760	394037	495792	-9	32

Table 3-12: Geometric accuracy analysis.

The UTM coordinates of these two points were measured on the 1/25000 IGN map with an accuracy of around 25m (1mm on the map)

### 3.4.7. Data quality assessment summary

		P-Band	L-Band
Calibration			
	Radiometric accuracy	+/- 0.5dB	+/- 0.5dB
	Co-polar phase accuracy	1° +/- 2.2°	-1° +/- 4°
NE-Sigma0 [dB]			
	25-35°	-30	-33
	35-45°	-32	-35
Cross-Talk Level		-25dB	-30dB
Geometric accuracy	(if altitude is known)	< 10m	< 10m

Table 3-13: SAR data quality parameters.

## 4. FOREST SITE DETAILED DESCRIPTION AND GROUND MEASUREMENTS

### 4.1. General description of Nouragues and Paracou

This study was carried out at two sites located in the lowland rain forest of French Guiana: the Nouragues and the Paracou Research Stations (Figure 4-1).



Figure 4-1: Location of the Nouragues and Paracou Research Stations in French Guiana.

#### 4.1.1. Nouragues Research Station

The Nouragues Station (4°05'N, 52°40'W, Figure 4 1) is located 120 km South of Cayenne and was established in 1986, near an inselberg (granitic outcrop) that reaches 430 m asl. The landscape is a succession of small hills, between 60-120 m asl. Rainfall is 2960 mm y<sup>-1</sup> (average 1987-2001), with a dry season that averages 73 days, from late August to early November, and a shorter dry season in March. Daily temperature ranges between 20 °C and 33 °C (annual mean 27 °C). Wind is never strong (maximum <14.2 m s<sup>-1</sup> between 1999 and 2002, mean = 0.11 ± 0.07 m s<sup>-1</sup>). No hurricanes or cyclones reach French Guiana. Human activity is unlikely to have induced major disturbances in the recent history: the Nouragues Indians are reported to have inhabited this area during the eighteenth century, but departed further South at least 200 years ago.

The forest around the station harbours a diverse flora [Sabatier and Prevost, 1990; van der Meer and Bongers, 1996], with over 1700 angiosperm species recorded in the Reserve ([Nouragues], <http://www.nouragues.cnrs.fr/plantspecies2.html>). Recent floristic censuses have recorded 177 and 204 species of trees above 10 in trunk diameter (DBH) in 2 plots of 1 ha each [BRIDGE] project unpublished). In total, the number of tree species may be well in excess of 400 species.

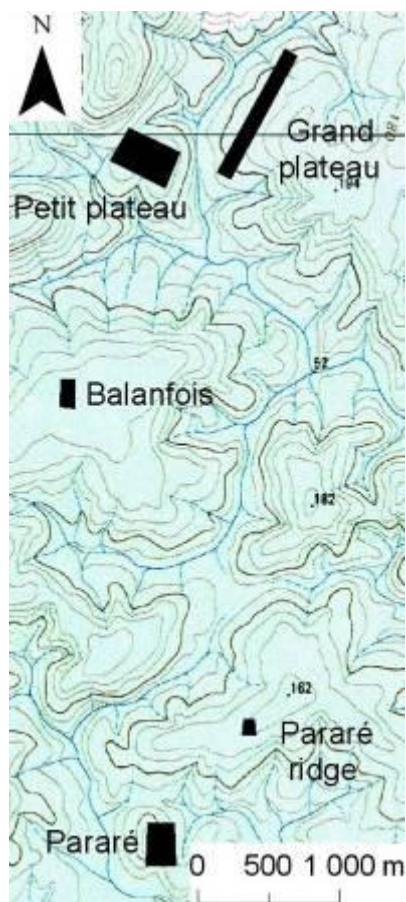


Figure 4-2: Localization of the 5 plots at the Nouragues research station.

The Nouragues Research Station has two camp sites. The Nouragues-Inselberg site is located on the west bank of a small river, called ‘crique Nouragues’, that flows on a fault separating two geomorphological entities [Grimaldi and Riera, 2001]. The west bank has a weathered granite parent material, with sandy soils of variable depth, on which a  $400 \times 300$ -m plot called Petit Plateau (PP) has been established [van der Meer and Bongers, 1996]. The east bank is on a metavolcanic rock parent material of the Paramaca formation, with clayey soils rich in ferruginous nodules, typical of the decomposition of a laterite crust. On the east bank, and ca. 500 m from PP, a  $1000 \times 100$ -m plot, called Grand Plateau (GP), has been established on a uniform and gentle slope toward the creek. Permanent sampling plots are delineated by a grid of trails every 100 m on two plateaux along a compass bearing of  $137^\circ$  either sides of crique Nouragues.

A second site, called Nouragues-Pararé, is located 8 km South of the first one, on the North bank of the Arataye river, a tributary of the Approuague river. This second station is on metavolcanic parent material, and is located close to a temporary site established by Museum National d’Histoire Naturelle in the late 1970s. It manages a  $300 \times 200$ -m permanent tree plot, called Pararé (Figure 4 2), established in the early 1980s.

For the purpose of the TropiSAR project, we established two new plots located on metavolcanic parent material. The first plot, called Balanfois (Figure 4 2), is a  $200 \times 100$ -m plot established in June 2010 midway between the two sites. The second, called Pararé-ridge is





a 100 × 100-m plot established in October 2010 on the first ridge of the plateau North of Pararé, some 1 km North of the Pararé station (Figure 4 2).

#### 4.1.2. Paracou Research Station

Paracou experimental site is located in a lowland tropical rain forest near Sinnamary, French Guiana (5° 18' N, 52° 55 'W; [Gourlet-Fleury *et al.*, 2004]). The site receives nearly two-thirds of the annual 3160mm ± 161SE of precipitation between mid-March and mid-June, and less than 50 mm per month in September and October [Gourlet-Fleury *et al.*, 2004]. The most common soils in Paracou are the shallow ferralitic soils limited in depth by a more or less transformed loamy saprolithe [Boulet and Brunet, 1983]. Some very thick ferralitic soils, with free vertical drainage, are primarily encountered on the highest residual summits of the area (approximately 40 m asl), but they can also be found at the bottom of the slopes [Epron *et al.*, 2006].

More than 550 woody species attaining 2 cm diameter at breast height (DBH) have been described [Molino and Sabatier, 2001; Baraloto *et al.*, unpublished data], with an estimated 150 species per hectare [BRIDGE project, P. Petronelli, unpublished data]. The dominant families at the site include Lecythidaceae, Leguminosae, Chrysobalanaceae, Euphorbiaceae.

Fifteen permanent 300 × 300 m plots were established in 1984 (Figure 4-3). In these 9 ha square plots, a buffer zone of 25 m around the plot was created, and the present report used data on 250x250 m plots (i.e. 6.25 ha). From 1986 to 1988, the plots underwent three logging treatments according to a randomized block design, with three replicate blocks of twelve plots, assigned as controls or one of three treatments. In Treatment 1, selected timbers were extracted, with an average of about 10 trees ≥ 50 or 60 cm DBH removed per hectare. Treatment 2 was logged as in Treatment 1, followed by timber stand improvement (TSI) by poison girdling of selected non-commercial species, with about 20 trees ≥ 40 cm DBH removed per hectare. Treatment 3 was logged as in Treatment 2 for an expanded list of commercial species, with about 45 trees ≥ 40 cm DBH removed per hectare. Depending on stand composition, some of the latter plots were less intensively logged than treatment 2 plots. Tree harvesting in the plots was initiated in October 1986 and was completed in May 1987. Timber stand improvement by poison girdling began in December 1987. Additional permanent plots were established in 1990 (plot 13 to 15, 300 x 300 m each) and in 1991 (plot 16, 500 × 500-m) and did not experience logging treatment.



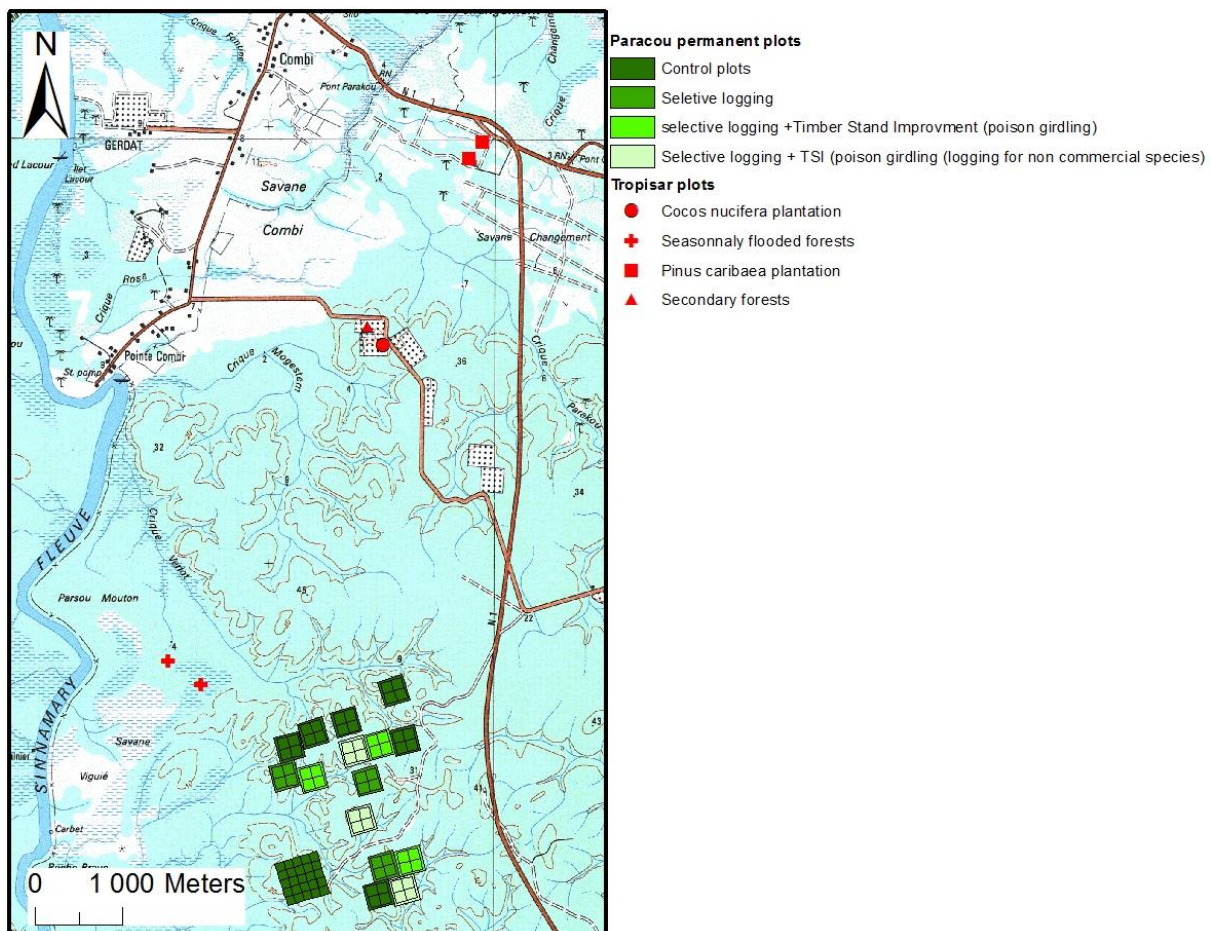


Figure 4-3: Location of the Paracou permanent plots and additional plots established for the TropiSAR project.

For the purpose of the project, we established 6 new plots near the Paracou research station:

- Two 70 × 70 m plots were established on a plantation of *Pinus caribaea*. L. Trees were planted in 1978.
- One 50 × 50-m plot was established on a plantation of *Cocos nucifera* planted in 1996.
- One 40 × 70-m plot was established in a secondary forest. This vegetation recovered from an abandoned oil palm plantation.
- Two plots of 0.5 ha were established following the modified Gentry protocol ([Baraloto] in review) in natural seasonally flood forests.

An area of 25 ha, called Arbocel and located near Paracou (Figure 4.1), was initially clear-cut in 1976 to establish a pulp paper operation, but was abandoned in 1978. The natural regeneration of the forest has been subsequently studied by the CIRAD. The area receives approximately 3119 mm of rainfall annually. Forest regrowth in the whole area has been



monitored in a 250× 250 m permanent tree plot established since 1992 [de Foresta, 1981; Larpin, 1989; Toriola *et al.*, 1998].

#### 4.2. Tree measurements and inventories

Ground plots cover more than 158 ha of forest in total (Table 4-1). In all plots, all living trees  $\geq 10$  cm DBH were mapped and censused to assess growth, recruitment and mortality every 1 to 5 years. Each individual tree was botanically identified whenever possible. DBH were calculated from circumference measures to the nearest 0.5 cm. For trunks without buttresses, DBH measurements were conventionally made at 1.3 m above the soil surface and points of measurement were marked using permanent paint on the trunk. For buttressed trees, trunks were measured 10 cm above the highest buttress and also marked with paint.

The same technique was applied for mature rain forest sites and for disturbed forest sites and plantations. In all cases, trees less than 10 cm DBH and lianas were ignored in the biomass estimate. Dead standing trees were also ignored.

A subsample of the surveyed trees was measured for their total tree height. We selected six 1-ha subplots, located on different forest plot, for which all trees were measured. We used a laser telemeter (LaserAce MDL Company) to spot the top leaf or branch from the ground. Turning around each tree, and using the opinion of at least three trained operators if needed, we were able to estimate the total height of all trees. Controls were regularly conducted to assess the performance of this technique. The tree height dataset currently contains 3029 trees.

Site	Forest type	Census date	Number of plots	Plot Size	Total census size	Number of trees
Paracou	Mature rain forest	2009	6	6.25	37.5	22,868
Paracou	Mature rain forest	2010	1	25	25	12,959
Paracou	Disturbed rain forest	2009	9	6.25	56.25	37,997
Paracou	Pinus plantation	2010	2	0.49	0.98	1178
Paracou	Coco plantation	2010	1	0.25	0.25	40
Paracou	Secondary forest	2010	1	0.28	0.28	367
Paracou	Flooded forest	2010	2	0.5	1	1275
Arbocel	Regrowth from clear-cut	2009	1	6.25	6.25	5468
Nouragues	Mature rain forest	2008	1	10	10	5098
Nouragues	Mature rain forest	2008	1	12	12	6338
Nouragues	Mature rain forest	2010	1	6	6	3093
Nouragues	Mature rain forest	2010	1	2	2	985
Nouragues	Mature rain forest	2010	1	1	1	484
			28		157.51	98150

Table 4-1: Summary of the plots considered in the TropiSAR project.



Details about the AGB for the different plots are presented in Section 6 together with the assessment of the field measurement errors.

### 4.3. Weather conditions

#### 4.3.1. Weather conditions in Nouragues

Weather conditions was measured using a WS-STD1 DeltaT meteorological station (<http://www.delta-t.co.uk>), with an automatic rainfall gauge, a temperature-humidity probe and an anemometer. Measurements were taken at a semi-hourly frequency. Daily rainfall varied between 0 and 19.2 mm/day, on August 18<sup>th</sup>, 2009. Total rainfall for the study period was 84 mm, and the monthly rainfall for august 2009 was average, over 100 mm/month. During the flight hours over Nouragues, no rainfall was recorded. Ground temperature and moisture were typical of tropical rainforest, with a daily temperature amplitude of 22-33°C, and a mean of 25.7°C over the study period. Air moisture varied between 50% (around mid-day) to 100%. During the flight periods over Nouragues, air moisture varied between 81% and 88%.

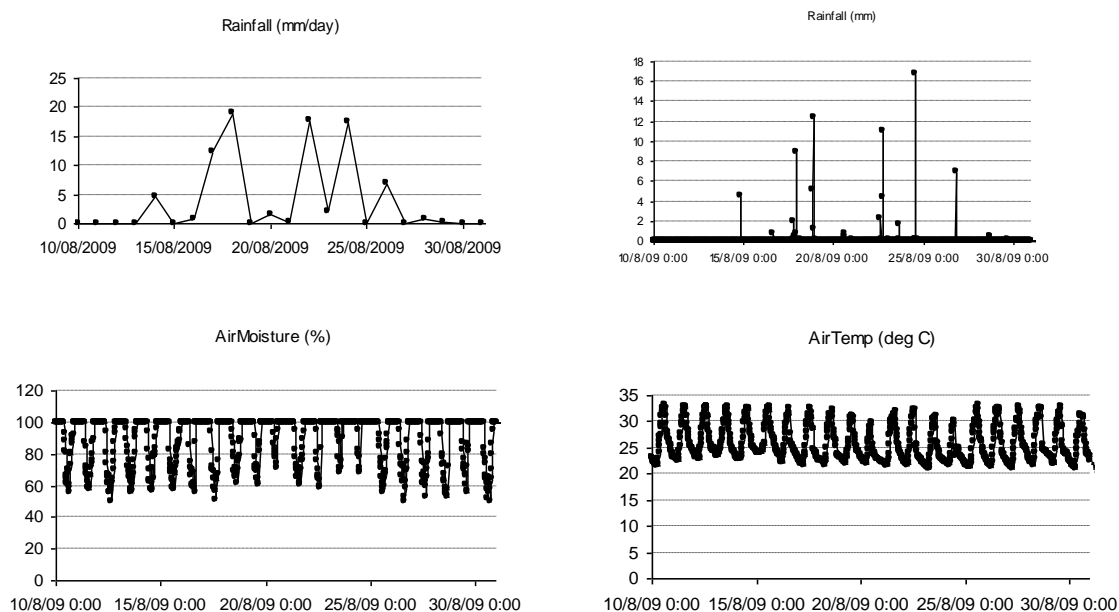


Figure 4-4: Rain fall, Air moisture and air temperature in Nouragues.

#### 4.3.2. Weather conditions in Paracou

Microclimate data were recorded at the Guyaflux tower (see [Bonal et al. 2000]). Air temperature and humidity (HMP45, Vaisala, Helsinki Finland) were measured at the ground level. Volumetric soil water content (SWC;  $\text{m}^{-3}\text{m}^{-3}$ ) using a frequency domain sensor (CS615; Campbell Scientific Inc.) at 0,05 cm depth were recorded. All meteorological data were collected at 1 min intervals and compiled as 30 min averages or sums with a CR23X datalogger (Campbell Scientific Inc.).

Total rainfall in august 2009 was 49 mm (8 days with rainfall). The mean annual rainfall recorded at the CIRAD meteorological station (Combi station located at 4 km form the



Guyaflux tower) is 114 mm. Rainfall exceeded 15 mm for two days: 6<sup>th</sup> (20 mm) and 17<sup>th</sup> august (15,8 mm). Similar values were recorded at the same date at the CIRAD meteorological station (resp. 18 and 14 mm).

Daily temperature amplitude recorded at the ground level ranged between 21,3 and 31,3°C and a mean of 25.5°C was recorded over the study period (August 2009).

Air moisture varied between 54% (around mid-day) and 98%. During the flight periods over Paracou (8 am to 12 am), air moisture varied between 96% and 56%.

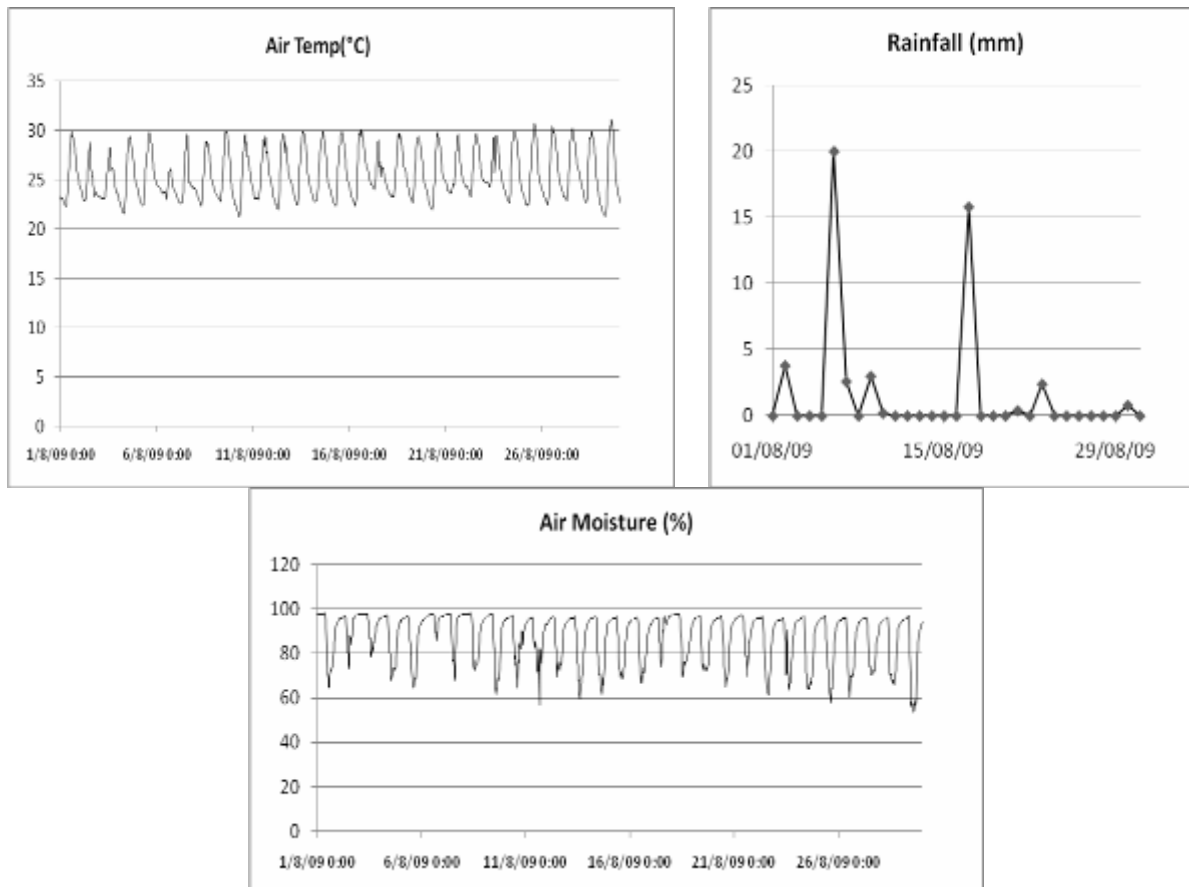


Figure 4-5: Air temperature, rainfall and air moisture at Paracou during the TropiSAR campaign.

#### 4.4. Soil moisture data

##### 4.4.1. Soil moisture data in Nouragues

Soil moisture was measured using a ML2x DeltaT Thetaprobe at 10 sites on Petit Plateau and 10 sites on Grand Plateau. To calibrate the probe, ca. 50 g of surface soil (0-5 cm below the superficial organic layer) was cored at the 20 sites. For each sample, the wet volume was measured, and the sample was weighed wet, and after being oven-dried during 36 h at 110°C. Near each core, a thetaprobe measurement was made. The calibration curve is reported in Figure 4-6. Measured soil moisture varied between 25 and 52%, and showed a very large heterogeneity over small spatial scales. The lowest soil moisture was encountered in the silt-



sand surface soil of Petit Plateau, while the clay-dominated soil of Grand Plateau held more water.

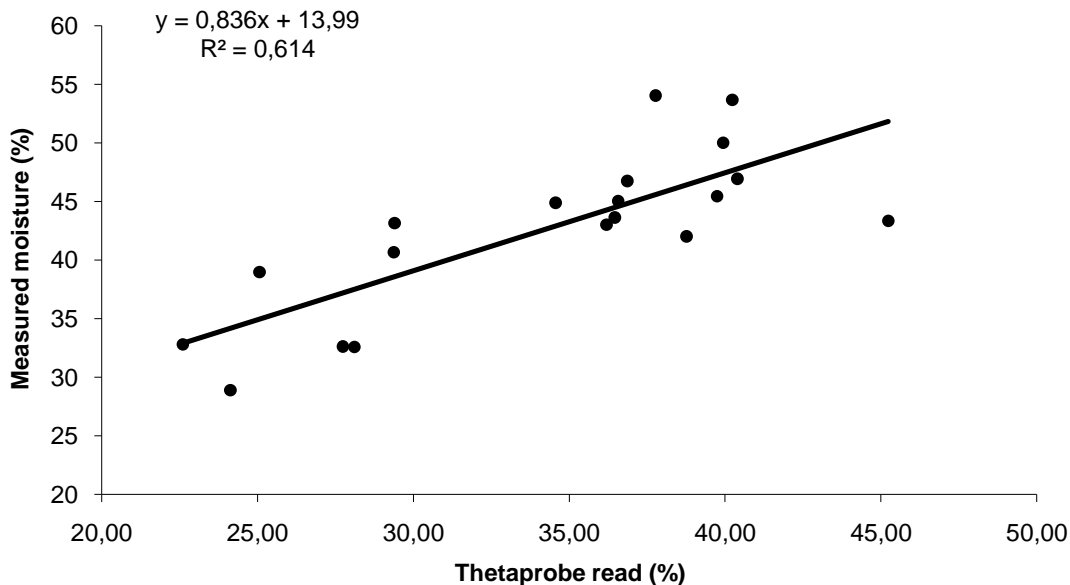


Figure 4-6: Calibration curve for the soil moisture measurement.

Mean soil moisture measurements at two of the Nouragues sites on two dates is presented in Table 4-2.

	Petit Plateau	Grand Plateau
18/08/09	41.1	43.4
24/08/09	38.6	38.33

Table 4-2: Mean soil moisture measurements on two dates

#### 4.4.2. Soil moisture in Paracou

Volumetric soil water content (SWC;  $\text{m}^3\text{m}^{-3}$ ) using a frequency domain sensor (CS615; Campbell Scientific Inc. at 0,10 cm depth were recorded. Data were collected at 1 min intervals and compiled as 30 min averages or sums with a CR23X datalogger (Campbell Scientific Inc.). Soil moisture ranged between 0,10 and 0,20  $\text{m}^3\text{m}^{-3}$ . Highest values were recorded just after the 2 rainy events : 6th august (from 8.30 to 12.30) and 17<sup>th</sup> august (from 13.00 to 15.30).



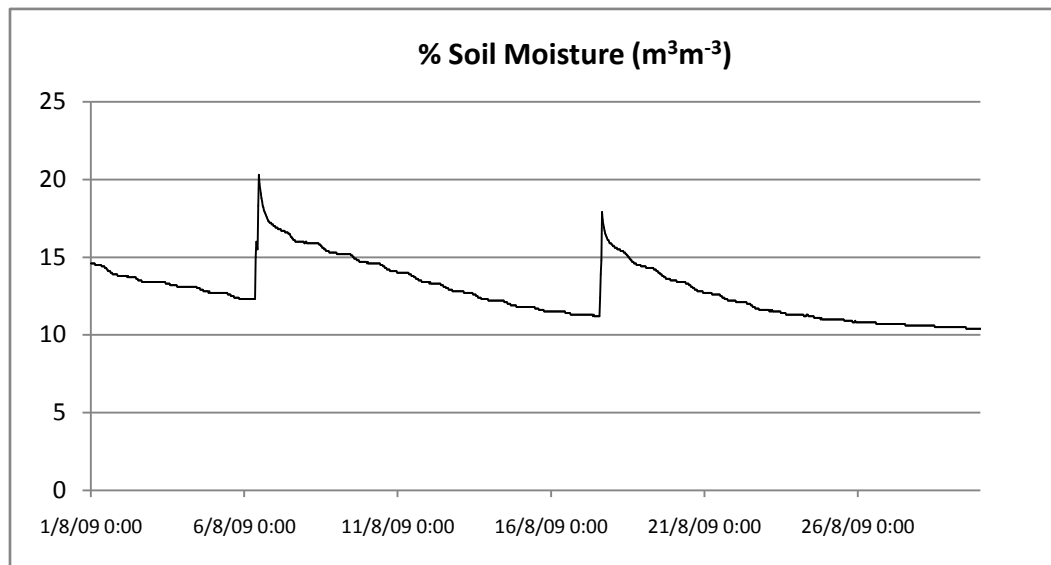


Figure 4-7: Soil moisture content in Paracou.

#### 4.5. LiDAR data

Two LiDAR acquisitions were conducted in 2004 and 2009. The LiDAR data was acquired using the ALTOA system (<http://www.altoa.fr/>). The ALTOA system includes a portable Riegl laser rangefinder (LMS6Q140i-60) embarked on a helicopter flying at a speed of about  $30 \text{ m s}^{-1}$  about 150 m above the ground. The system also consists of two dual-frequency GPS receivers coupled to an inertial navigation system, both systems ensuring that a sub-decimeter differential position can be calculated for the helicopter in post-processing. The rangefinder system is based on the principle of time-of-flight measurement of 30 kHz laser pulses in the infrared wavelength region ( $0.9 \mu\text{m}$ ). As laser beam divergence is 3 milliradians, the footprint is about of 0.22 m wide on the ground. The LiDAR dataset consisted of a cloud of laser echoes originating from terrain and vegetation. For each point, latitude, longitude and elevation are measured in metres and stored into a file. The datum used is WGS84 and the projection North UTM zone 22.

Depending of the campaign the average laser pulse density was c. 4 imp/m<sup>2</sup> (2004 to 2008) or 8 imp/m<sup>2</sup> (2009). Acquisition were all conducted in last return mode to maximise penetration (the system used did not have multiple return registering capacity). A major challenge in dense tropical forest is the penetration of Laser impulse which directly affects the precision of the Digital Elevation Model which it self will determine the precision of the canopy height data.

Two precise DEMs over both Paracou and Nouragues areas were established from the LiDAR data. At the same time a Canopy height model was also computed.

**The LiDAR data was acquired and processed under the Guyafor project and will not be included as part of the TropiSAR delivery; However, special request can be filed with Lilian Blanc, Guyafor principal investigator**



## 4.6. Illustrations

### 4.6.1. Nouragues



Figure 4-8: Forest view from the Inselberg.





Figure 4-9: Grand Plateau Area (Note the lianas and the Chablis area).





Figure 4-10: Petit Plateau area.





#### 4.6.2. Paracou



Figure 4-11: Plot 6 (no Treatment) ; *Vouacapoua americana* on the right.



Figure 4-12: Bois cathédrale (*Chimarrhis turbinata*) on Plot 1, Plot 15 and Plot 11.





Figure 4-13: Plot 9, Plot 2, Plot 2, (Treatment 1).



Figure 4-14: Plot 10 (Treatment 2).





Figure 4-15: Plot 12 with a *Cecropia* tree, pioneer species in the left picture (Treatment 3).



Figure 4-16: Plot 4 (Treatment 3).



## 5. TROPISAR DATASET

### 5.1. Ground measurement data set

The deliverables contain the total AGB (in Mg) stored in subplots of  $25 \times 25$  m,  $50 \times 50$  m and  $100 \times 100$  m (for the Nouragues plots and plot 16 of Paracou) or  $250 \times 250$  m (for the plots of Paracou and Arboce). Files are provided separately for each plot larger than 1 ha and AGB estimation at the different spatial resolution can be assessed within each sheet of the file (Table 5-1).

	A	B	C
1	X	Y	AGB
2	312613.528	449731.024	26.13615842
3	312586.348	449731.973	32.23908904
4	312559.168	449732.921	29.39309137
5	312531.988	449733.87	20.06523663
6	312613.234	449756.108	32.82361184
7	312586.285	449756.999	24.14494277
8	312559.336	449757.889	16.95186172
9	312532.387	449758.779	25.11972809
10	312612.94	449781.192	15.86285241
11	312586.222	449782.025	15.78132292
12	312559.503	449782.857	13.6187645
13	312532.785	449783.689	79.68480172
14	312612.645	449806.276	31.13276261
15	312586.158	449807.05	26.70372717

Navigation icons: back, forward, first, last, search, and a zoom control showing 25, 50, and 100 meters.

Table 5-1: Example of file that contains estimation of the above ground biomass (Mg) stored in each plot. Geographical coordinates of the center of each subplot follow the UTM WSG 84 22N. The different spatial resolution of biomass estimation can be assessed within each sheet of the file.

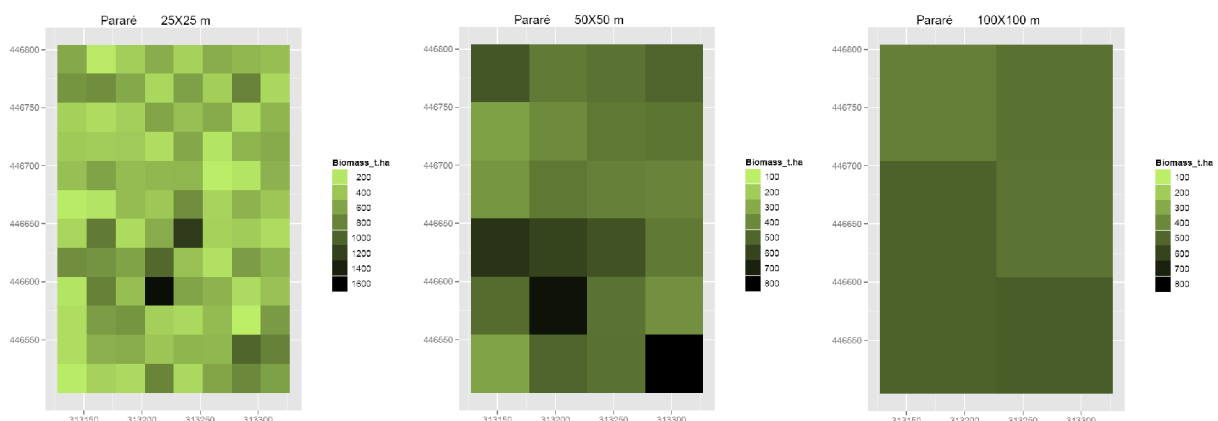


Figure 5-1: Example of map that illustrates the variation in space in biomass (tons per ha) at different spatial resolution ( $25 \times 25$  m,  $50 \times 50$  m,  $100 \times 100$  m). Similar maps have been provided to the TropiSAR project for each plot.



## 5.2. Radar dataset

In the next table, the different processed acquisitions are identified for the four different sites: Arbocel, Kaw, Paracou and Nouragues.

Altogether, we processed and calibrated 37 polarimetric datasets, 8 at L-Band and 29 at P-Band adding up to more than 110 GB of data. The list of the processed images is provided in the following table.

SITE	FREQUENCY BAND	ACQUISITION IDENTIFIER	TRAJECTORY	PLANNED LINE
Arbocel	P_Band	tropi0108	CONS	BZ
Arbocel	P_Band	tropi0307	CONS	BZ
Arbocel	P_Band	tropi0408	CONS	BZ
Kaw	P_Band	tropi0509	PROP	BZ
Paracou	L_Band	tropi0402	CONS	BZ
Paracou	L_Band	tropi0403	PROP	B1
Paracou	L_Band	tropi0404	PROP	B2
Paracou	L_Band	tropi0405	PROP	B3
Paracou	L_Band	tropi0406	PROP	B4
Paracou	L_Band	tropi0407	PROP	B5
Paracou	L_Band	tropi0506	CONS	BZ
Paracou	L_Band	tropi0603	CONS	BZ
Paracou	P_Band	tropi0007	CONS	BZ
Paracou	P_Band	tropi0104	CONS	BZ
Paracou	P_Band	tropi0208	CONS	BZ
Paracou	P_Band	tropi0305	CONS	BZ
Paracou	P_Band	tropi0402	CONS	BZ
Paracou	P_Band	tropi0403	PROP/PROJ	B1
Paracou	P_Band	tropi0404	PROP/PROJ	B2
Paracou	P_Band	tropi0405	PROP/PROJ	B3
Paracou	P_Band	tropi0406	PROP/PROJ	B4
Paracou	P_Band	tropi0407	PROP/PROJ	B5
Paracou	P_Band	tropi0506	CONS	BZ
Paracou	P_Band	tropi0507	CONS	B1
Paracou	P_Band	tropi0603	CONS	BZ
Nouragues 1	P_Band	tropi0101	CONS	BZ
Nouragues 1	P_Band	tropi0201	CONS	BZ
Nouragues 1	P_Band	tropi0204	PROP/PROJ	B2
Nouragues 1	P_Band	tropi0205	PROP/PROJ	B3
Nouragues 1	P_Band	tropi0206	PROP/PROJ	B4
Nouragues 1	P_Band	tropi0207	PROP/PROJ	B5
Nouragues 2	P_Band	tropi0303	CONS	BZ
Nouragues 2	P_Band	tropi0304b	CONS	B1
Nouragues 1	P_Band	tropi0501	CONS	BZ
Nouragues 1Bis	P_Band	tropi0607	PROP	BZ
Nouragues 1Bis	P_Band	tropi0608	PROP	B1
Nouragues 1	P_Band	tropi0609	CONS	BZ

Table 5-2: Processed Radar data per site.





All SAR processing are performed using the flown trajectory. However, the processor allows the operator to choose the straight trajectory which will be used to provide the geometry of the slant range image. This fitted straight trajectory can come from different sources.

**CONS:** processed with respect to the reference trajectory BZ, an ideal straight line which the pilots tried to follow when flying the zero baseline acquisition.

**PROP:** processed with respect to a straight trajectory adjusted to the flown trajectory

**PROJ:** Processed with respect to a straight trajectory adjusted to the flown trajectory and projected into the geometry of the CONS acquisition

These different processing scenarios are selected to provide the best possible data for the different applications. A recommendation concerning which product to use depending on the applications is presented in the next paragraph.

### 5.2.1. SLC products

In order to cover the different potential use of the data, we had decided in agreement with ESA, to process the data following two strategies, called CONS and PROP.

**CONS:** The Zero-baseline data was processed using a common geometry associated with the reference trajectory at zero-baseline. These images are identified with a 'CONS' in their name (CONS as in consign). All the 'CONS' images from one site have the same geometry and interferograms can be computed directly between any two images.

Some images acquired with a non-zero baseline were also computed in the reference trajectory geometry. The advantage is then that the interferometric applications are easily implemented at the cost of a slight degradation in the image quality parameters.

**PROP:** When the baseline becomes more important, this approach is not acceptable and we decided to compute each dataset in the radar geometry associated with the flown trajectory. These images are identified with a 'PROP' in the file name. (PROP stands for proper or self). Interferometric applications on these images require to first coregister the data. They do not share a common geometry.

In order to facilitate interferometry and tomography with these images, they are projected in a common geometry, usually selected to be the one associated with the ZB image. These images are identified with 'PROJ' in their names.

SLC geometry	CONS	PROP	PROJ
<b>Radiometry and polarimetry</b>	Recommended for ZB acquisition	Recommended for non-zero baseline	Not recommended
<b>Interferometry</b>	Recommended for ZB	Requires co-registration	Recommended for non-zero baseline
<b>Tomography</b>		Requires co-registration	Recommended
<b>ROI analysis</b>	Same position	Different image position	Position associated with the reference image.
<b>Summary</b>	Best suited for temporal analysis at zero baseline – All CONS images share the same geometry making	Best quality image but the geometry is different from one image to the next. The ROI files are different for	Best suited for PolInSAR and tomography.





	the comparison between acquisitions easy	every set and the user might have to perform co-registration.	
--	--	---	--

Table 5-3: Recommendation of SAR format as a function of applications.

The tomographic or interferometric sets include an ambiguity height file with respect to the reference image.

### 5.2.2. Geocoded radar products

The images are projected in a WGS84 UTM zone 22 grid with a 1m pixel spacing. The format is unsigned short integer and the coded value corresponds to Sigma0 in linear format (amplitude). The header provides the UTM coordinates of the origin point.

We have geocoded the following images: at least, one for each site and flight line.

Site	Flight line	Image name
Paracou	Paracou	tropi0402
Arbocel	Arbocel	tropi0108
Nouragues	Nouragues 1	tropi0201
Nouragues	Nouragues 1b	tropi0607
Nouragues	Nouragues 2	tropi0303
Kaw	Kaw	tropi0509

Table 5-4: Geocoded images at P band.

Site	Flight line	Image name
Paracou	Paracou	tropi0402
Arbocel	Arbocel	NA
Nouragues	Nouragues 1	NA
Nouragues	Nouragues 1b	NA
Nouragues	Nouragues 2	NA
Kaw	Kaw	tropi0509

Table 5-5: Geocoded images at L-Band.

A detailed description of the radar data format is provided in Annex B.

### 5.2.3. Region of interest

In order to facilitate the selection of the studied plots, we created the “region of interest” files, there are in the Envi format (.roi) and can be directly open via the ENVI/IDL software. They are 16 plots in Paracou, 24 in Nouragues (depending on the flight lines) and 1 in Arbocel. One roi file is computed for each of the datatake. A .txt file is also available, which provides the (i,j) image position of the boundary of the different plots. Each side of one ROI is defined with up to 64 points. The boundaries are not straight lines on the radar image when the topography is rugged. When a DEM is available in the area, the image coordinates (i,j) are



computed based on the geographic coordinates and the ellipsoidal height from the LiDAR measurements. This height is also reported in the .txt file.

### 5.2.3.1. Description of the txt file

In Annex B, we provide the four corner coordinates of each ROI in WGS84 geographic coordinates, UTM projection, zone 22, altitude (Hayford 1909 , NGG77) et ellipsoidal height (IAG GRS80, RGFG85) and image pixel coordinates in the reference (ZB geometry) image tropi0007 for Paracou and tropi0201 for Nouragues 1.

Furthermore, together with the SLC data, we deliver a txt file positioning the ROI's in the image. A description of this txt file is provided in the following.

```

*Résultat de la transformation de type Standard entre:
*SYSTEME :   Guyane : RGFG95
*COORDONNÉES : Planes
*ELLIPSOÏDE : GRS 1980
*PROJECTION : UTM Nord fuseau 22 (RGFG95)

*SYSTEME :   Guyane : RGFG95
*COORDONNÉES : Géographiques
*ELLIPSOÏDE : GRS 1980
*MERIDIEN :   Greenwich
*UNITE :      Degrés décimaux

*SYSTEME ALTIMETRIQUE :   NGG 1977 (Guyane)
  
```

Header with description of the geographic transformation system

```

* Latitude  Longitude  Hauteur  Azimut  Range
* ROIPPE20
4.084722 -52.684441 79.211998 1063.953356 230.310661
4.084686 -52.684369 78.762001 1067.265357 234.609542
4.084650 -52.684288 77.092003 1070.590142 240.485241
4.084614 -52.684207 74.751999 1073.915152 246.933384
...
4.084577 -52.684540 78.942001 1076.665861 224.999980
4.084649 -52.684495 79.092003 1070.302995 227.396208
4.084722 -52.684441 79.211998 1063.953356 230.310661
* ROIPPF20
4.084362 -52.683648 76.820999 1097.172142 276.027889
4.084326 -52.683576 77.611000 1100.483691 279.376910
4.084290 -52.683494 77.981003 1103.807734 283.598865
...
* ROIPPF21
...
* ROIGPM11
...
  
```

Indication of the table

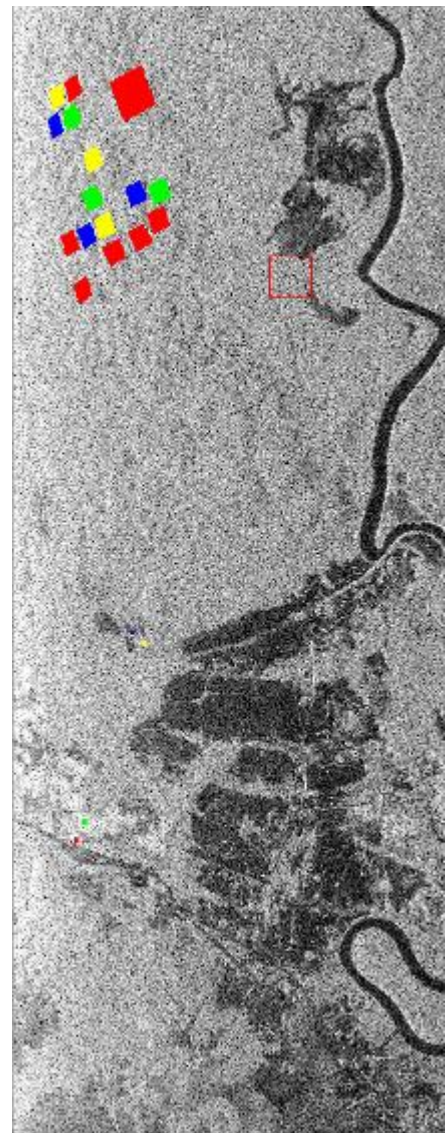
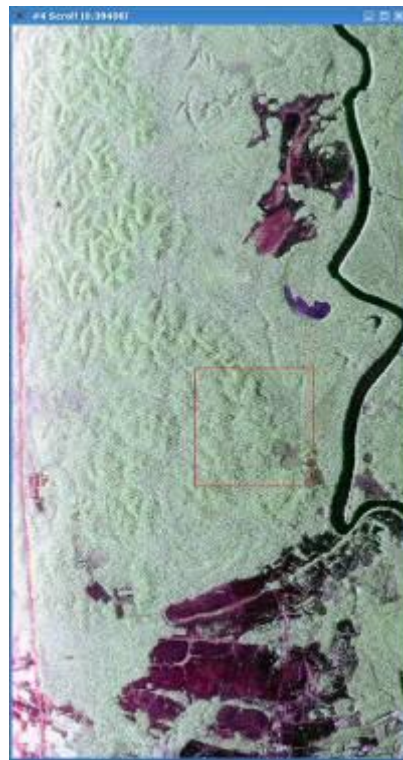
N coordinate lines correspondent of vertexes

All ROIs

Figure 5-2: Example of the text file based on the ROI\_Nouragues1\_tropi0201\_Pcons.



#### 5.2.4. SAR images over Paracou



Tropi0007  
RGB (Hh, Hv, Vv)

Tropi0007  
RGB Pauli

Tropi0506  
Hh with the 19 Rois

This image (tropi0007) was used as a reference in the temporal analysis.





Tropi0104  
RGB (HH, HV, VV)



Tropi0208  
RGB (HH, HV, VV)



Tropi0305  
RGB (HH, HV, VV)



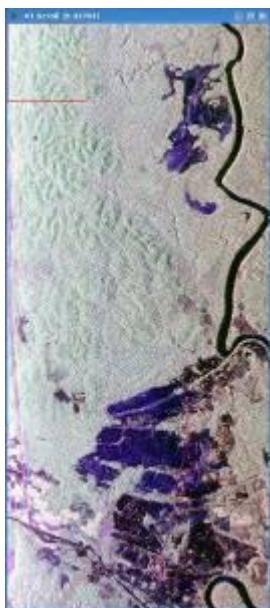
Tropi0402  
RGB (Hh, Hv, Vv)



Tropi0403  
RGB (Hh, Hv, Vv)



Tropi0404  
RGB (Hh, Hv, Vv)



Tropsar0405  
RGB (Hh, Hv, Vv)



Tropsar0406  
RGB (Hh, Hv, Vv)

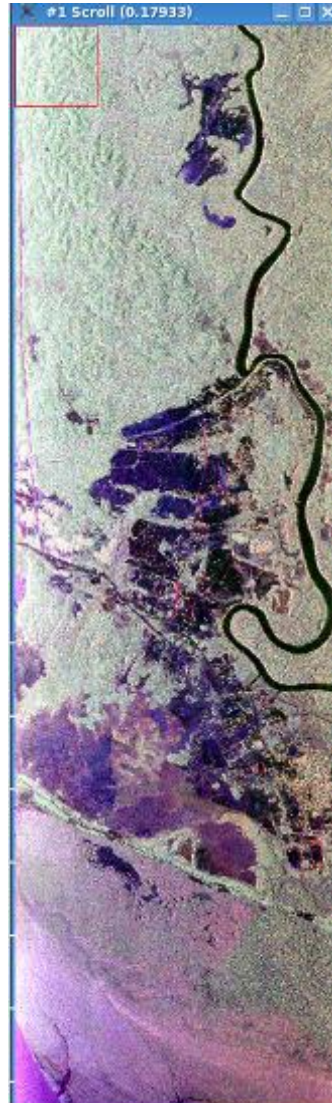


Tropsar0407  
RGB (Hh, Hv, Vv)





Tropi0506  
RGB (Hh, Hv, Vv)



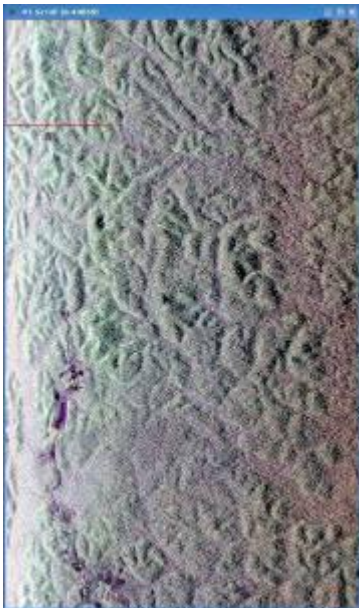
Tropi0507  
RGB (Hh, Hv, Vv)



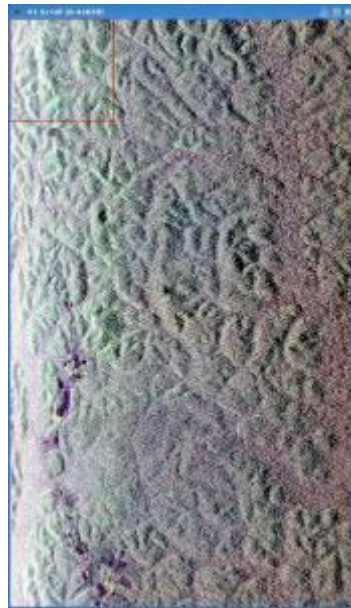
Tropi0603  
RGB (Hh, Hv, Vv)



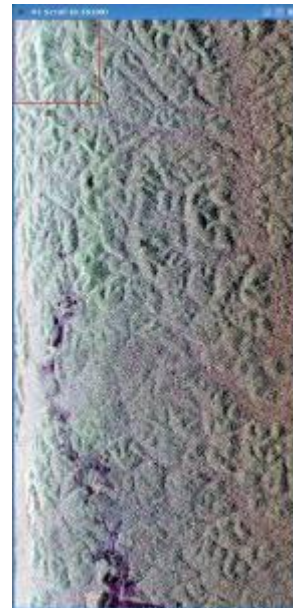
### 5.2.5. SAR images over Arbocel



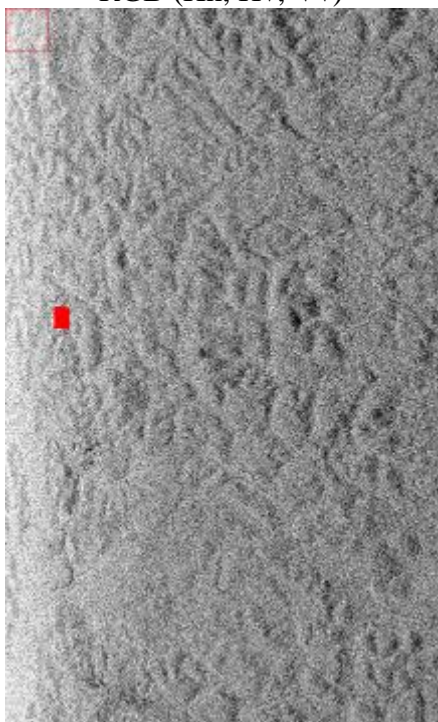
Tropi0108  
RGB (Hh, Hv, Vv)



Tropi0307  
RGB (Hh, Hv, Vv)



Tropi0408  
RGB (Hh, Hv, Vv)

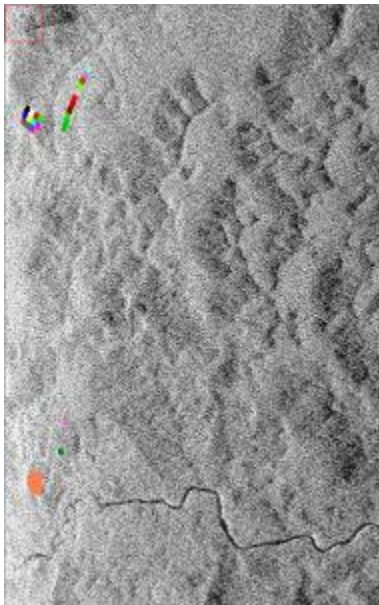


Tropi0108 with the ROI

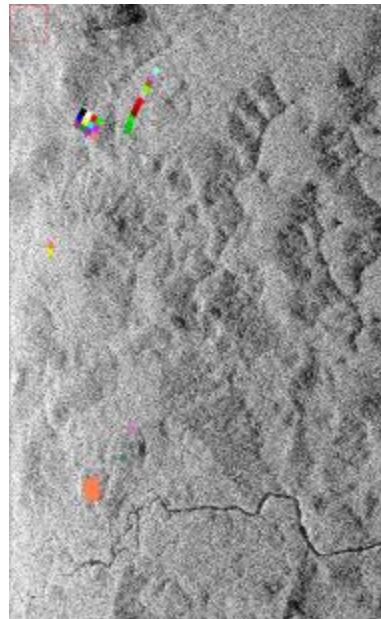




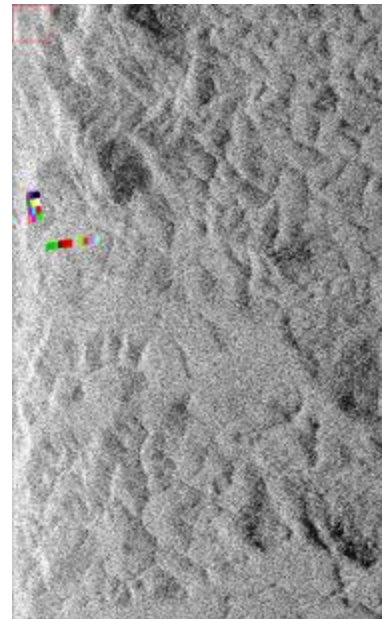
### 5.2.6. SAR images over Nouragues



Nouragues 1  
Tropi0201

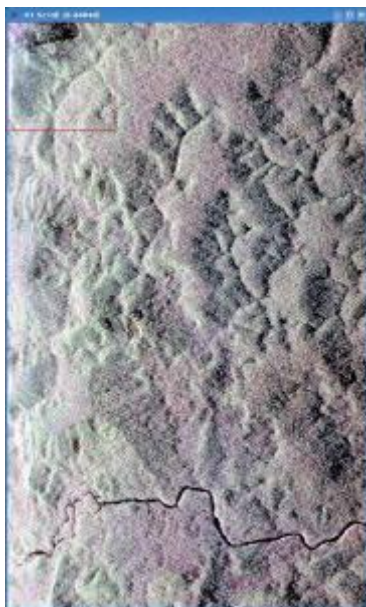


Nouragues 1 bis  
Tropi0607

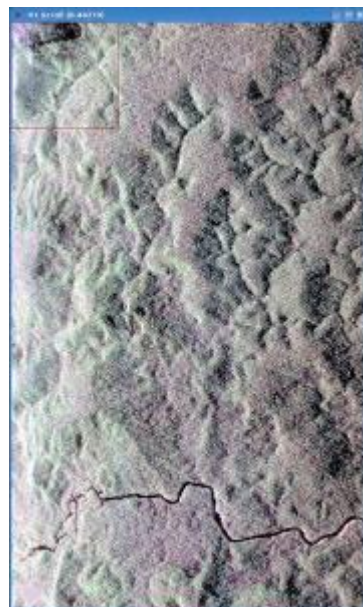


Nouragues 2  
Tropi0303

#### 5.2.6.1. Nouragues 1



Tropi0201  
RGB (Hh, Hv, Vv)

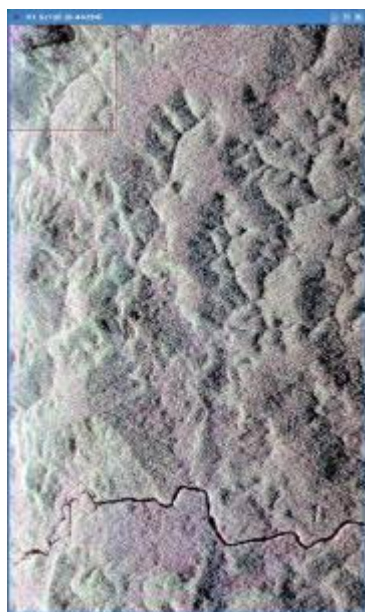


Tropi0204  
RGB (Hh, Hv, Vv)

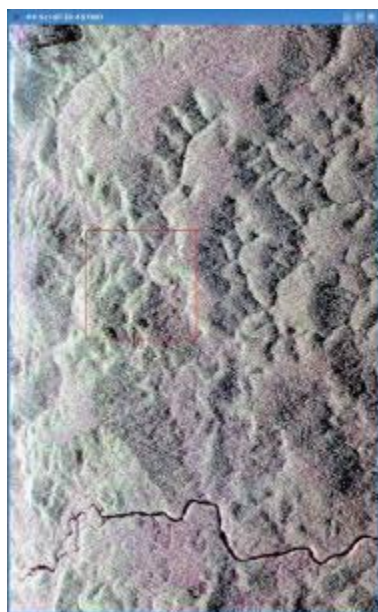


Tropi0205  
RGB (Hh, Hv, Vv)

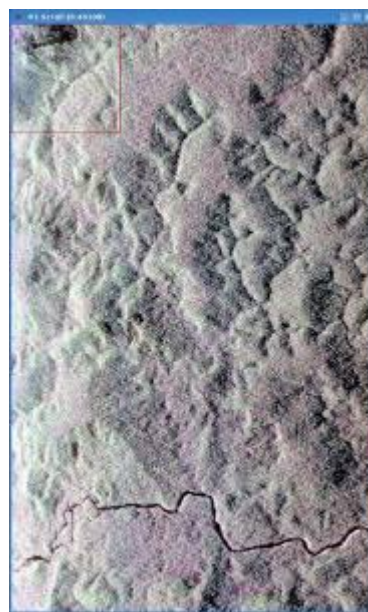




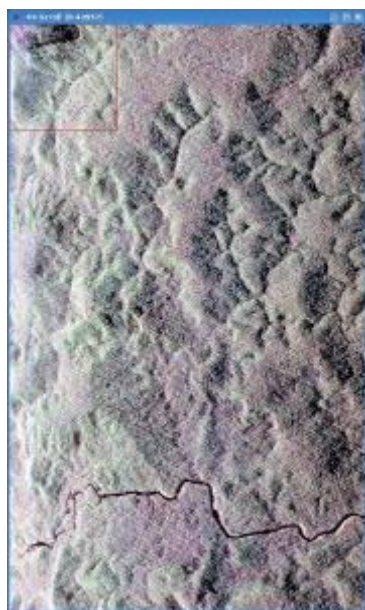
Tropi0206  
RGB (Hh, Hv, Vv)



Tropi0101  
RGB (Hh, Hv, Vv)



Tropi0207  
RGB (Hh, Hv, Vv)



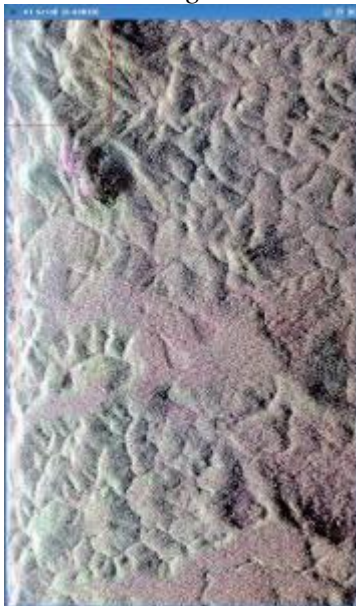
Tropi0501  
RGB (Hh, Hv, Vv)



Tropi0609  
RGB (Hh, Hv, Vv)

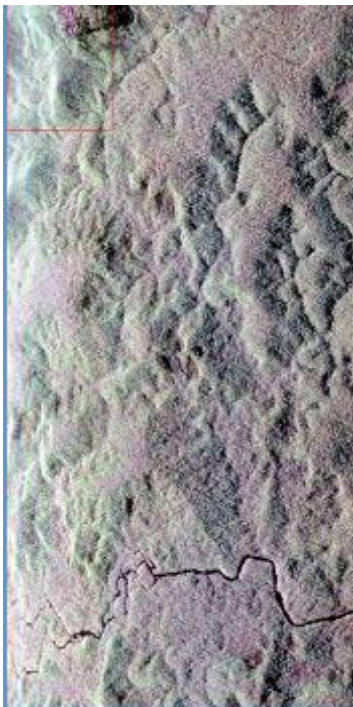


### 5.2.6.2. *Nouragues 2*



Tropi0303  
RGB (Hh, Hv, Vv)

### 5.2.6.3. *Nouragues Ibis*



Tropi0607  
RGB (Hh, Hv, Vv)



Tropi0608  
RGB (Hh, Hv, Vv)





### 5.2.7. SAR images over Kaw



Tropi0509  
RGB (Hh, Hv, Vv)

### 5.3. Description of the summary file

This file is an excel file which is part of the delivery. It contains the in-situ measurements as well as the radar measurements.

The radar data contains one sheet per radar SLC image with the sigma0, gamma0 value per ROI organised in sheets with a sheet per radar image.



## 6. TROPISAR DATA ANALYSIS – GROUND MEASUREMENTS – ERROR ANALYSIS

### 6.1. Methods for above ground biomass estimation

#### 6.1.1. Allometric equations

Most tropical forest biomass estimates based on forestry censuses make use of allometric equations to convert measured dimensions (diameter at breast height, henceforth *DBH*, and/or total tree height) into an aboveground biomass (*AGB*) for each tree in the sample. Plot-wide estimates are then simply obtained by summing over the biomass estimates of individual trees.

[Chave, 2005] proposed a set of tree biomass allometries for a number of tropical rain forest types. French Guiana rain forests are characterized by a 2-month dry season, and may therefore be classified as moist rain forests. Hereafter, we only consider the equations applicable for moist tropical forests. These equations are based on 1504 trees directly harvested and compiled from several literature sources. For each tree, a direct measure of *DBH* (in cm) and of *AGB* (in kg), as well as a measure of wood specific gravity (*WSG*, in  $\text{g cm}^{-3}$ ) is available. One can therefore infer the *AGB* of any tree based on the following model:

$$AGB = WSG \times \exp(-1.499 + 2.148 \times \ln(DBH) + 0.207 \times \ln(DBH)^2 - 0.0281 \times \ln(DBH)^3)$$

In order to assess the consistency of *AGB* estimation using different allometric models, we also used an allometric model including information on *DBH*, *WSG* and tree height (*H*) [Chave, 2005]:

$$AGB(H) = 0.0509 \times WSG \times DBH^2 \times H$$

This model was applied to 6 subplot of 1 ha in which all trees were measured for their total tree height.

The *AGB* of plantation trees and palms were estimated with species-specific allometric models [Brown, 1997]. For the *Cocos nucifera* plantation we used a model originally developed on an abundant palm species of Puerto Rico, *Pretoaia Montana* [Frangi, 1985]:

$$AGB = 10 + 6.4 * H$$

For *Pinus caribaea* plantations we used an allometry obtained by compiling several harvest studies on trees in the genus *Pinus* [Brown, 1997]:

$$AGB = \exp(-1.17 + 2.2119 \times \ln(DBH))$$



### 6.1.2. Wood density

WSG, the oven-dry weight of wood divided by its green volume, varies from ca. 0.2 in the lightest woods to over 1.2 [Williamson, 2010]. There is a strong species-specific determinism in wood density. We therefore inferred WSG not from field data but from large database that provide mean WSG for species. In this contribution we used the DRYAD data base, that come from a large compilation of wood density measurement [Chave, 2009] but we considered only measures that were made in tropical region of South America (n=4182) in order to limit the bias due to regional variation of wood density [Muller-Landau, 2004, Chave, 2006]. When no reliable species identification or no wood density information at the species level was available, the general mean wood density at upper taxonomical levels (*i.e.* genus, family, order and global) was attributed to the tree. Here the assumption is that closely related species shows more similar wood density values than expected by chance [Chave, 2006].

### 6.1.3. Estimating the error in AGB measurement

Three main sources of errors can be identified: i) errors and/or biases in field measurements,

ii) errors associated to the allometric model [Chave, 2004] and iii) errors associated to the representativeness of the plot (*i.e.* size of the plot).

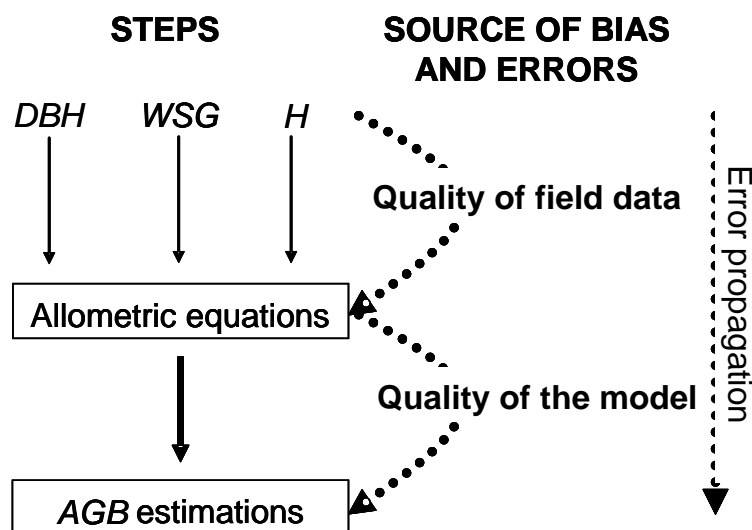


Figure 6-1: Steps of above ground biomass estimation and their bias and/or errors associated.

Figure 6-1 shows the different steps to convert forest plot data into AGB estimation. Errors may creep in the final AGB estimation due to error in measuring *DBH*, in estimating *WSG*, and – if available – in estimating tree height (*H*). Previous studies show that the major source of error in AGB estimation is attributed to the allometric model [Chave, 2004; Quentin Molto comm. Pers.].



To assess the uncertainties associated to the allometric equation, we used the original dataset that was compiled to design the allometric equation, and we bootstrapped this dataset. More precisely, we then drew 1504 trees from the original dataset of 1504 trees but one by one and with replacement. This amounts to picking some trees more than once and to ignore other trees in the analysis. We then constructed 1,000 bootstrapped allometric biomass equations, which we used to estimate the AGB of each plot. This yielded a standard deviation across AGB estimates, and 95% confidence limits (2.5% and 97.5% confidence limits). We did not perform the error estimation on plantations, but we expect that the error is typically smaller than that on unmanaged old-growth mixed forests.

We then estimated the errors associated to the sampling size of the plots. As AGB distribution across subplots  $\geq 0.25$  ha approaches normality (Figure 6-2) [Chave, 2003], the error structure due to sampling size should be as:

$$CV_{size} = \frac{b}{\sqrt{A}}$$

where  $A$  is the plot size (in ha), and  $b$  is the coefficient of variation of 1-ha subplots. To estimate  $b$ , we subsampled all the study plots, excepting plots inferior to 1 ha, using 50x50 m subplots. We thus obtained 624 subplots of 0.25 ha in which we estimated AGB (Figure 6-2).

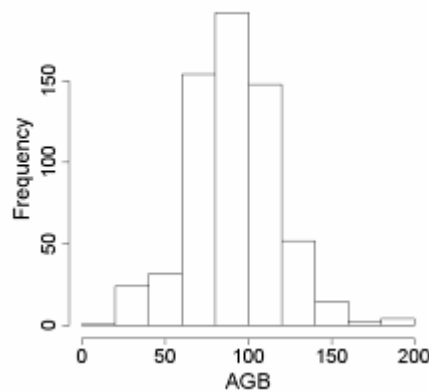


Figure 6-2: Histogram of the AGB values in the 624 0.25-ha subplots.

We estimated that  $b$  was equal to 9.47 using the following equation:

$$b = \frac{\sum_{i=1}^n CV(0.25)_i}{2n} ..$$

where  $CV(0.25)_i$  is the coefficient of variation of 0.25-ha subplots within the plot  $i$  and  $n$  is the total number of plots ( $n=22$ ).

The total error associated to AGB estimates ( $CV_{total}$ ) can thus be estimated as following:





$$CV_{total} = \sqrt{CV_{allom}^2 + CV_{size}^2}$$

where  $CV_{allom}$  corresponds to the error due to the allometric model (mean of  $CV_{allom}=2.35$ ). We were thus able to model the structure of the total error according to plot size (Figure 6-3).

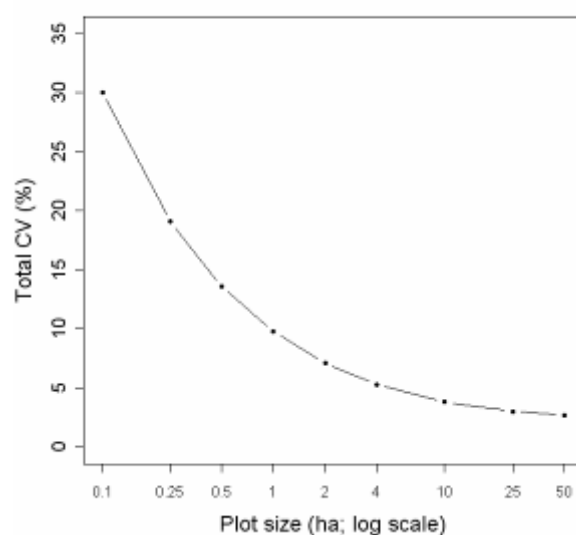


Figure 6-3: Errors associated to the sampling size in percent (CV).

## 6.2. Above-ground biomass in the ground plots

The AGB estimation of the 28 study sites covered a large range of values, ranging from 10.6 to 485.7 t/ha (Table 6-2).

Site	Plot	Plot size (ha)	AGB (t/ha)	SD	2.5%CL	97%CL
Paracou	Plot 1	6.25	369.6	5.9	355.6	378.2
Paracou	Plot 2	6.25	346.4	5.3	334.1	354.4
Paracou	Plot 3	6.25	309.0	4.1	300.2	315.8
Paracou	Plot 4	6.25	284.7	3.6	277.7	291.5
Paracou	Plot 5	6.25	300.5	3.9	292.7	307.5
Paracou	Plot 6	6.25	431.9	7.8	411.7	442.6
Paracou	Plot 7	6.25	392.4	6.4	377.0	401.7
Paracou	Plot 8	6.25	257.5	3.2	251.2	263.5
Paracou	Plot 9	6.25	337.5	4.8	326.9	345.0
Paracou	Plot 10	6.25	307.5	4.1	299.1	314.6
Paracou	Plot 11	6.25	402.7	6.3	388.0	412.2
Paracou	Plot 12	6.25	304.3	4.0	296.4	311.5
Paracou	Plot 13	6.25	405.3	6.5	389.7	414.8
Paracou	Plot 14	6.25	407.7	6.5	392.1	417.4
Paracou	Plot 15	6.25	417.8	6.6	402.3	427.6



<b>Paracou</b>	Plot 16	25	406.1	8.6	383.1	415.9
<b>Paracou</b>	Pinus plantation 1	0.49	284.7			
<b>Paracou</b>	Pinus plantation 2	0.49	303.5			
<b>Paracou</b>	Coco plantation	0.25	10.6			
<b>Paracou</b>	Secondary forest	0.28	186.4	2.2	182.5	191.0
<b>Paracou</b>	Flooded forest 1	0.5	286.3	3.7	277.9	292.7
<b>Paracou</b>	Flooded forest 2	0.5	485.7	9.6	459.8	497.9
<b>Paracou</b>	Arbocel	6.25	120.1	1.3	118.3	123.2
<b>Nouragues</b>	Petit plateau	12	427.4	10.3	398.3	439.1
<b>Nouragues</b>	Grand plateau	10	375.7	10.7	346.1	387.4
<b>Nouragues</b>	Pararé	6	483.0	15.4	439.4	499.3
<b>Nouragues</b>	Balanfois	2	445.7	12.5	409.6	457.5
<b>Nouragues</b>	Pararé-ridge	1	465.9	13.5	428.5	480.4

Table 6-1: Estimation of the above ground biomass (Mg.ha<sup>-1</sup>) stored in each plot, with error estimates.

With the 6 1-ha plots where all trees heights were measured (n=3029), we compared two AGB estimation models: one without tree height (AGB in Table 6-2) and one with tree height (AGB(H) in Table 6-2, see above). The AGB estimation model that explicitly incorporate tree height measures in biomass calculations led to systematically lower AGB estimates than those obtained with the model that without height. However, the differences between the two models did not exceed 9% of the mean.

Site	Plot name	Ntree	Mean tree height	SD tree height	AGB without tree height	AGB with tree height	% Error
<b>Paracou</b>	Plot 6	593	19.94	6.17	376.49	344.1	<b>8.6</b>
<b>Nouragues</b>	Grand Plateau	462	20.37	8.23	466.25	447.25	<b>4.08</b>
<b>Nouragues</b>	Petit Plateau	483	19.58	8.42	520.49	483.17	<b>7.17</b>
<b>Nouragues</b>	Balanfois	533	21.68	8.02	480.12	464.4	<b>3.27</b>
<b>Nouragues</b>	Pararé	474	21.9	7.88	461.23	430.07	<b>6.76</b>
<b>Nouragues</b>	Pararé ridge	484	21.48	7.74	465.85	437.87	<b>6.01</b>

Table 6-2: AGB estimation based on DBH, and based on both DBH and total tree height. Ntree is the number of trees measured in each plot. % Error is the error between the two measurements (in %).

### 6.3. Discussion and perspectives

This contribution aimed at providing accurate estimation of above ground biomass from ground data.

First we underestimated the true AGB of the stand because we discarded trees < 10 DBH and lianas. Previous studies showed that trees comprised between 1 and 10 cm DBH accounted for 5% of the total AGB stored while lianas accounted for 3% [Chave, 2003]. Hence it is unlikely that this AGB pool will contribute more than 10% of the total AGB stock. Another stock is due to the dead standing trees, which are rarely measured in forestry inventories. This term may make a substantial contribution to AGB especially in recently



disturbed stands, and it would be important to further quantify this term in the future. However, it is debatable whether P-band radar sensor will 'see' such obstacles.

Estimating tree height in the field was found to be a challenging task because it is often hard to clearly identify the top leaf or branch of a tree in the canopy. Hence, tree height measurements often underestimate the real tree height. Then, we argue that a large part of differences between the two models may be attributable to an underestimation of tree height in the field, though other explanations, such as a bias in the allometry, cannot be discarded. Further work is however needed to improve the accuracy of biomass estimation when tree height information is missing. Particularly, understanding the determinant of tree height in our study area will considerably improve our ability to take into account these biases.



## 7. TROPISAR DATA ANALYSIS – POLSAR ANALYSIS

In this section, polarimetric TropiSAR backscatter data are analyzed. The analysis concerns data of different dates over the two main test sites which are Paracou and Nouragues. However, the report includes mainly the results on Paracou test site, the data over Nouragues required further analysis. The extracted backscatter measurements are subsequently analyzed as a function of in-situ biomass values reported in Sections 4 and 6.

### 7.1. Extraction of the backscattered intensities from SETHI data

The measurements of backscatter intensities are the backscattering coefficients for distributed target. These coefficients are derived from the brightness coefficient (the averaged radar-cross section per unit image area) which definition [Raney, 1994] leads to Equation (7.1) with:

- $S_{qp}$  : the complex number taken from the 'tropi[xxxx]\_Pcons\_[qp]\_slc' files, the indice qp indicates the transmit and receive polarization horizontal 'H' or the vertical 'V' polarization.
- $A_s$ : the slant range surface resolution given in the files 'tropi[xxxx]\_Pcons\_qp\_slc.ent
- $\langle \cdot \rangle$  indicates the spatial average over the image pixels (i,j) over the region of interest (ROI).

With this notation, the coefficients  $S_{qp}$  are the scattering matrix coefficients divided by  $4\pi$ . From the physical point of view, the  $S_{qp}$  coefficients can thus be used to relate the scattered field to the incident field, as shown by Equations (7.2) and (7.3).

Using the same notations as for the brightness coefficient, the intensities  $\sigma_{qp}^0$ ,  $\gamma_{qp}^0$  and  $\alpha_{qp}^0$  can be defined respectively by Equations (7.6), (7.7) and (7.8).





$$\beta_{qp}^0(dB) = 10 \log_{10} \frac{\langle |S_{qp}|^2 \rangle}{A_s} \quad (7.1)$$

$$[S] = \begin{bmatrix} S_{Hh} & S_{Vh} \\ S_{Hv} & S_{Vv} \end{bmatrix} \quad (7.2)$$

$$\vec{E}^s = \frac{e^{jkr}}{r} \cdot \frac{1}{4\pi} [S]_{h,v} \cdot \vec{E}^i \quad (7.3)$$

$$\vec{E}^s = \begin{bmatrix} E_h \\ E_v \end{bmatrix} = \frac{e^{jkr}}{r} \cdot \frac{1}{4\pi} \begin{bmatrix} S_{Hh}E_H + S_{Vh}E_V \\ S_{Hv}E_H + S_{Vv}E_V \end{bmatrix} \quad (7.4)$$

$$\beta^0 = \frac{4\pi}{A_s} \frac{\langle |rE^s|^2 \rangle}{\langle |E^i|^2 \rangle} \quad (7.5)$$

$$\sigma_{qp}^0(dB) = 10 \log_{10} \left\langle \frac{|S_{qp}|^2}{A_s / \sin \theta_T} \right\rangle \quad (7.6)$$

$$\gamma_{qp}^0(dB) = 10 \log_{10} \left\langle \frac{|S_{qp}|^2}{A_s / \tan \theta_T} \right\rangle \quad (7.7)$$

$$\alpha_{qp}^0(dB) = 10 \log_{10} \left\langle \frac{|S_{qp}|^2}{A_s \cos^2 \theta_T / \sin \theta_T} \right\rangle \quad (7.8)$$

In relations (7.6) to (7.8), the parameter  $\theta_T$  matches the elevation angle, defined as shown in figure 7.1 and 7.2. Important to note is that these formulae should consider local angles (e.g  $\theta_i$  the local incident angle) as long as they can be derived from ancillary data (e.g DEM), as shown in paragraph 7.2.

Nonetheless, the use of the elevation angle in the formulation of  $\sigma_{qp}^0$ ,  $\gamma_{qp}^0$ ,  $\alpha_{qp}^0$  and especially in  $\gamma_{qp}^0$  and  $\alpha_{qp}^0$  backscattering coefficients can reduce significantly the range/elevation dependency which appears in the  $\beta_{qp}^0$  image, in particular for HV or VH, as shown in Figure 7-3 and Figure 7-4 and which is also well illustrated by Figure 7-5 and Figure 7-6 displaying the backscatter profiles along range transects.



Of particular importance is the use of  $\alpha_{qp}^0$  which can be justified by geometrical consideration. Indeed, if we consider that volume scattering dominates in the case of a relatively dense media like the tropical forests, the length of penetration (herein noted  $l_p$ ) turns out to be essential the normalization of the backscattering coefficient. This penetration length (often referred with the 3 dB threshold) can be defined more generally as the length beyond which the remaining scatterers do not contribute significantly to the backscattered energy. If we assume that  $l_p$  is constant in the considered range of incidence, the Figures 7-1 and 7-2 point out that the volume of scatterers which contribute to the main backscattered energy equals to  $l_p \cdot \cos(\theta_T) \cdot A_s / \sin(\theta_T)$  and thus depends on  $\theta_T$ . In order to take into account this variation, we come up with the backscattering coefficient  $\alpha^0$  which uses this volume as a normalization factor.

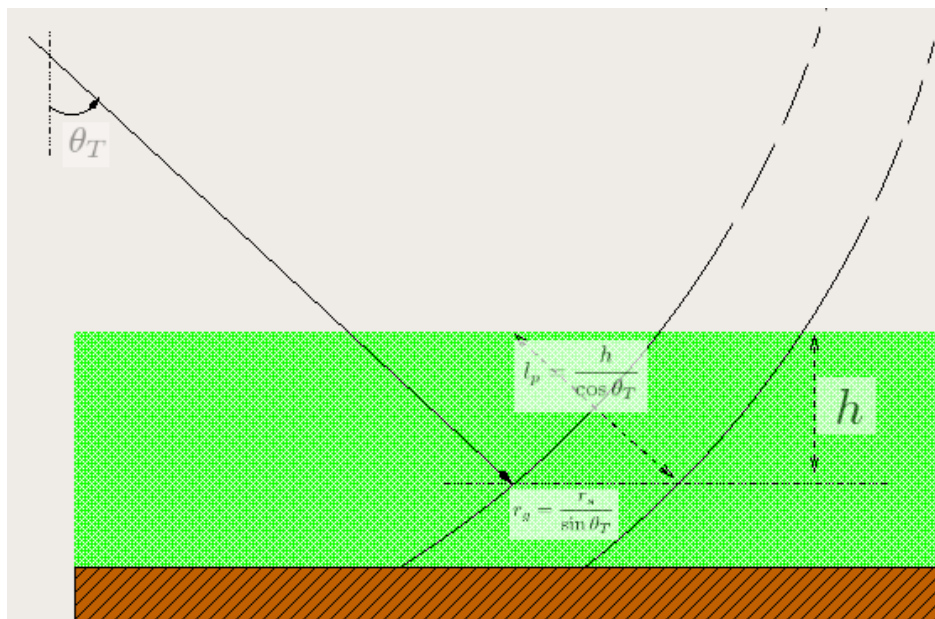


Figure 7-1: Geometry of the backscattering from a forest canopy. The figure explains the volume normalization used in the definition of  $\alpha^0$  (Equation 7.8).

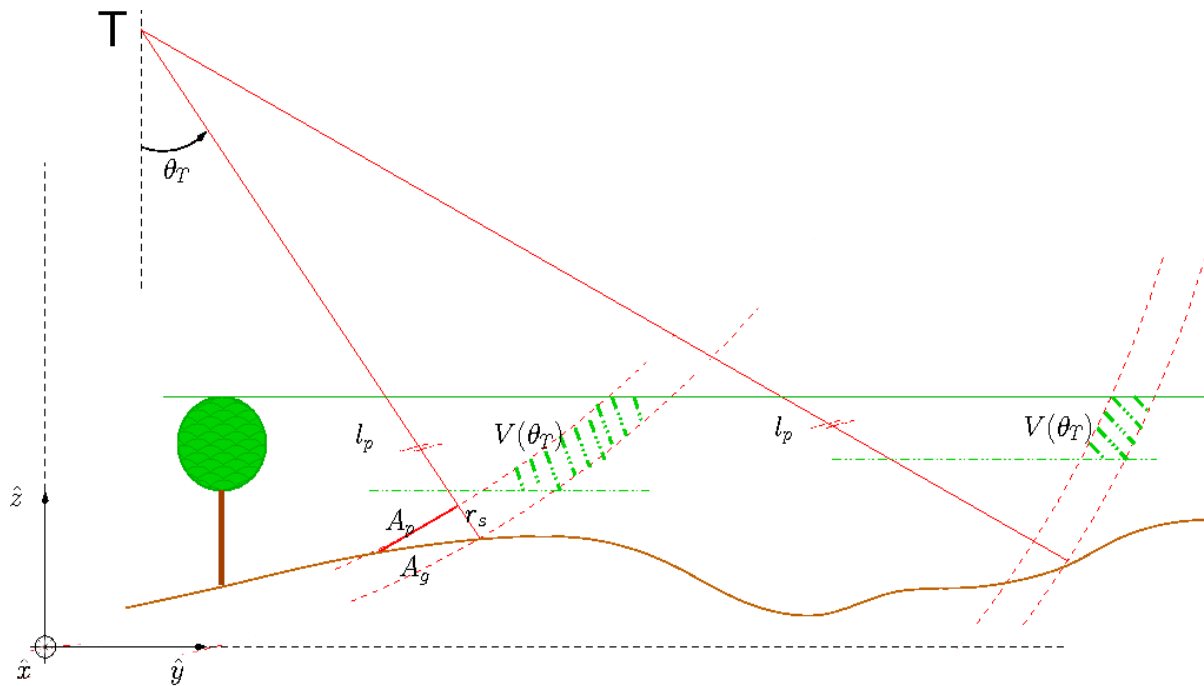


Figure 7-2: Illustration of the dependency of the scattering volume on the elevation angle defined. The use of this volume as a normalization factor leads to the definition of the backscattering coefficient  $\alpha^\circ$ .

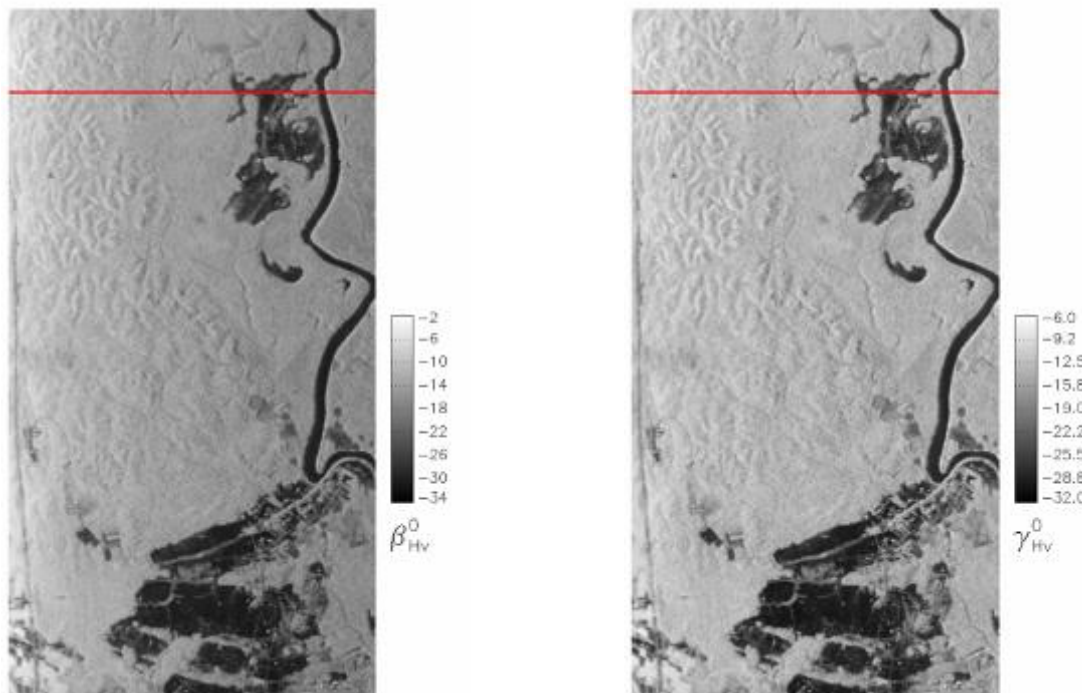


Figure 7-3:  $\beta^0$  and  $\gamma^0$  images of the Paracou region, corresponding to the "tropi0007\_Pcons\_Hv\_slc" files. Red line: across range transect where backscatter profiles are analyzed in Figure 7-5.



CS2

February 2011 V2.1

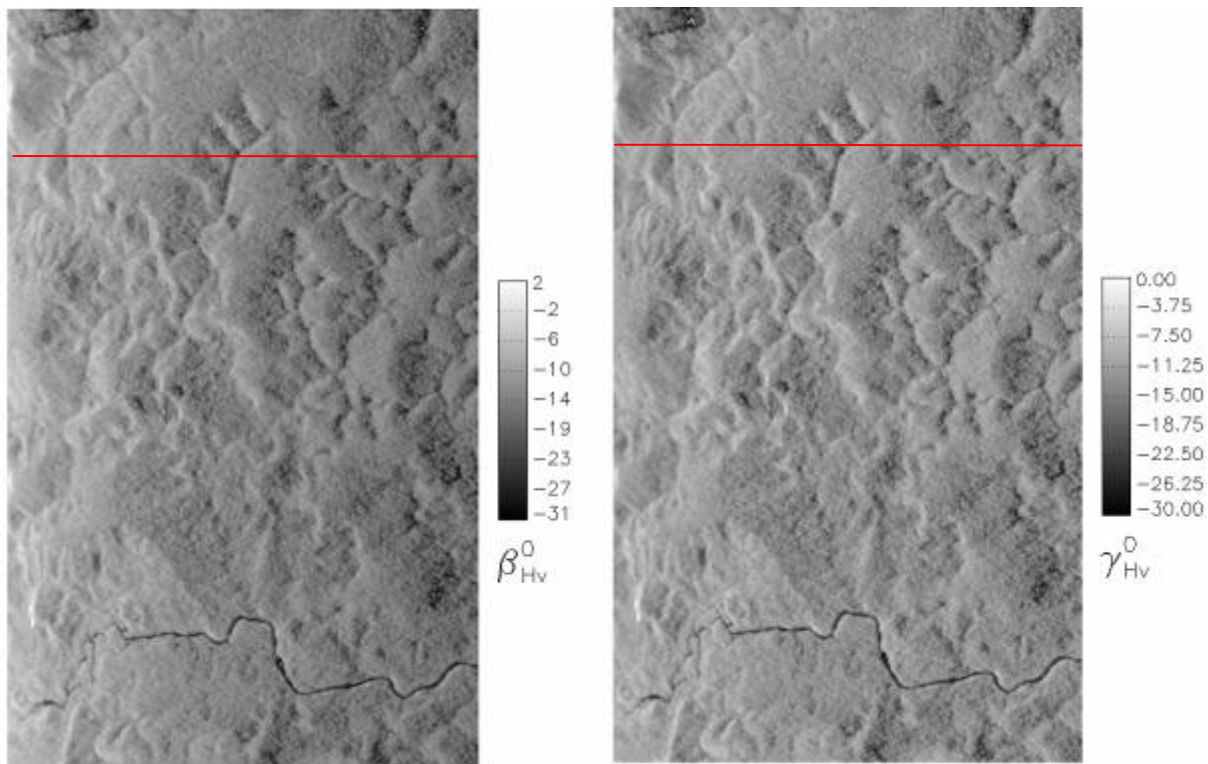
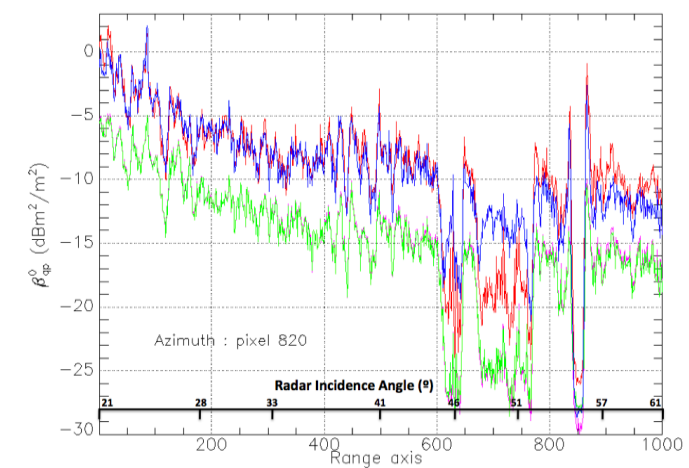


Figure 7-4:  $\beta^0$  and  $\gamma^0$  images of the region of Nouragues, corresponding to the "tropi0101\_Pcons\_Hv\_slc" files.  
Red line: across range transect where backscatter profiles are analyzed in Figure 7-6.





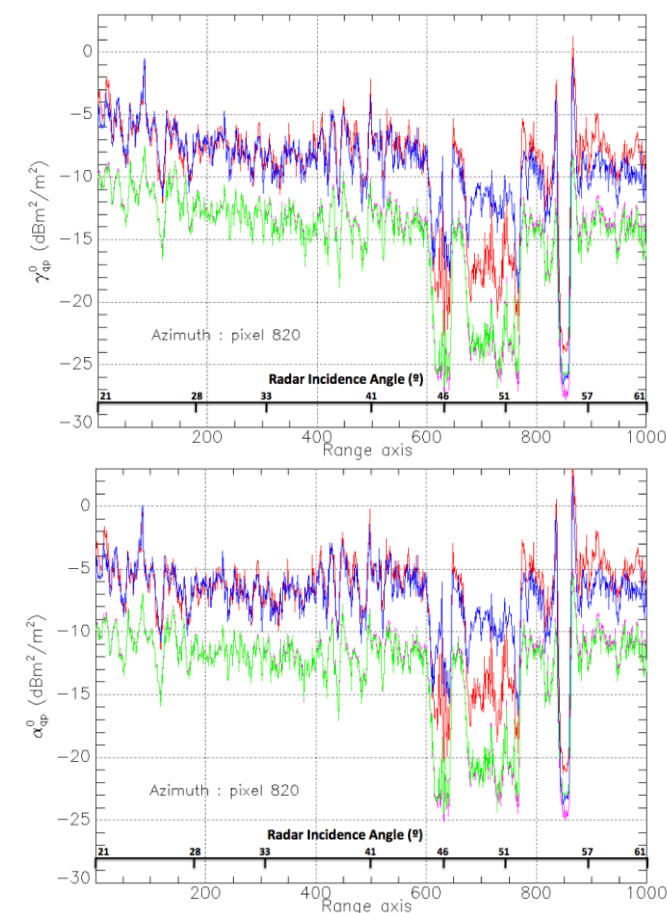
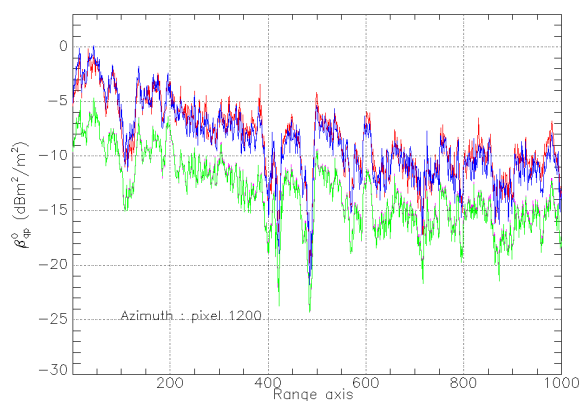


Figure 7-5: Range profiles of backscattering coefficient  $\beta$ ,  $\gamma$  and  $\alpha$  from a transect in Figure 7-3 on the image from "tropi0007\_Pcons\_gp\_slc" over Paracou. HH, VV and HV are respectively in red, blue and green colour. The coefficients are computed using spatial averaging over windows of 60 x 4 pixels respectively in azimuth and range. The profile size is reduced from 4000 to 1000 (x axis).



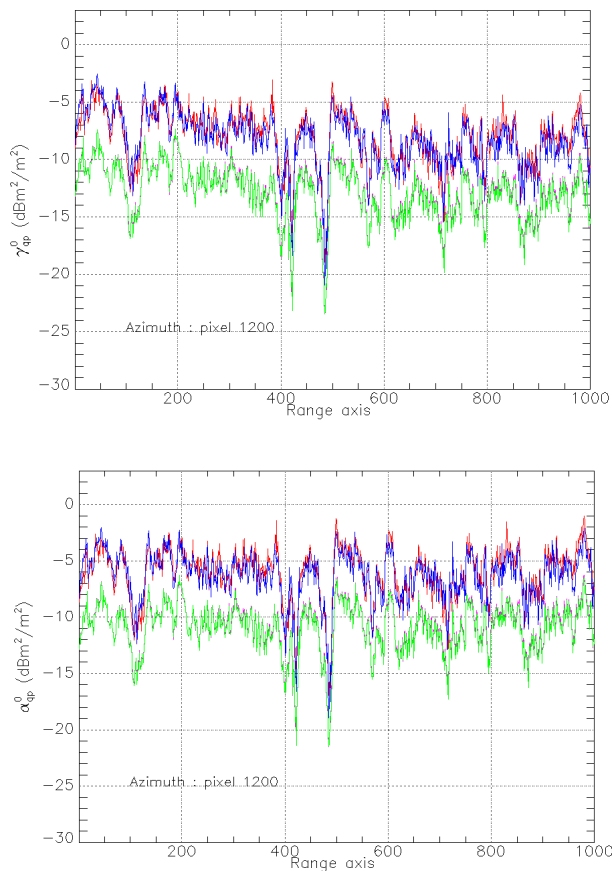


Figure 7-6: Range profiles of backscattering coefficients  $\beta^0$ ,  $\gamma^0$  and  $\alpha^0$  from a transect in Figure 7-4 on the image from "tropi0007\_Pcons\_gp\_slc" over Nouragues. HH, VV and HV are respectively in red, blue and green colour. The coefficients are computed using spatial averaging over windows of  $60 \times 4$  pixels respectively in azimuth and range. The profile size is reduced from 4000 to 1000 (x axis).

The following remarks can be drawn from examination of the Figures 7-5 and 7-6:

- polarization: in general, HH, VV and HV show very similar spatial variations over the forests. This can be seen over the whole transect in Nouragues and the forested part in Paracou. Whereas large polarization differences can be seen in non forested areas (bare soil, water), in Paracou. For forests, HH and VV are very close, and HV is approximately of 5 dB lower than HH and VV.
- Variation as a function of range:  $\beta^0$  variation across the range (from  $23^\circ$  to  $60^\circ$  of elevation angle) is important, about 10 dB for HH, VV and HV. However, the most important decrease is in the low range of elevation angle (about  $23$ - $35^\circ$ ).  $\gamma^0$  decrease with elevation angle is much reduced (of the order of 5 dB), and the reduction is significant with  $\alpha^0$ , for the forested areas.



The results suggest that for these forests, the angular normalization  $\gamma^0$  (Equation 7.7) can be improved using the  $\alpha^0$  normalization (Equation 7.8).

## 7.2. Analysis of the backscattering coefficients of the reference plots

The backscatter coefficients  $\beta_{qp}^0, \sigma_{qp}^0, \gamma_{qp}^0, \alpha_{qp}^0$  are extracted from all the pixels of the forest reference plots mentioned in section 6. For each stand, geographic coordinates (WGS84 UTM 22 latitude and longitude) have been converted in radar coordinates (image position i,j) by means of the transformation grid delivered by ONERA. For all pixels whose centers are located within a stand, the mean values of  $\beta_{qp}^0, \sigma_{qp}^0, \gamma_{qp}^0$  are computed by averaging values of all pixels, first in power units, before being converted in decibel.

In the preliminary analysis, 15 plots of 250 m x 250 m and the ROI number 16 (500 m\*500 m) are analyzed in priority. For each reference plot (ROI) containing a large number of pixels (from 22000 to 35000 for the 15 main plots in Paracou), the effect of speckle in the mean backscatter value is negligible. However, it can be noted that the concept of sample plots in tropical forests differs from that in managed temperate or boreal forests, where sample plots are selected for their homogeneity in terms of species, age classes and ground conditions. The sample plots in French Guiana have been established for ecological studies of the forest variability and dynamics. Thus the mean values and the standard deviation in terms of biomass depend on the plot size, as explained in Section 6.

For the radar datasets in Paracou and Nouragues, the original plots of 1 ha in Nouragues and 6.25 ha in Paracou are analyzed and included in the Excel-document. Each sheet in the document corresponds to an acquisition date and each row details the relevant backscatter parameters of a given stand. Additionally, the stand identification number, the number of pixels per stand, an estimate of the stand biomass (derived from in-situ measurements), the estimated standard error of the biomass estimates, and averaged elevation angles are included in the tables. The following table gives a typical description of the data provided.

Stand ID	Pixel Number	Biomass (t/ha)	Elevation angle
01	35489	369,6	44,27
02	35675	346,4	44,42
03	32848	309	42,00
04	31570	284,7	38,22
05	28194	300,5	35,72
06	27963	431,9	33,02
07	31744	392,4	36,50
08	29987	257,5	36,62
09	29339	337,5	33,35
10	22984	307,5	30,45
11	26037	402,7	33,49
12	24228	304,3	30,76
13	34142	405,3	42,43
14	34530	407,7	39,42
15	28131	417,8	34,97
16	132722	406,1	41,63

Table 7-1: Stand identifier, number of stand pixels, stand biomass and elevation angles corresponding to the "tropi0007\_Pcons\_Xx\_slc" acquisition files.



Stand ID	$\beta_{HH}^o$	$\beta_{HV}^o$	$\beta_{Vh}^o$	$\beta_{VV}^o$	$\bar{\sigma}_{HH}^o$	$\bar{\sigma}_{HV}^o$	$\bar{\sigma}_{Vh}^o$	$\bar{\sigma}_{VV}^o$	$\bar{\gamma}_{HV}^o$
01	-8,81	-13,32	-13,19	-8,84	-10,36	-14,89	-14,76	-10,40	-13,44
02	-8,88	-13,46	-13,34	-8,82	-10,40	-15,00	-14,88	-10,36	-13,55
03	-7,79	-12,27	-12,23	-8,05	-9,58	-14,05	-14,01	-9,83	-12,77
04	-7,36	-12,06	-12,04	-7,47	-9,47	-14,15	-14,13	-9,56	-13,10
05	-6,14	-10,93	-10,82	-6,05	-8,45	-13,25	-13,14	-8,39	-12,34
06	-5,14	-9,95	-9,90	-5,03	-7,83	-12,64	-12,59	-7,74	-11,88
07	-6,87	-11,67	-11,57	-6,67	-9,14	-13,95	-13,85	-8,94	-13,00
08	-6,43	-11,32	-11,21	-6,51	-8,67	-13,52	-13,42	-8,72	-12,57
09	-6,32	-10,66	-10,58	-6,01	-8,92	-13,29	-13,21	-8,62	-12,52
10	-3,99	-8,86	-8,83	-4,11	-6,98	-11,85	-11,81	-7,10	-11,21
11	-5,05	-9,54	-9,44	-4,75	-7,67	-12,15	-12,05	-7,35	-11,36
12	-4,19	-9,05	-8,98	-4,20	-7,21	-12,05	-11,98	-7,20	-11,40
13	-7,52	-12,21	-12,14	-7,68	-9,24	-13,95	-13,87	-9,42	-12,63
14	-8,02	-12,24	-12,21	-7,74	-10,00	-14,23	-14,20	-9,76	-13,10
15	-6,01	-10,48	-10,35	-5,80	-8,60	-13,01	-12,88	-8,36	-12,14
16	-7,28	-12,34	-12,32	-7,53	-9,08	-14,13	-14,11	-9,32	-12,87

Table 7-2: Radar Backscatter coefficients derived from the "tropi0007\_Pcons\_Xx\_slc" acquisition files.

It would be interesting to add to the table the polarimetric features, such as the module and phase of the complex correlation between polarization (HH and VV). However, because of the large size and the heterogeneity of the sample plots, the mean values of the polarimetric measurements will not be meaningful as plot and biomass indicators.

### 7.2.1 Temporal and polarization variations of the backscatter

The backscatter coefficients of the reference plots have been analyzed for different polarizations and different acquisition dates.

**Erreur ! Source du renvoi introuvable.** Figure 7.7 a, b, c, and d show the temporal variation of  $\sigma_{HH}^o$ ,  $\sigma_{HV}^o$ ,  $\sigma_{VV}^o$  and  $\gamma_{HV}^o$  of the 16 reference plots in Paracou.

The general observations are the following:

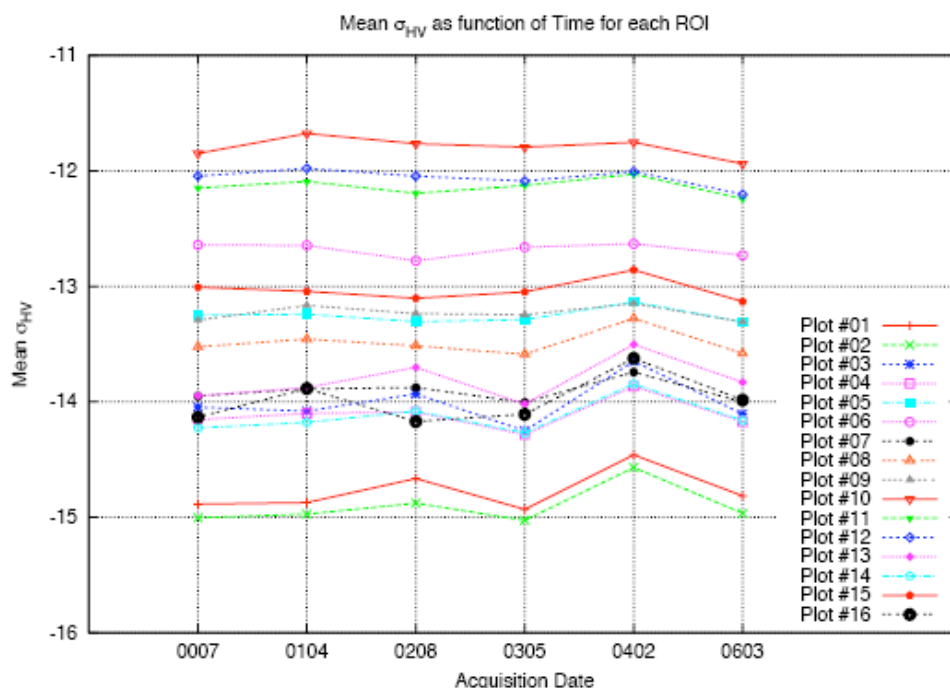
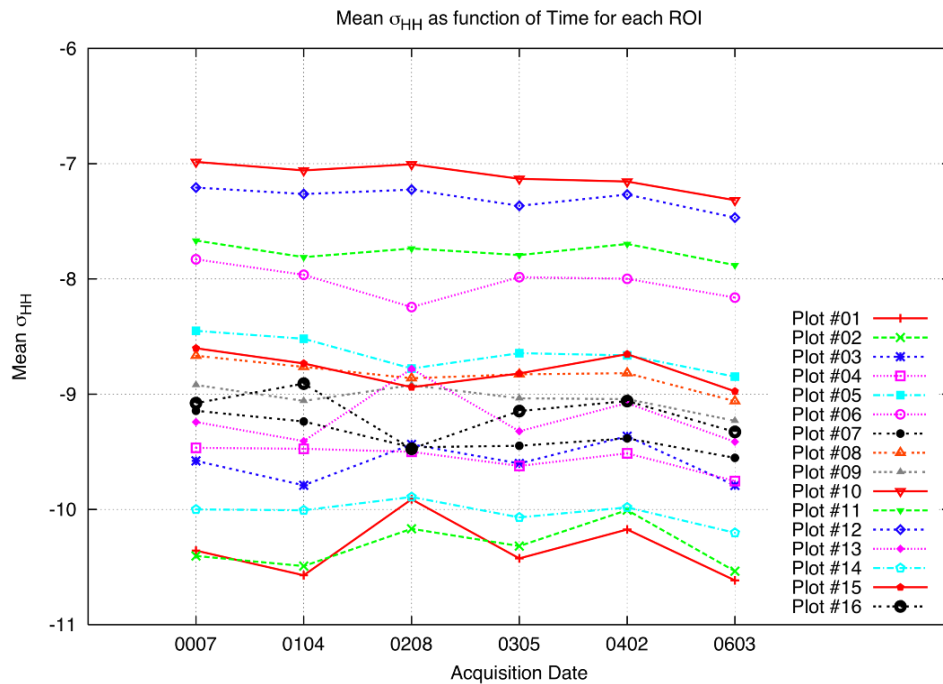
- The temporal variations of  $\sigma^o$  between the 6 different TropiSAR dates are less than 0.5 dB. The variations of stands located at near range (e.g. stands 10, 11, 12) are smaller than 0.3 dB, while higher variations can be observed for stands at far range (higher elevation angles) (between tropi0305 and tropi0402 for  $\sigma_{HV}^o$ , and between tropi0104 and tropi0208 for  $\sigma_{HH}^o$ ). Such a small temporal variation, of the order of the radiometric stability of the radar system, indicates that during the experimental period, both the system radiometric stability and the 'geophysical' stability of the forest plots. It can be noted that a slight decrease can be observed in temporal variation of  $\sigma_{HH}^o$ ;

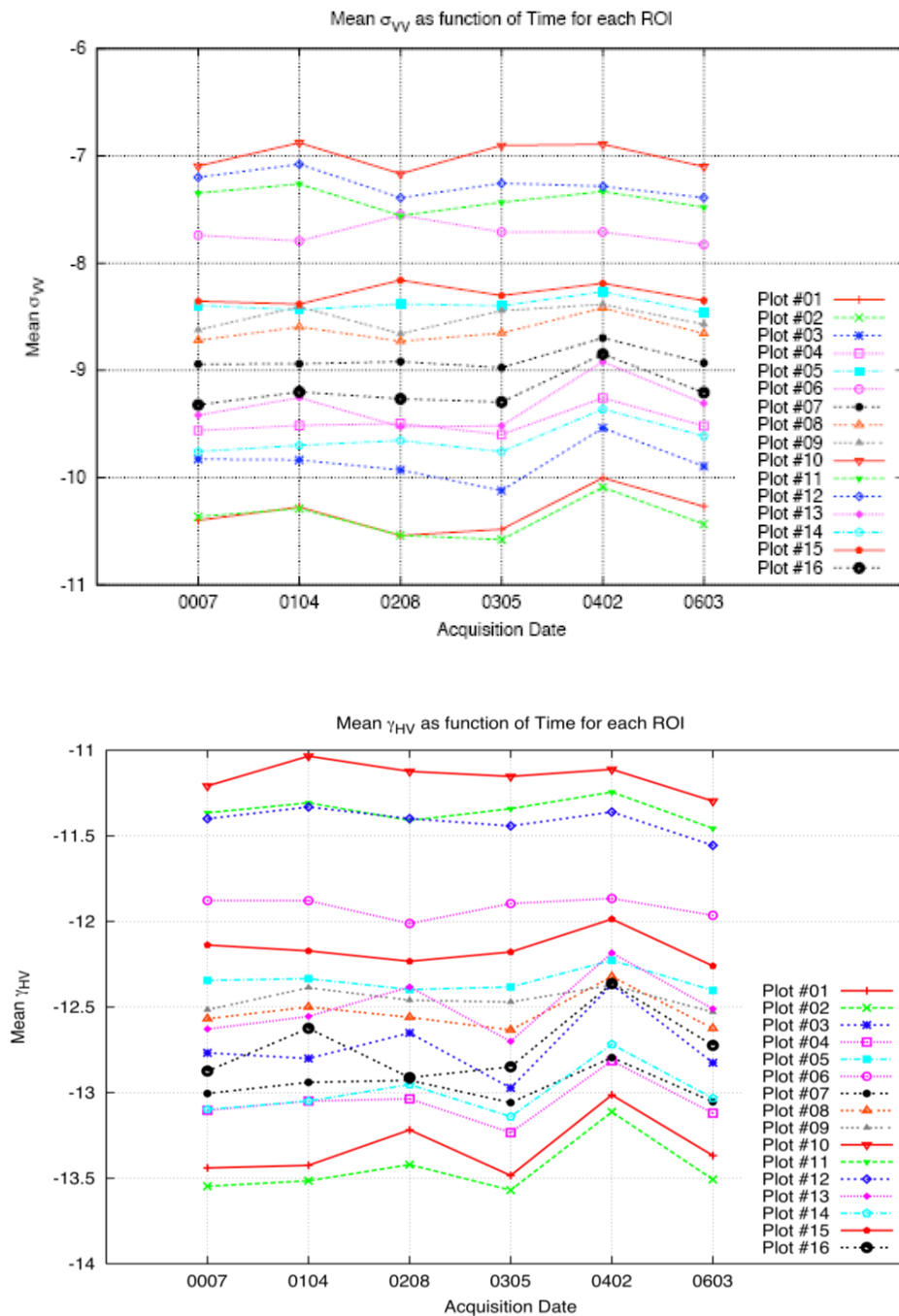




however, the decrease ( $< 0.3$  dB) is less than the nominal radiometric stability, and it is thus difficult to interpret this as due to system or geophysical variation.

- The overall dynamic range of the backscatter coefficients  $\sigma^0$  of the 3 polarizations, corresponding to the 16 reference plots is of the order of 3.5 dB, for the biomass range from 260 ton/ha to 430 ton/ha. Figure 7-7 d shows that when  $\gamma^0_{HV}$  is used to reduce the effect of incidence angle, the dynamic range is reduced to 2.5 dB.





**Erreur ! Source du renvoi introuvable.:** Temporal variations of  $\sigma_{HH}^0$ ,  $\sigma_{HV}^0$  and  $\sigma_{VV}^0$  and  $\gamma_{HV}^0$  corresponding to the 16 stands of the Paracou test site. Acquisition dates ranged between August 10th (tropi0007) and September 1st (tropi0603).

- The polarization behavior is illustrated in Figures 7-8. High correlation is observed between HH and VV, and between HH and HV. While HH and VV are very close (distributed along the 1/1 line), a distinction can be seen for stands with backscatter values  $> -9$  dB, (plots in near range and on slope), HH is lower



than VV. This can be interpreted by the reduction of double bounce scattering in HH. HH and HV are more correlated as shown in Figure 7-7b, in particular for the plots in near range (high HH).

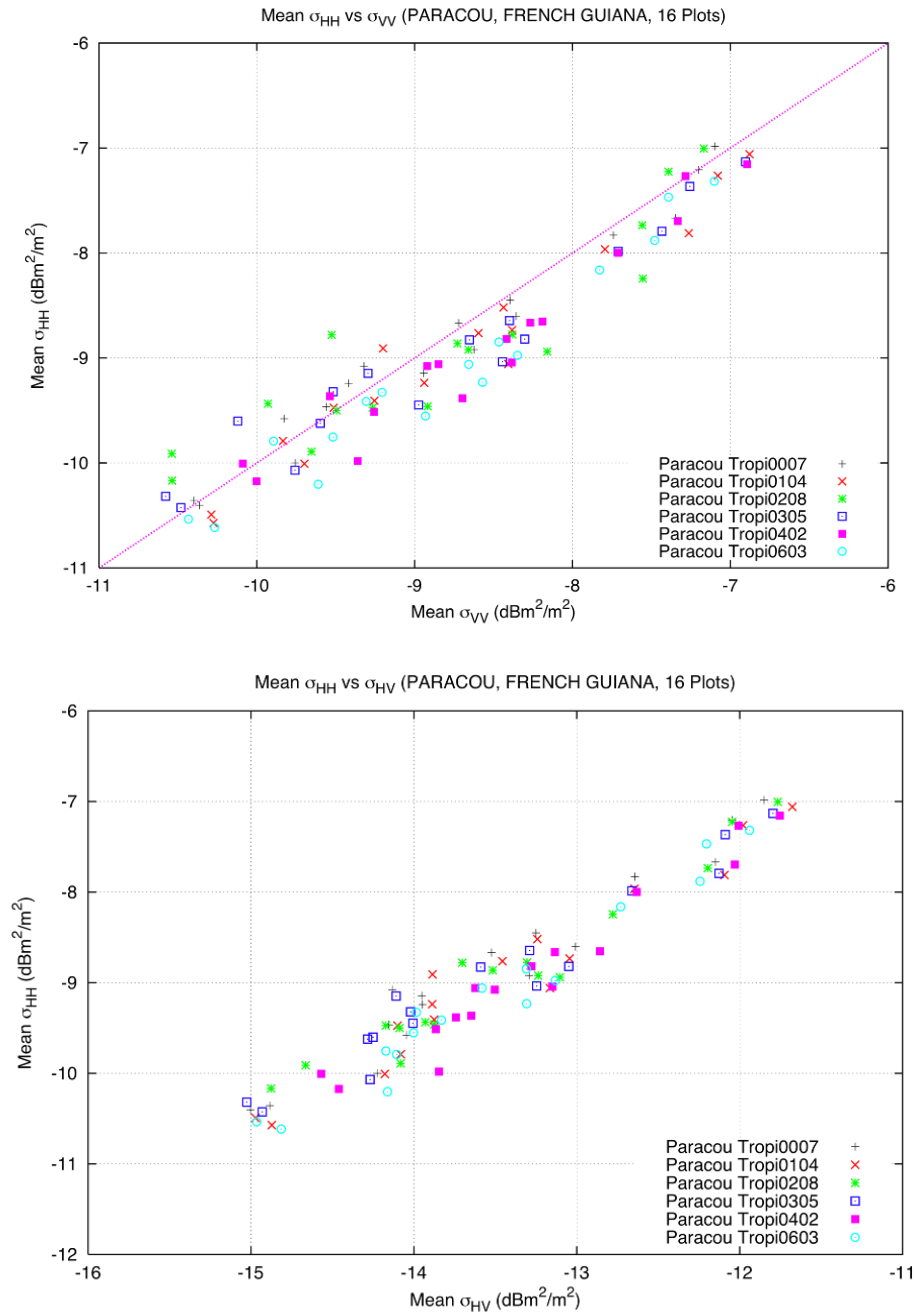


Figure 7-7: Radar backscattering coefficient expressed in  $\sigma_{HH}^0$  as function of  $\sigma_{VV}^0$  (top) and  $\sigma_{HV}^0$  (bottom) corresponding to the 16 stands of the Paracou test site, at different acquisition dates.



### 7.3. Relation with in-situ biomass

#### 7.3.1. Relation between the different backscattering coefficients and in situ biomass

The averaged normalized radar backscattering coefficients in HH, VV, and HV are derived for each forest plots at the test site of Paracou and for each acquisition dates.

Annex C shows the figures where  $\beta_{qp}^0$ ,  $\sigma_{qp}^0$ ,  $\gamma_{qp}^0$ ,  $\alpha_{qp}^0$  are plotted as a function of biomass for HH, VV and HV.

The distribution of  $\beta_{qp}^0$  as a function of biomass displays a high dispersion. As an example, the dynamic range of  $\beta_{qp}^0$  of different plots having a biomass value around 300 t/ha is of 5dB, for all polarizations.

When considering ground-projection normalization factor, resulting in the  $\sigma_{qp}^0$ , the dispersion previously mentioned is reduced, e.g. the dynamic range is of 3.5 dB for a biomass value set to 300 t/ha.

Using the incidence angle normalization leading to the  $\gamma_{qp}^0$ , the dispersion of the backscattering intensity is further reduced, presenting a dynamic range of around 3dB at the same biomass value, for all polarizations.

Finally, applying a volume normalization, resulting in  $\alpha_{qp}^0$ , the dispersion is further reduced, with a dynamic range less than 2dB. The  $\alpha_{qp}^0$  backscattering coefficient appears thus better than  $\gamma_{qp}^0$ , as far as the incidence effect on the relationships between biomass and the backscatter intensity is concerned.

#### *Application of $\alpha_{qp}^0$ or $\gamma_{qp}^0$ :*

To invert the a SAR scene with non forest areas and forests having a large range of biomass, the foreseen strategy is to compute  $\alpha_{qp}^0$  when scattering is dominated by volume effect (rather than surface) and  $\gamma_{qp}^0$  when the signal can reach the ground level.

Various indicators are under investigation to be computed prior to the backscattering normalization. Those can be based on analysis of Pol-InSAR, tomographic, and polarimetric data. However, a simple indicator based on the backscattering intensity ratio between HH and VV appears to be possible. For forest plots with biomass >260 t/ha, the ratio between  $\gamma_{HH}^0$  and  $\gamma_{VV}^0$  (or difference in dB) is small ( less than 1 dB in our analysis), whereas for non forest and low forest areas, the ratio is larger ( higher than 1 dB). When verified by the same analysis at other sites, a ratio threshold (e.g. 1 dB) can be used prior to the backscattering normalization.

#### 7.3.2. Topographic correction adapted to $\alpha^0$

After volume normalization, the remaining dispersion of  $\alpha_{Hv}^0$  as a function of biomass can be further explained by topographic effect. For biomass inversion, it is essential that this effect should be mitigated.

The topographic effect can produce important bias in the backscattered intensity, simply through geometrical configurations ('A<sub>g</sub>' in Figure 7-2 should be calculated with respect to the local incidence angles, [Van Zyl, 1993]), or more completely through electromagnetic considerations (especially regarding the coupling terms, [Villard, 2010]). The topography





correction proposed here lies on geometrical considerations, assuming that a) the top of the forest canopy follows the underlying surface and b) the azimuthal symmetry of the vegetation with respect to the vertical, whatever the ground topography. The second hypothesis brings us to consider the elevation angle ( $\theta_T$ ) for the Lambertian correction. Therefore, we come up with the following formula for the  $\alpha^0$  backscattering coefficient:

$$\alpha_{qp}^0(dB) = \beta_{qp}^0(dB) - 10 \log_{10} \left( \frac{\cos \theta_T \cdot \cos \theta_i}{\cos \psi_v} \right) \quad (7.9)$$

with :  $\psi_v = (\hat{n}, -\hat{k}_i)$

The calculation of the angles used in Equation 7.9 have been achieved with two different DEMs described in Section 2.3:

- a) The DEM from LiDAR measurements over the Paracou reference plots, covering an area of 2952 m x 4370 m, with ground resolution of 1 m. The LiDAR DEM is used in topographic correction of the different forest plots to assess the inversion method with minimized error on topographic effect.
- b) The DEM extracted from SRTM global data providing a ground resolution of 90 m to be used in the inversion of the SAR scene into biomass.

In order to reduce the large difference between the resolution of airborne SAR images and SRTM data, we worked at improving the resolution of the original 90m SRTM DEM to a finer resolution at 30m, which is also close to the spatial resolution expected for the BIOMASS mission. Previous studies related to DEM resolution improvement can be found in the literature. These are mostly based on variogram modeling and kriging [Carlos 2006, Marcio 2006]. More recently, [Keeratikasikorn, 2008] showed that for most cases using 90m SRTM DEMs as a source, the generation of 30m resolution DEMs of the same quality of the original 30m DEM can be achieved by means of bicubic polynomial interpolation technique. Based on the same assumptions, we rather considered a quintic polynomial interpolation using the Akima's 2D-interpolation method [Akima, 1978]. Such interpolation uses the triangulation method developed by [Lawson, 1972]. Classically, the objective of interpolation method is to transform (x,y) coordinates in the source image into (u,v) coordinates of the target image. The transformation mapping (x,y)  $\rightarrow$  (u,v) can be established by fitting parameters of given bivariate polynomials in the (u,v) plane, leading to transformation functions x(u,v) and y(u,v) which can be determined independently from each other [Wiemker, 1996]. According to the Akima's scheme, the transformation functions are substituted for a bivariate surface function z(u,v). In the SRTM DEMs, the surface height z is given at each (x,y) coordinates, and shall be interpolated elsewhere (in u-v plane). For that matter Akima's method first performs triangulation of the given heights in the (u-v) plane. The surface function z(u,v) can be represented as the sum of functions each valid in one triangle. Quintic bivariate polynomials in u, v are then fitted within all triangles, and the coefficients of these local polynomials are chosen such that the first and second partial derivatives of the surface function are continuous across the sides of the triangles.

Figure 7-9 a shows the initial 90m SRTM DEM covering the Paracou test site, while Figure 7-9 b displays the interpolated SRTM DEM at 30m resolution by means of the Akima's



interpolation algorithm. It was found that the resampled surface appears continuous and smooth, without erroneous oscillations. Large scale flat regions (especially dark ones) also appear well resolved in the target image since the Akima's method offers the best interpolation for regions related by affine, bilinear, or second degree polynomial functions between source and target images. Finally, as shown in Figure 7-9, the Akima's method provides highly confident resampled structures (even at edge values) accurately reproducing local vertical variations, additionally to computational stability and convergence.

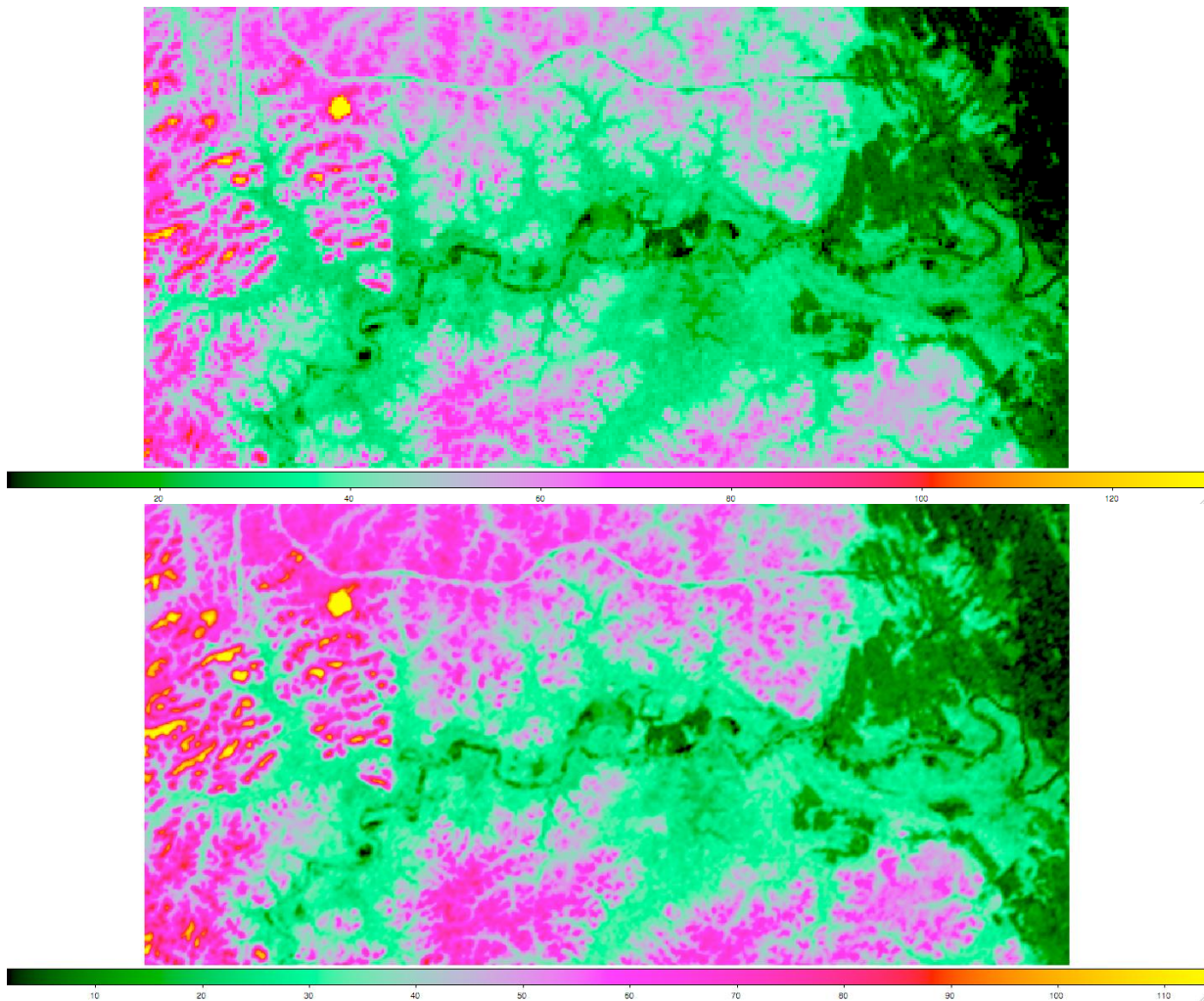


Figure 7-8: a (top) 90m SRTM DEM over the Paracou test site, and b (bottom), interpolated SRTM DEM at 30m resolution (color scale for the elevation is between 0 and 125 m).

Both types of DEM have been used for topographic correction. From the DEM grid, triangular facets have been determined in order to associate to each point of the grid a normal vector matching the mean between the two normal vectors to the two facets formed by the 8 neighbour points. Then, considering the radar slc images and their geo-localization, each image pixel (j,i) can be matched to geo-projected coordinates and then to the obtained normal vector. The geo-localization of the slc image has been achieved from the grid files 'tropi[xxxx]\_Pcons\_slc.grille' using the UTM22 coordinate system and the RGFG95 geo-projection (equivalent over French Guiana to a projection on the WGS84 ellipsoid). Once



loaded the file with the normal vector for each radar image pixel, the local incidence file ( $\theta_i$ ) can be derived as well as the file for  $\psi_v$ , used to derive the tilted surface intercepted by the resolution cell.

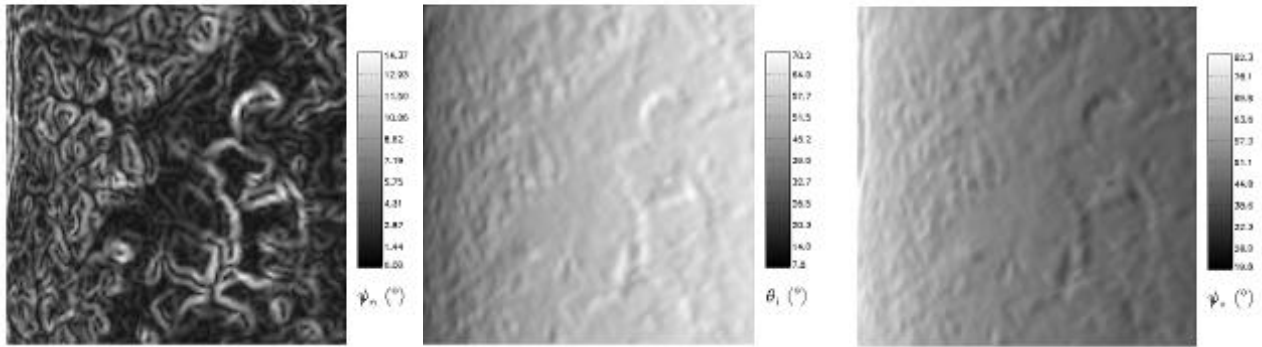


Figure 7-9: Angle images derived from the SRTM DEM and used in the topographic correction. From left to right, angle with the vertical, local incidence angle and angle ' $\psi_v$ ' defined above.

After topographic correction, the backscattering coefficient  $\alpha_{pq}^0$  are analyzed as a function of in-situ biomass of the reference forest plots. As stated in the previous sections, there is a strong correlation between the 3 polarizations HH, VV and HV over dense forest plots. Similar sensitivity to biomass is thus expected from  $\alpha_{HH}^0$ ,  $\alpha_{VV}^0$  and  $\alpha_{HV}^0$ . However, for the less dense forest areas in the scene, as in the case of boreal or temperate forests with lower biomass density, the relative contribution of ground and canopy scattering in the backscatter intensity changes with the polarization. For such general cases, HV was proved in previous studies to result dominantly from canopy scattering, e.g. to be less affected by the ground contribution.

Figure 7-11 shows  $\alpha_{HV}^0$  versus in situ biomass of 15 reference forest plots of 250 m x 250 m of high biomass (260-440 ton/ha) at the Paracou test site at one date (August 10<sup>th</sup>). In this test, the topographic correction is based on the LiDAR DEM which covers only the region of the reference plots.

Similar results are obtained with all the 6 dates, and also with HH and VV.

In Figure 7-11, the  $\alpha_{HV}^0$  data of the six dates from Paracou are put together with existing data sets covering the range of biomass from 0 to 300 ton/ha. Those data are HV backscattering coefficients, expressed in  $\gamma^0$  from the Landes forests [Le Toan, 1992], Remningstorp forest [Sandberg, 2010] and La Selva forest [Saatchi, 2010]. In Figures 7-10 and 7-11, a curve relating HV to biomass derived from multiple datasets [Le Toan, 2010] is also added.

The solid curve in Figures 7-10 and 7-11 is a regression curve of form

$$\gamma_{HV}^0 = a_0 + a_1 \log_{10} B$$

with  $\gamma_{HV}^0$  expressed in dB.

$$\gamma_{HV}^0 = 7.868 \log_{10} B - 29.91 + K$$



where  $B$  is the above ground biomass in  $\text{t ha}^{-1}$ ,  $k$  is a calibration factor in dB

The following remarks can be made:

- In Figure 7-10, the data shows an increasing trend, but the overall dynamic range from 260 ton/ha to 440 ton/ha is small (of the order of 1.5 dB).  
It is to be noted that the nominal radiometric stability is  $\pm 0.5$  dB and the uncertainty in biomass for plots of 6.25 ha in the dense tropical forest is of the order of 5% (cf. Section 6).
- In Figure 7-11 the data from Paracou, expressed in  $\alpha_{\text{HV}}^0$ , appear to fit well to the general trend depicted by the multi-site regression.
- In order to assess statistically the fit between the general curve and the data from Paracou, the following parameters are used: the Root Mean Squared Difference, the Mean Percentage Error (bias), the Pearson and Spearman coefficients as described in Table 7-3. For the 14 data in Figure 7-10, the level of significance of the Spearman coefficients at 90% and 95% of confident interval are respectively 0.456 and 0.544.

In addition, the mean percentage error ( bias) is found to be very small.

The results show that the data from Paracou can be expressed by the same relationship between  $\gamma_{\text{HV}}^0$  and biomass established from multiple datasets, with in certain cases, a calibration constant to take into account the differences in SAR systems (center frequency, calibration, processing...). For Paracou data, no calibration constant is applied. This means that the relationship can be applied to a diversity of forests, with biomass well over 300 t/ha.

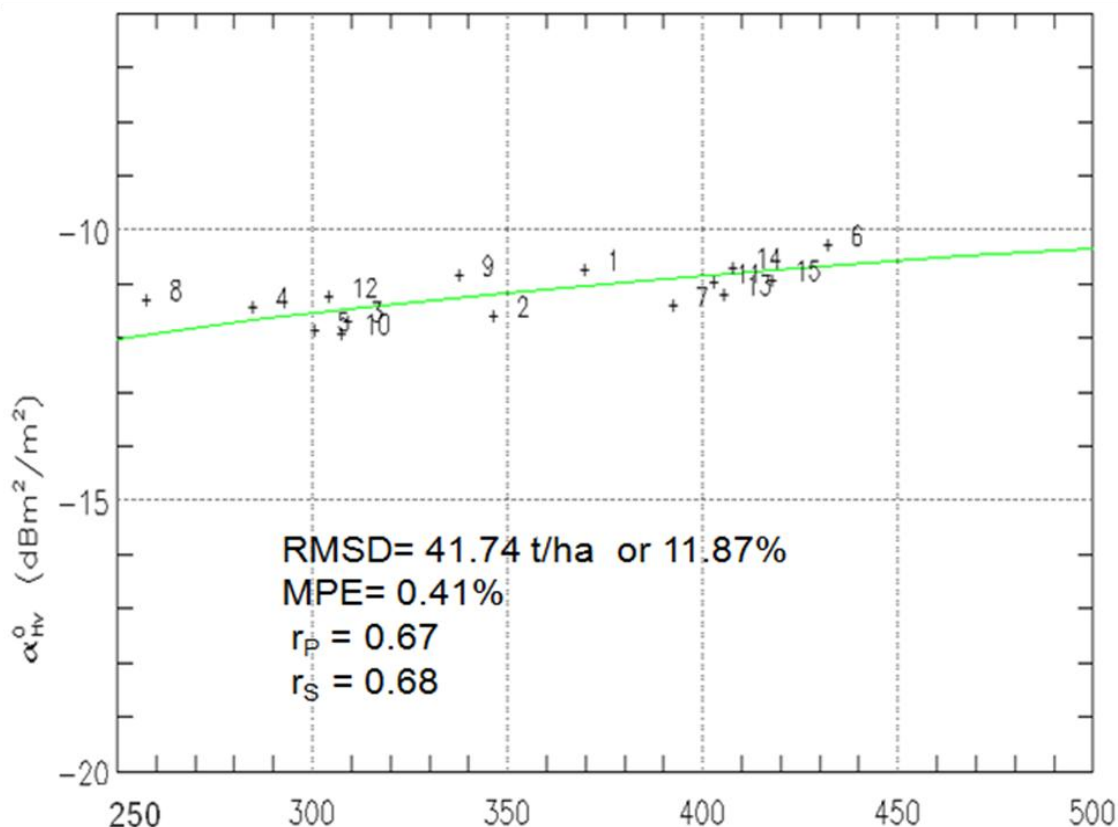






Figure 7-10: The HV backscattering coefficients, expressed in  $\alpha^0$ , as a function of biomass for the 15 reference plots of 250 m x 250 m in the Paracou site. For each data point, the number denotes the number of the plot. The curve is the relationship between  $\gamma_{HV}^0$  and biomass established from multiple datasets [Le Toan et al., 2010]. RMSD = Root Mean Squared Difference, MPE= Mean percentage error,  $r_P$  and  $r_S$  are Pearson and Spearman coefficients.

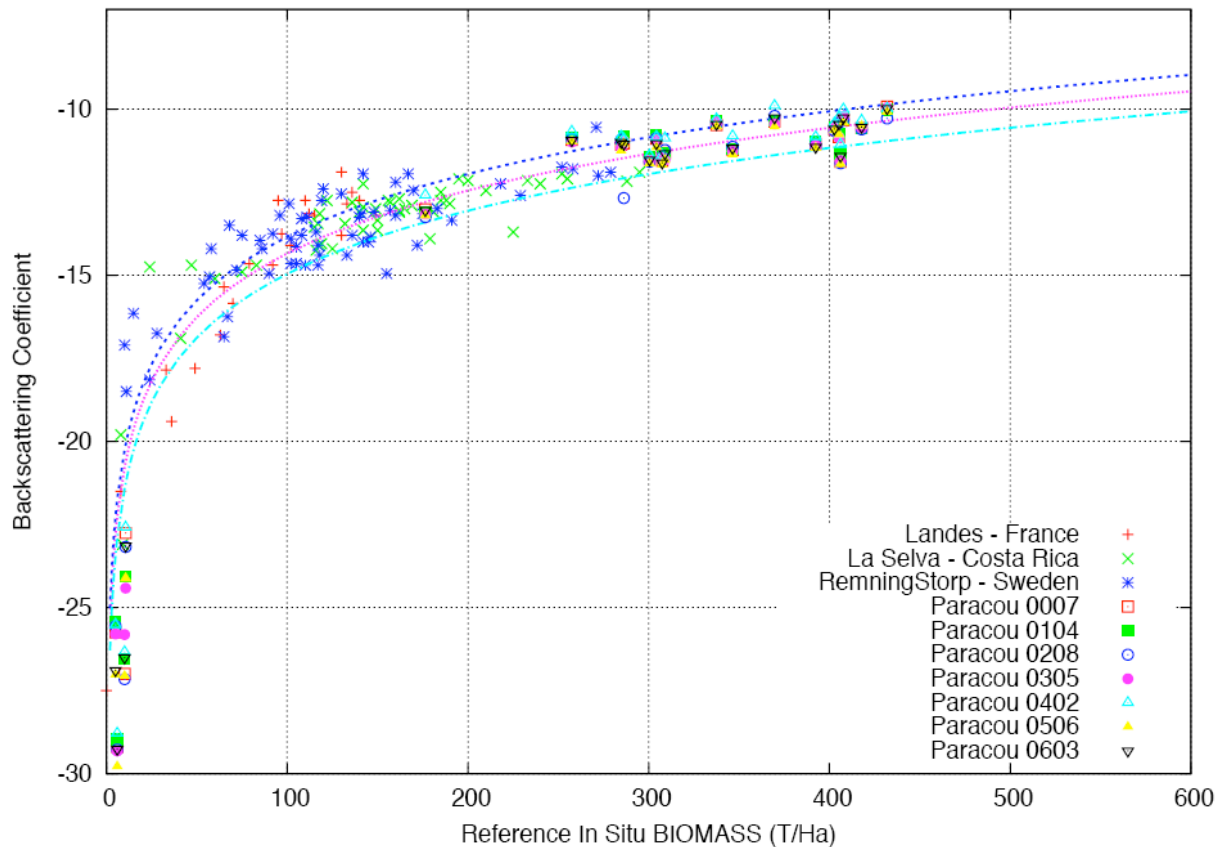


Figure 7-11: HV backscattering coefficients, expressed in  $\gamma^0$  from the Landes forests [Le Toan et al., 1992], Remningstorp forest [Sandberg et al., 2010] and La Selva forest [Saatchi et al., 2010] and expressed in  $\alpha^0$  at the Paracou test site. The pink curve is the relationship between  $\gamma_{HV}^0$  and biomass established from multiple datasets [Le Toan et al., 2010]. The dashed blue curves materialize 20% of error in biomass.



Root Mean Squared Difference :	$RMSD = \sqrt{\frac{1}{N} \sum_k (\hat{B}_k - \check{B}_k)^2}$
Mean Percent Error :	$MPE = \frac{1}{N} \cdot \sum_k \frac{(\hat{B}_k - \check{B}_k)}{\check{B}_k}$
Pearson (linear) correlation coefficient :	$r_P = \frac{\sigma_{\hat{B}\check{B}}}{\sigma_{\hat{B}}\sigma_{\check{B}}}$
Coefficient of determination :	$r_P^2$
Spearman (rank) correlation coefficient :	$r_S = 1 - \frac{6 \sum_k d_k^2}{n(n^2 - 1)}$

Table 7-3: Statistical parameters assessing of the correlation between estimated biomass and the reference biomass.

## 7.4. Preliminary biomass inversion mapping

### 7.4.1. Inversion of $\alpha_{HV}^0$

In order to transform the SAR scene from Paracou into biomass map, we applied the topographic correction using the interpolated SRTM DEM at 30 m of resolution. Mean  $\alpha_{HV}^0$  of window of respectively 15 x15 pixels and 25 x 25 pixels are inverted into biomass values according to equations :

$$\log_{10} B = \begin{cases} -\ln\left(\frac{-\alpha_{HV}^0 - 10}{32}\right) & \text{if } \alpha_{HV}^0 < -15 dBm^2/m^2 \\ 4.5563 + 0.18 \alpha_{HV}^0 & \text{if } \alpha_{HV}^0 \geq -15 dBm^2/m^2 \end{cases}$$

Figure 7-14 a, b show the resulting biomass maps and Figure 7-13 shows the comparison between retrieved biomass and the in situ biomass at the reference plots.

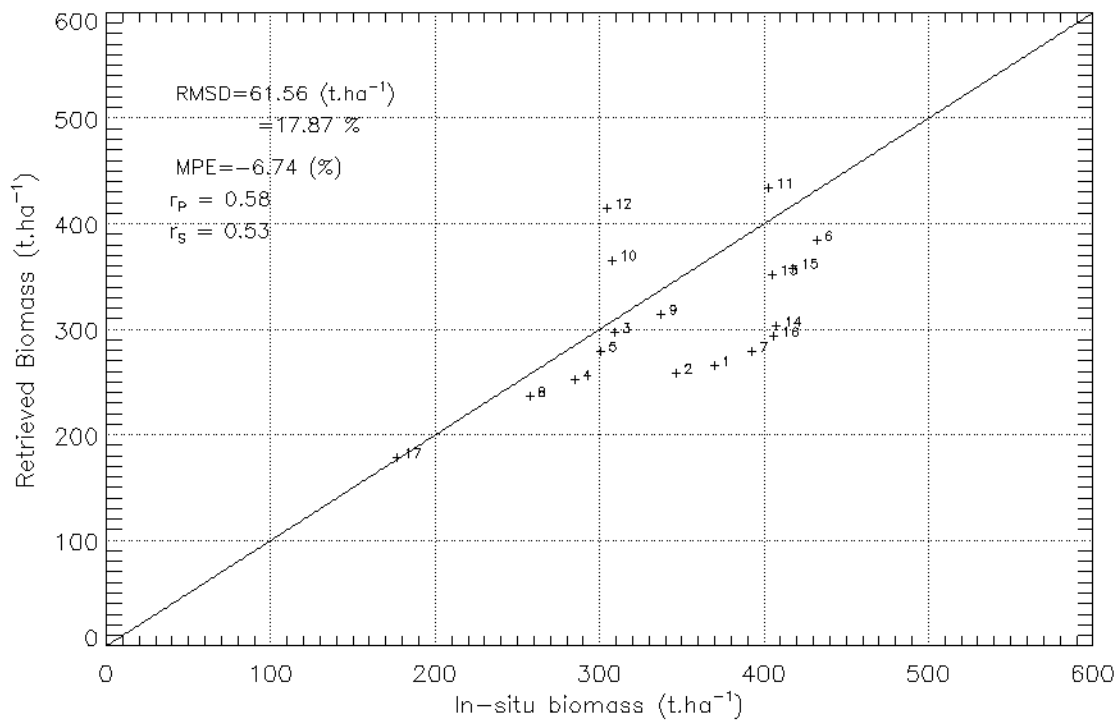
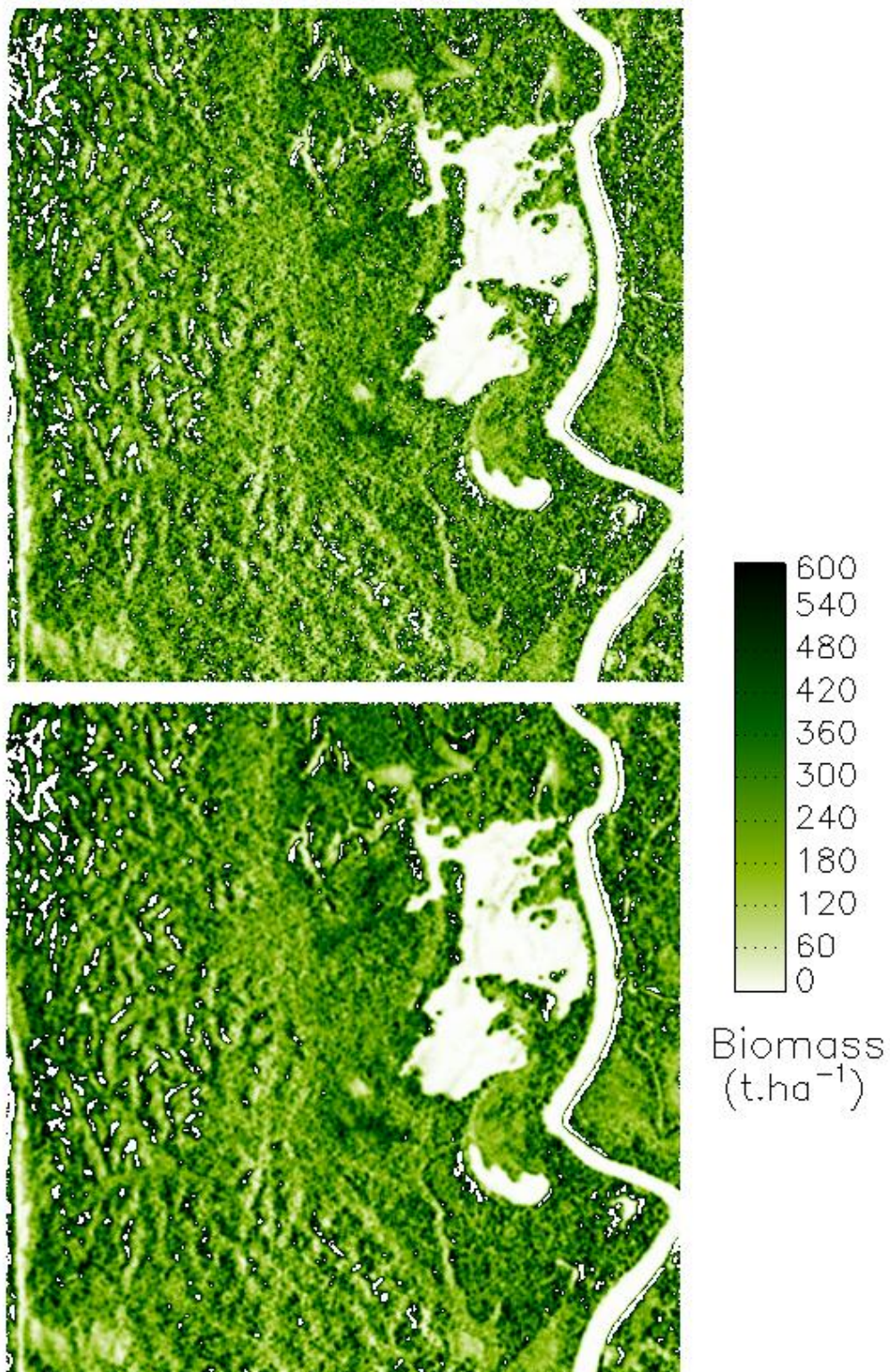


Figure 7-12: Retrieved biomass versus in situ biomass of the plots in Paracou, from inversion of  $\alpha_{HV}^0$  using the topographic correction derived from SRTM DEM.





Figure 7-13: Biomass map of the Paracou site, obtained by inversion of  $\alpha_{HV}^0$  (corrected with the SRTM DEM)



using a window of 15 x 15 pixels at the top (a) and 25 x 25 pixels below (b). White values are either non estimated (masked with the 600 t/ha threshold) or zero biomass regions.

The following remarks can be made:





The statistical assessment of the retrieval based on interpolated SRTM at 30 m resolution, in Figure 7-14 is good (RMSD= 17.87%, as compared to the result using LiDAR height in Figure 7-10, but with lower correlation coefficient). However, residual topographic effect is visible, as shown in the Figure 7.13, where plots 10, 12 have slope facing the radar are overestimated, whereas plots 1, 2 with slope away from the radar appear underestimated.

The biomass maps also show some residual topographic effect, however, this is to be interpreted together with the knowledge on the spatial distribution of biomass as a function of slope in this region [Ferry, 2010].

#### 7.4.2 Inversion using intensity and Pol-InSAR

In order to improve the retrieval performance base on SAR intensity ( $\alpha_{HV}^0$  in the previous section), other SAR measurements have been explored

The basis for this approach is provided by Bayes theorem which relates the likelihood function  $P(D_{meas} | B)$  to the posterior distribution  $P(B | D_{meas})$  through:

$$P(B | D_{meas}) = \frac{P(D_{meas} | B)P(B)}{P(D_{meas})} \quad (5.1)$$

Where  $B$  is the biomass and  $D_{meas}$  is radar measurement

$P(B | D_{meas})$  and  $P(D_{meas} | B)$  represent the conditional probabilities, for example  $P(B | D_{meas})$  is the probability of biomass  $B$ , given the measured data  $D_{meas}$ .

$P(B)$  is the a priori probability, based on initial knowledge of the biomass distribution in the scene.

The integral of  $P(B | D_{meas})$  over all possible values of biomass in the scene equals 1:

$$\int_B P(B | D_{meas}) dB = 1$$

Since  $P(D_{meas})$  is independent of  $B$ ,

$$P(D_{meas}) = \int_B P(D_{meas} | B)P(B)dB$$

The inversion method supposes a relationship  $f$  between biomass and the radar measurement. Using the established models, we derive the radar value predicted for a given biomass  $B$ :



$$D_{theo} = f(B)$$

The differences between model derived  $D_{theo}$  and experimental values  $D_{meas}$  can be taken into account by introducing random variable  $R$  representing the sources of random noise not considered in the model  $D_{theo} = f(B)$ .

$$D_{meas} = R D_{theo}$$

The approach can be used to handle multiple sources of information (e.g. intensity and PolInSAR measurements), provided that they are related to biomass, and that they are independent (or partially independent from one another). In this case,

$$B_{estimMMSE} = K_1 K_2 \int_B \frac{P(R_1)P(R_2)}{|D_{1theo} D_{2theo}|}$$

The relationship between Pol-InSAR height and biomass is still under investigations. In this report, we explored other Pol-InSAR measurements that can be related to biomass. From our analysis, it was found that the size of the loci encompassing the Pol-InSAR coherences (the ellipse region on the complex unit circle) can be used, especially considering the gap between the highest and the lowest phases. For that purpose, 20% of the highest phases in HV have been extracted as well as 20% of the lowest phases for the HH-VV combination of polarizations (classically used to maximize the double bounce contribution supposed to be projected on the ground in double pass monostatic acquisition). This phase difference is then transposed to a phase center height, using the multiplicative factor  $h_a/2\pi$  where  $h_a$  matches the local ambiguity height. This procedure has been carried out for each ROI and we come up with an interesting linear relationship (cf. Figure 7.14) between this phase center difference (noted  $\Phi$ ) and the biomass:

$$\Phi = 0.078 * B - 2.1245$$

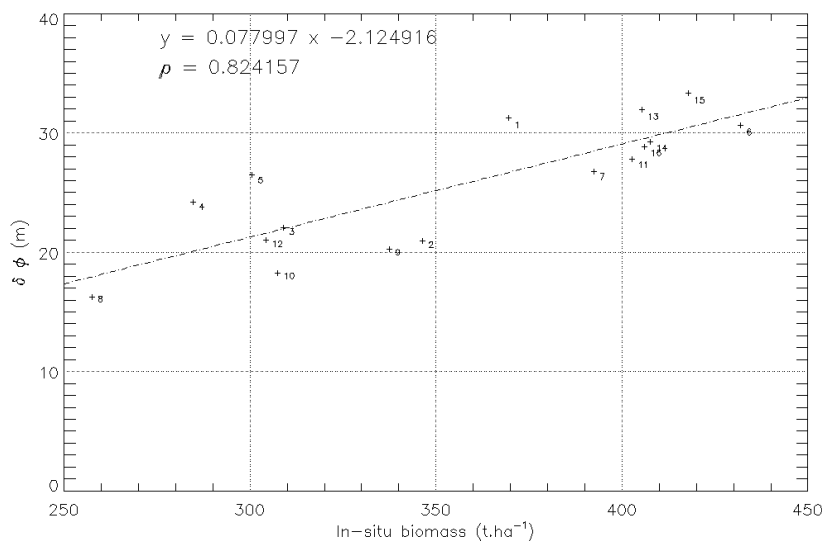


Figure 7-14: Relationship between the Pol-InSAR indicator  $\Phi$  and the in-situ biomass.



Figure 7-15 shows the comparison of the in situ biomass and the biomass retrieved based on Bayes inversion of  $\alpha^0_{HV}$  (corrected with SRTM DEM) and the Pol-InSAR indicator  $\Phi$ . Compared to the use of intensity only (based on SRTM topographic correction), the retrieval results are significantly improved, in terms of MRSD, MPE, and the correlation coefficients.

This encouraging result requires further studies on the use of multiple radar measurements in biomass inversion.

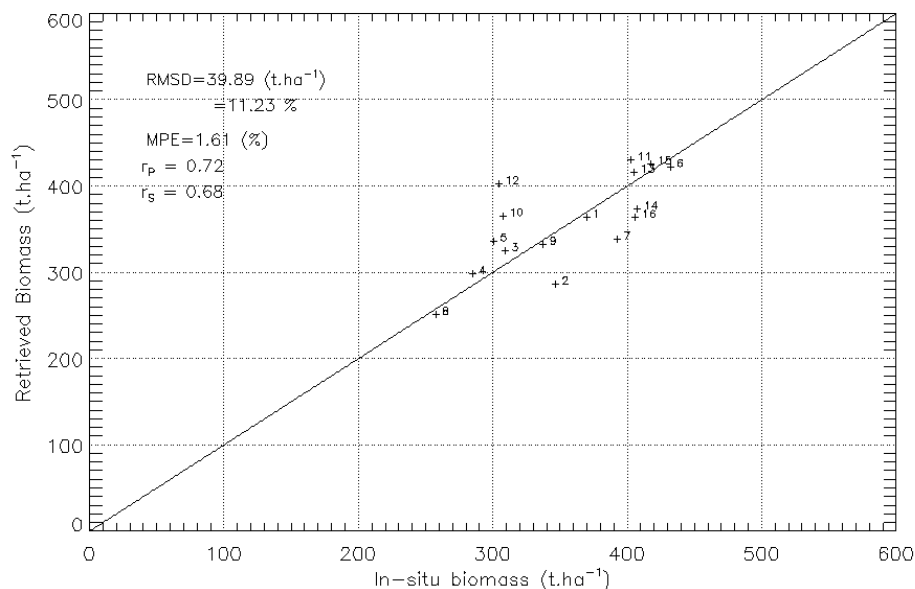


Figure 7-15: Comparison of the in situ biomass and the biomass retrieved based on Bayes inversion of  $\alpha^0_{HV}$  and the Pol-InSAR indicator  $\Phi$ .

## 7.5 Summary and current works

In this study, the TropiSAR backscatter coefficients have been analyzed in terms of polarimetric, temporal and incidence behavior. The preliminary analysis has highlighted the following:

- The high correlation between polarized backscatter coefficients, indicating that the tropical forests are characterized by specific scattering mechanisms
- The high temporal stability of the backscatter coefficients, during the campaign,
- The effect of elevation angle of these dense medium is better compensated by a new normalized coefficient  $\alpha^0$ , as compared to the classical  $\gamma^0$ .
- The topographic effect needs to be account for. In the absence of DEM whose resolution is compatible with the SAR data spatial resolution, interpolated SRTM DEM can be used to correct for the topography,
- The relationships between the backscattering coefficients  $\alpha^0_{HV}$  with in situ biomass are in good agreement with the trend derived from previous datasets.
- The preliminary inversion using HV backscattering coefficients has provided mapping results with RMSD of less than 20%.
- The combination of different SAR measurements derived from intensity and PolInSAR, e.g. using a Bayes inversion approach, was found to improve the inversion performance.



This work will be pursued on the other TropiSAR data (in particular Nouragues), and making use of tomographic datasets for an improved understanding of the various SAR , and Pol-InSAR measurements with biomass.





## 8. TROPISAR DATA ANALYSIS – POLINSAR ANALYSIS

### 8.1. Temporal decorrelation analysis

One of the objectives of the TropiSAR campaign was to assess whether the interferometric coherence would remain high despite the temporal baseline after a satellite cycle, around 22 days. In order to meet this objective, the same scene was imaged 7 times over the full period of the TropiSAR campaign.

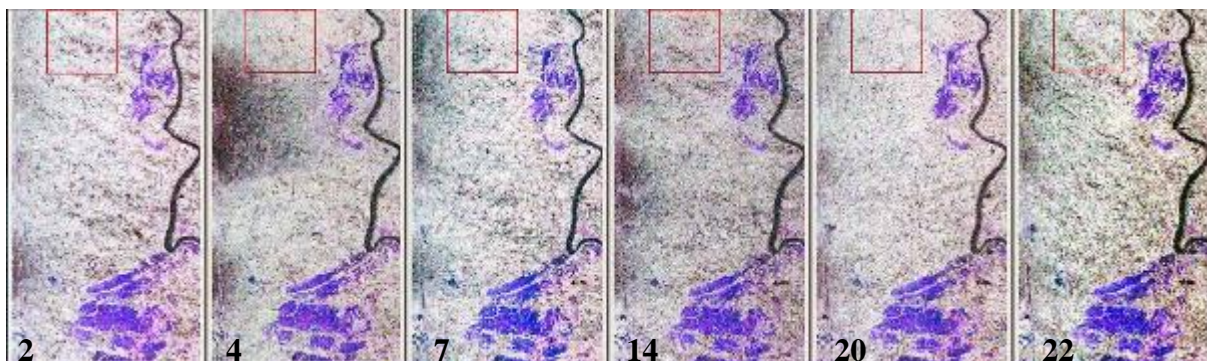


Figure 8-1: Interferometric coherence image for HH, HV and VV channels between tropi0007 and tropi0104, tropi0208, tropi0305, tropi0402, tropi0503, tropi0603, scaled between 0 and 1 for 6 time intervals (2 days, 4 days, 7 days, 14 days, 20 days, 22 days) The red box indicates the area which was explored in the histogram analysis.

The next figure represents the corresponding  $k_z$  variation using the same upper and lower bound and the same color table. As expected the darker area in the second coherence image can be correlated with a larger  $k_z$ , resulting in a loss of coherence linked to volume and spatial decorrelation.

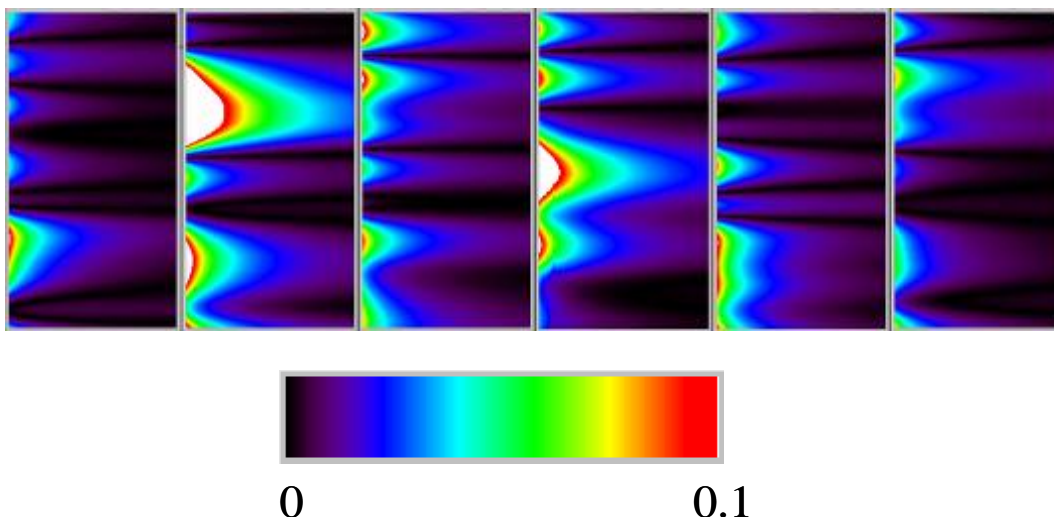


Figure 8-2: Image of the  $k_z$  or  $(2\pi/Ha)$  for the six interferometric images presented in Figure 8-1.

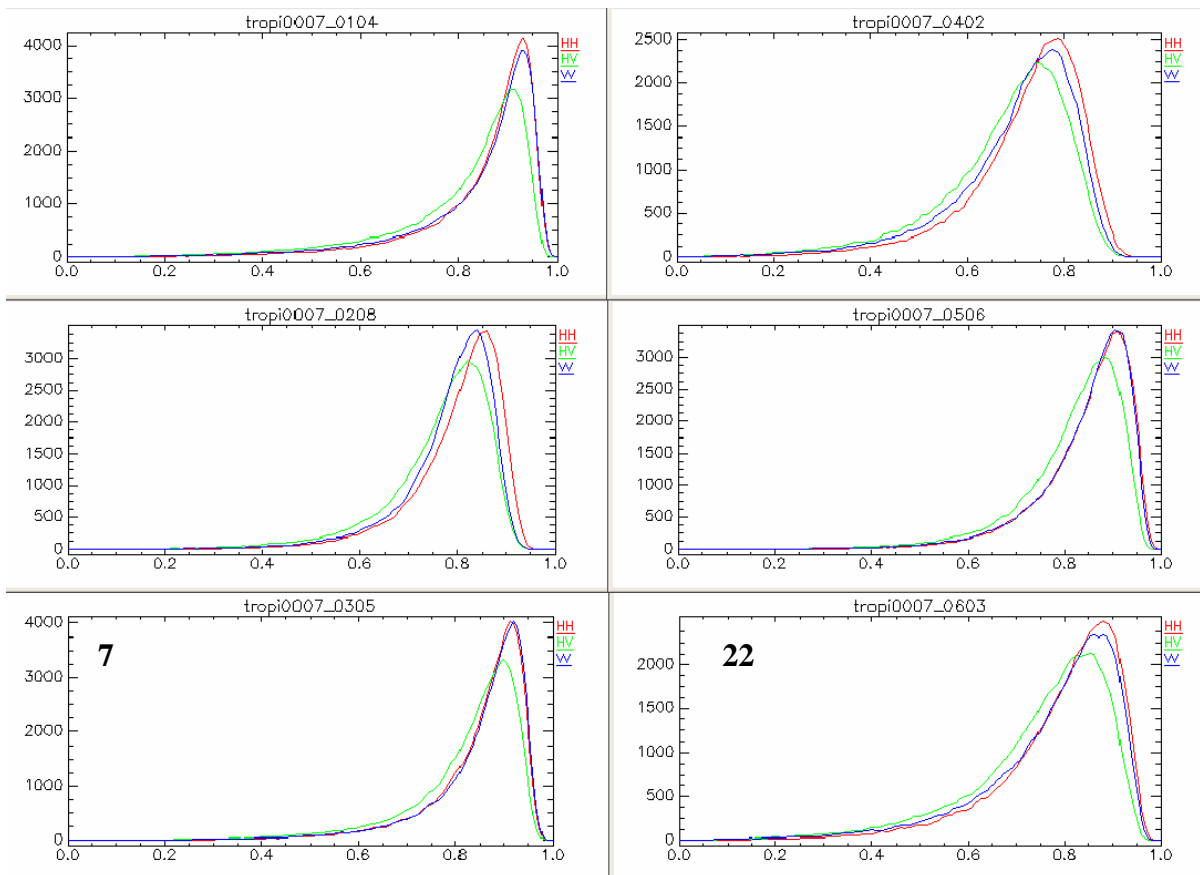


Figure 8-3: Histogram of the interferometric coherence corresponding to the red box in the interferograms presented in Figure 8-1.

Three histograms present a very high coherence value with a peak above 0.9. The loss of coherence experienced between image tropi0007 and tropi0402 (14 day delay) is more important and the interferometric coherence histogram presents a peak for HH at around 0.78 which is rather low compared to all the other interferometric pairs. This cannot be attributed to geometrical conditions as the  $k_z$  over the red zone is very similar to the one observed for the other delays. There is a definite temporal effect affecting this interferometric couple.

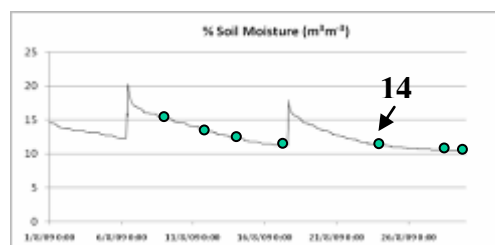


Figure 8-4: Soil moisture measured in the Paracou site. The green dots represent the seven acquisition flights. Flight 4 was acquired after a rain event and correspond to a 14 day delay with respect to Flight 0.



The interesting point is that the coherence is observed to increase for later dates. This marked loss of coherence could be linked to a punctual variation in the backscatter mechanism, linked to the rain event which occurred on the 17<sup>th</sup> of August.

	Temporal baseline	HH			HV			VV		
0007-	days	Ro_0	Ro_1	Ro_2	Ro_0	Ro_1	Ro_2	Ro_0	Ro_1	Ro_2
0104	2	0.93	0.87	0.95	0.91	0.83	0.95	0.93	0.87	0.96
0208	4	0.85	0.77	0.90	0.81	0.73	0.88	0.85	0.75	0.88
0305	7	0.91	0.85	0.95	0.90	0.81	0.94	0.93	0.85	0.95
0402	14	0.79	0.67	0.85	0.75	0.63	0.83	0.77	0.66	0.84
0506	20	0.91	0.83	0.95	0.89	0.79	0.93	0.91	0.82	0.95
0603	22	0.88	0.75	0.93	0.85	0.71	0.91	0.86	0.75	0.93

Table 8-1: Statistics on the temporal decorrelation histograms presented in Figure 8-3.

Table 8-1 summarizes the loss of correlation linked to the temporal baseline. The indicators are defined below and illustrated in Figure 8-5 where:

- Ro\_0 is the coherence of the most populated bin
- Ro\_1: the lower coherence value reach at ½ the histogram height
- Ro\_2: the higher coherence value reach at ½ the histogram height

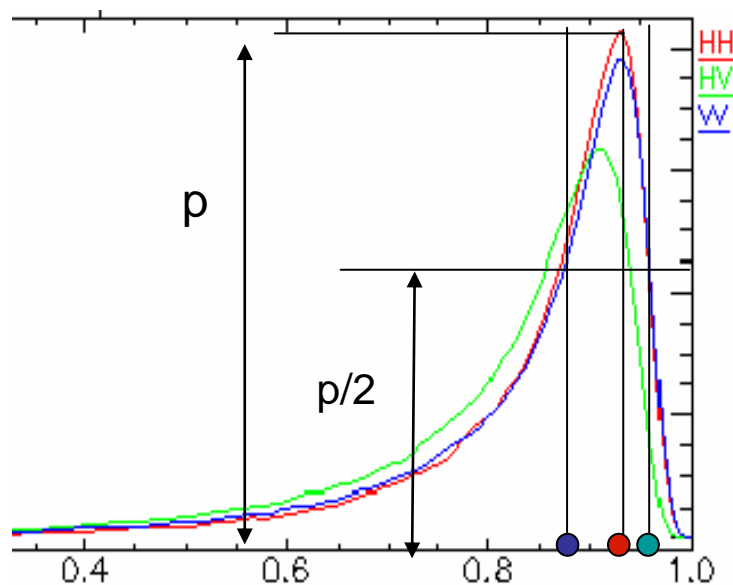


Figure 8-5: Illustration of the indicators –Ro\_0 (red dot) is the most populated bin, Ro\_1 (blue dot) and Ro\_2 (green dot) correspond to the coherence for 1/2 the population of the max.



## 8.2. Forest height inversion result validation from PolInSAR data

### 8.2.1. Method and P band specificity

The PolInSAR height inversion scheme is based on the Random Volume Over Ground model first presented by Cloude and Papathanassiou [Cloude et al., 2003, Papathanassiou et al., 2003]. They applied this model to L-band data acquired by E-SAR.

In a previous study [Dubois-Fernandez et al. 2005, Dubois-Fernandez et al. 2006, Dubois-Fernandez et al. 2008, Garestier et al. 2008.], the PolInSAR inversion at P-band has been addressed. The inversion algorithm based on the RVoG model had to be adjusted to take into account the specificity at P-band. The reasons for that are summarised as follows:

The RVOG model assumes that the contribution coming for the forest can be modelled as the sum of two contributions.

- The first one is the ground contribution attenuated by the crown layer and includes the double bounce return (ground-trunk). The interferometric phase associated with this contribution is simply the one corresponding to the ground height for all possible polarisations. The interferometric coherence is assumed to be 1, after geometric decorrelation correction.
- The second contribution is due to the crown layer only. If the crown layer is modelled as a random volume, it has been showed that the interferometric complex coherence associated with a random volume is independent of the polarisation [Treuhaft et al., 1996].

When both contributions are present (they are assumed independent), the resulting interferometric coherence  $\gamma_T$  can be written as:

$$\gamma_T = f(\gamma_g, \gamma_v) = \frac{\sigma_{0g}}{\sigma_{0g} + \sigma_{0v}} \gamma_g + \frac{\sigma_{0v}}{\sigma_{0g} + \sigma_{0v}} \gamma_v$$

where  $\gamma_v$  is the volume-only coherence,  $\gamma_g$  is the ground coherence and  $\sigma_{0g}$ ,  $\sigma_{0v}$  are the normalised backscatter coefficient associated respectively to the ground scattering (ground + ground-trunk contribution including the attenuation through the canopy) and to the volume return. Both are varying with polarisation and the total coherence is simply the weighted average of the two coherences. As a direct consequence, the weighting factors will vary with polarisation, and the locus of the interferometric coherences will describe a line segment between the point  $\gamma_g$  (ground) and  $\gamma_v$  (volume-only). This simple model is not perfect and some deviation from the line can be observed.

It can be shown from matrix theory that the locus of interferometric coherence will describe a convex set which will be aligned with the line between the two points. The spread around the line can be caused by the model not being an exact representation of the scattering mechanisms, and by the noises in the data.

The inversion scheme as described by Cloude and Papathanassiou [Cloude et al., 2003] can be summarised in four steps:

- (1) synthesize many interferometric coherences by varying the polarisation of the transmit and receive antennas and identify the line AB.





- (2) identify the two intersection points between the line AB and the circle, choose between the two the one associated with the ground  $e^{i\varphi_0}$  as being the one closer to the HH coherence and furthest to the HV coherence.
- (3) select the interferometric coherence furthest from the ground coherence as  $e^{i\varphi_0}\gamma_V$ .  
This assumes that there is a polarisation state of the transmit and receive antenna such that there is no contribution from the ground.
- (4) from  $\gamma_V$ , invert the vegetation height and attenuation from.

$$\gamma_V = \frac{\int_{h_v}^0 \sigma_{0l} e^{uz} dz}{\int_{h_v}^0 \sigma_{0l} e^{vz} dz} = \frac{\int_{h_v}^0 e^{uz} dz}{\int_{h_v}^0 e^{vz} dz} = \frac{v \left[ \frac{e^{uz}}{u} \right]_{h_v}^0}{u \left[ \frac{e^{vz}}{v} \right]_{h_v}^0} \text{ with } u = 2 \frac{\sigma_x}{\cos \theta} + ik_z \text{ and } v = 2 \frac{\sigma_x}{\cos \theta}$$

This equation reflects the fact that the volume can be modelled as a succession of identical layers, each one characterised by a backscatter coefficient  $\sigma_{0l}$ .  $\theta$  is the incidence angle. In the denominator, the scattered power is just the sum of the contribution of each layer weighted by the attenuation resulting from the roundtrip through the layers sitting on top with the attenuation coefficient being  $\sigma_x$ . In the numerator, the interferometric phase associated with each layer is also introduced. Because all layers are identical and independent, the  $\sigma_{0l}$  term vanishes.

In previous studies on PolInSAR, we have concluded that at P Band, the ground contribution is significant in all polarisations. This is clearly linked to the increased penetration expected at lower frequencies. As a consequence, the initial algorithm proposed by Papathanassiou and Cloude [Cloude et al., 2003] could not be used directly. Remember that this algorithm was first designed for L band data, for which HV is mostly dominated by the vegetation contribution. The volume only interferometric coherence  $\gamma_V$  can then be inverted directly, into a height and an attenuation coefficient through the vegetation. The inversion provides a unique solution.

Because at P band the canopy-only response is never observed, the problem does not have a unique solution. Estimating the height requires injecting other information.

Several possible approaches can be followed. Fixing the attenuation coefficient through the vegetation is the most straightforward and this is the one we have proposed when working with the P band data over the Nezer forest [Dubois-Fernandez et al., 2005]. Other path can be envisioned, for example by increasing the number of observables via multiple baselines.

The previous ONERA studies were conducted over temperate forest. The first one concluded that PolInSAR at P band over the Nezer forest provided an excellent estimation of forest height, with a 1.2m RMS error for forest height ranging from 6 to 25m. The second one was over the Remingtorp forest and was based on E-SAR data. The main conclusion was that the ground return could not be neglected, even at HV polarisation, and this observation was confirmed by the tomographic analysis presented by Rocca and Tebaldini [Tebaldini, 2009].

### 8.2.2. Ground contribution in the HV polarisation over Tropical Forest

The tropical forest is known to be denser and the relative contribution of the canopy and the ground needs to be evaluated in these new conditions. The forest is denser and we expect a



higher attenuation coefficient. The forest is higher and the vegetation layer is thicker. These combined effects, longer path through the vegetation and higher attenuation could very well result in the fact that the ground contribution is no longer present at HV. This is the first point we analysed with the TropiSAR dataset.

In this illustration, the phase centers associated with the different polarisations are positioned in the unit circle for an zone inside ROI 16, a reference plot with an average tree height around 30m and a maximum height of 50m. The phase centers are along a line, in agreement with the RVoG model, also known as the line model. The three lines represent three iso-attenuation curves for the volume only coherence. The blue curve is with an attenuation coefficient of 0.1, while the red curve corresponds to a higher attenuation coefficient. The green cross is the interferometric coherence corresponding to the HV polarisation. If the model assumptions were valid and if the HV coherence corresponded to a canopy-only response, then we would expect to see the green cross along the line but inside the region between the blue and red curves. This is not the case and we can conclude that either the model is not valid or the vegetation only response is not observed.

Here the estimated height is 31.6m for an attenuation coefficient of 0.3dB/m, which is the attenuation selected for the Nezer forest.

This analysis was conducted on many sites and the same conclusion was reached again and again. Either the ground contribution is still present in all polarisations or the RVoG is not valid. The assumptions underlying the RVoG can be questioned.

The first assumption is to say that the overall scattering is resulting from two different objects, the volume and the ground. The ground includes the direct ground return, the ground/trunk interaction as in the double-bounce. The scattering from these two objects is assumed to be statistically independent. This assumption seems physically sound given the high number of scattering elements involved in the volume scattering.

The second assumption is that the volume only coherence and the ground only coherence are independent of the polarisation. This assumption fails if the volume is oriented. However, this assumption results in the alignment of the interferometric coherence along a line, which is what is observed in the TropiSAR data set. If the volume was strongly oriented, the shape of the coherence region will diverge from a line.

The third assumption is that the vegetation behaves like the cloud model, a homogeneous volume. This assumption is the most questionable. The longer wavelength is certainly sensitive to the larger elements of the canopy, like the trunks which are larger at the base than in the top part of the tree.

However, in the case of the tropical forest, the tapering of the trunks is rather small, with a forest being composed of vertical cylinder for its major part. To quantify further this statement, we can refer to the paper by [Chave, 1995] in which the authors provide the behavior of the diameter as a function of height based on the measurements over 2410 harvested trees over 27 study sites in the tropics.

$$D_z = D_0(1 - z/H)^{0.271}$$

The diameter at  $\frac{3}{4}$  of the tree height is around 0.69 times the reference diameter.



In the remainder of this study, we have assumed that the vegetation behaves like an homogeneous layer and that the vegetation only scattering is not observed.

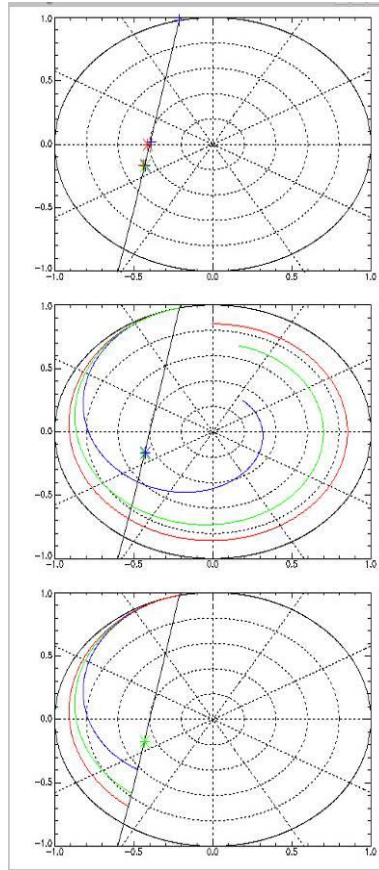


Figure 8-6: Interferometric coherence circle for an area inside the ROI 16.

### 8.2.3. The dataset analysed in this study

The TropiSAR dataset is large and contains many images which can be analysed with the PolInSAR technique. In this report, we restrict the analysis to two interferometric couples, acquired during Flight 4 over Paracou as it includes many different baselines with the least temporal decorrelation (all acquisitions were acquired within a 2 hour period).

We selected acquisitions tropi0402 and tropi0404, which were flown with a 100 foot vertical shift. In order to present the analysis and evaluate the result we have selected an area of 1000m in range and 1000m in azimuth.

The forest in the Paracou area does not present striking spatial height variations at the 100m scale. Indeed, the tree height can vary significantly from one tree to the next as the forest includes a few very high and large trees, but the variation is very similar from one spot to the next when the observation is performed at a larger scale. There are only a few exceptions. When we are closer to the river, the vegetation is lower; it corresponds to a potentially flooded





area forest. Besides the lowlands, the plots which have been logged the most (Treatment 3) are also showing a small height variation compared to the surrounding forest. In the image, we selected a zone containing sufficient natural variation to provide an interesting case for PolInSAR height map evaluation.

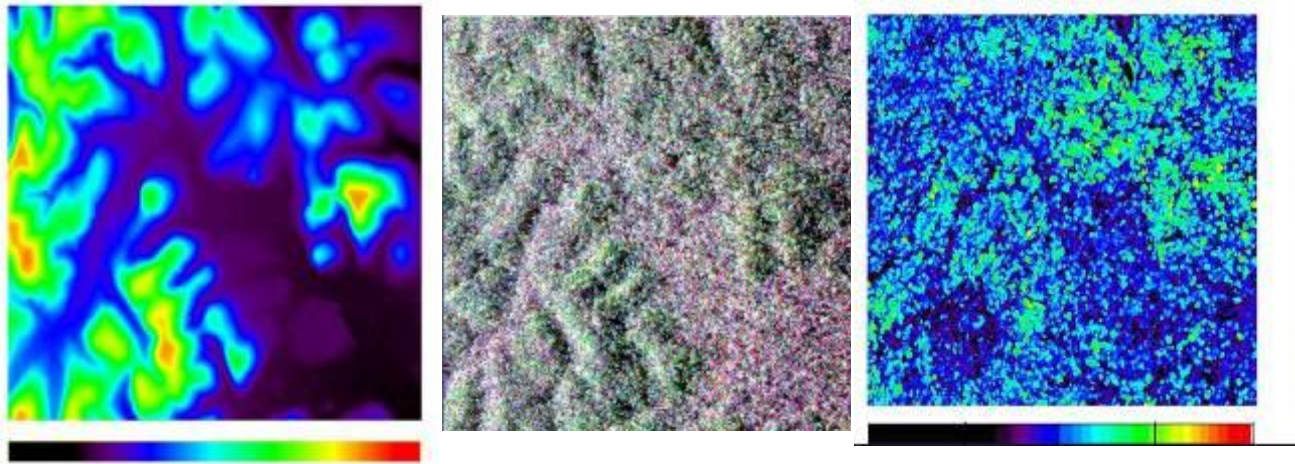


Figure 8-7: LiDAR derived DEM (color bar = [0,40m]), radar image [HH,V,VV], LiDAR derived canopy height (color bar = [0,60]) Note that the topography is marked and that the vegetation height is mostly between 25 and 35 m.

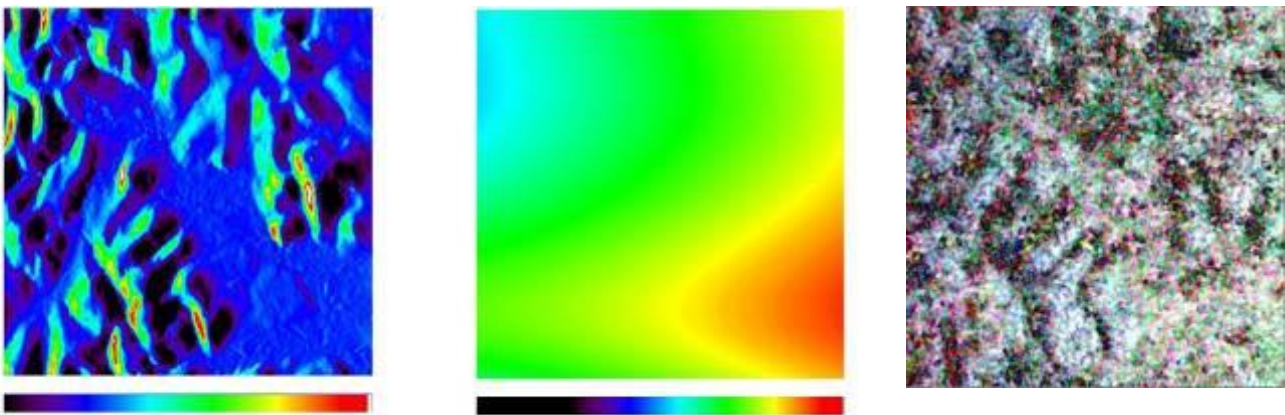


Figure 8-8: Over the study area, the slope image - color bar=[-10°,30°], the altitude of ambiguity - color bar=[40m,80m], the interferometric coherence (HH,HV,VV).

This zone will be the basis for presenting the PolInSAR height inversion. The zone is presented in the Figure 8-7. Over the same area, we present the altitude of ambiguity, the coherence map and the interferometric coherence map.

Over the study zone, for the interferometric couple 0402-0404 the altitude of ambiguity ranges between 61m and 76m, well above the average tree height in the area. The corresponding baseline was selected in order to provide the correct altitude of ambiguity for P band over this type of forest and we will come back later in the analysis on the influence of the baseline on the inversion performance.





Figure 8-8, one can see that the interferometric coherence varies drastically with the slope. It is more coherent when the slope is facing away from the radar, less coherent in the areas where the slope is facing the radar. This is the results of combined effects:

- The ground contribution presents a decorrelation linked to the fact that there is a height variation inside the resolution cell.
- The volume decorrelation is also more important as the effective  $K_z$  varies with the incidence angle.

Our current standard PolInSAR inversion algorithm does not take into account these variations and a new version is currently tested.

In this report we present the inversion obtained with our standard algorithm, therefore not taking into account topography. But clearly, the topography as a strong influence on the coherences and should be taken into account.

#### 8.2.4. PolInSAR height inversion – effect of the attenuation

We have established that under the RVoG model hypothesis, the ground contribution is always present, no matter the polarisation. Even at HV polarisation, the ground is contributing. Therefore, in order to perform the inversion from a single baseline, we need to select the attenuation. From measurements over a hard target, we had estimated that the attenuation over the Nezer forest (temperate, plantation forest) was around 0.3dB/m. We also had confirmed that varying the value of the attenuation coefficient in good baseline condition had a mild effect on the inversion, creating a homothetic shift in the inverted height. We expect the attenuation to be larger over tropical forests. We started our analysis by investigating the effect of this parameter on the inverted height map. The PolInSAR estimation is performed on a 19x19 pixel sliding window.

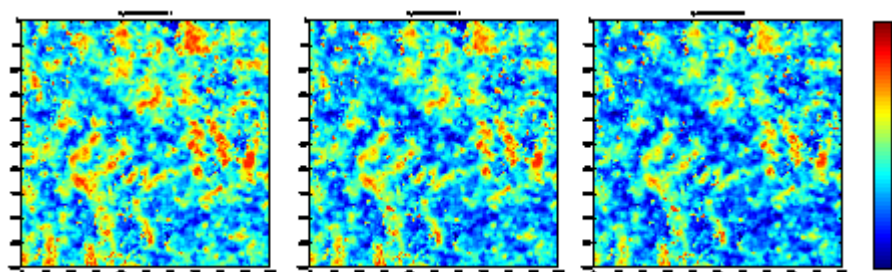


Figure 8-9: PolInSAR estimated vegetation height maps over the study zone (color bar=[20,45m]) for three attenuation coefficients 0.3dB/m, 0.4dB/m and 0.5dB/m.

The overall structure of the estimated height map is conserved when varying the attenuation coefficient between 0.3dB/m to 0.5dB/m. As expected the estimated height decreases as the attenuation increases. However, the global behaviour is very similar and the overall structure of the zone is found to be identical with a low zone in the bottom right of the image, corresponding to the beginning of the occasionally inundated forest closer to the river and a lower zone in the middle left of the image, corresponding to a logged area.

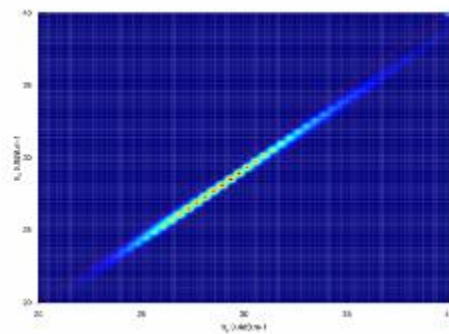


Figure 8-10: A 2-D histogram comparing the PolInSAR height obtained with 2 different attenuation coefficients, 0.4 dB/m and 0.5dB/m. There is a 0.8m bias and a 0.16m RMS between the two estimations. The red line is the 1:1 line.

The observed differences are quantified more precisely in Figure 8-10 where the PolInSAR height estimations obtained with a attenuation of 0.4dB/m are compared to the ones obtained with a 0.5dB/m attenuation. The observed bias, computed as the mean difference between the two estimations, is 0.8m and the RMS difference is 0.16m.

In order to select the attenuation, we proceeded as follows: over an area outside the study area presented in the above figures, we selected several zones, performed the attenuation inversion assuming the LiDAR height was the vegetation height. We then estimated the attenuation based on these observations. We observed that there is spread in the estimated attenuations and we selected the median value. Note that the attenuation is not a sensitive parameter and therefore, its estimation remains noisy. This analysis resulted in the selection of an attenuation of 0.4dB/m.

When comparing and evaluating different height maps, we ran into a difficult problem: the spatial filtering. Using different spatial averaging, different smoothing filters change the resulting map and the perception one can have of the result. This point is even more critical when comparing LiDAR derived height maps to PolInSAR derived height maps, as illustrated in the analysis performed on the spatial filtering of the LiDAR data, later in the document.

#### 8.2.5. Comparison between the inversion results from two interferometric couples

The same inversion algorithm was used to estimate the vegetation height from another interferometric couple: tropi0402 and tropi0405. The intended baseline is now a 150 feet vertical shift between the two trajectories resulting in a height of ambiguity of around 40m, close to the mean vegetation height in the study zone.

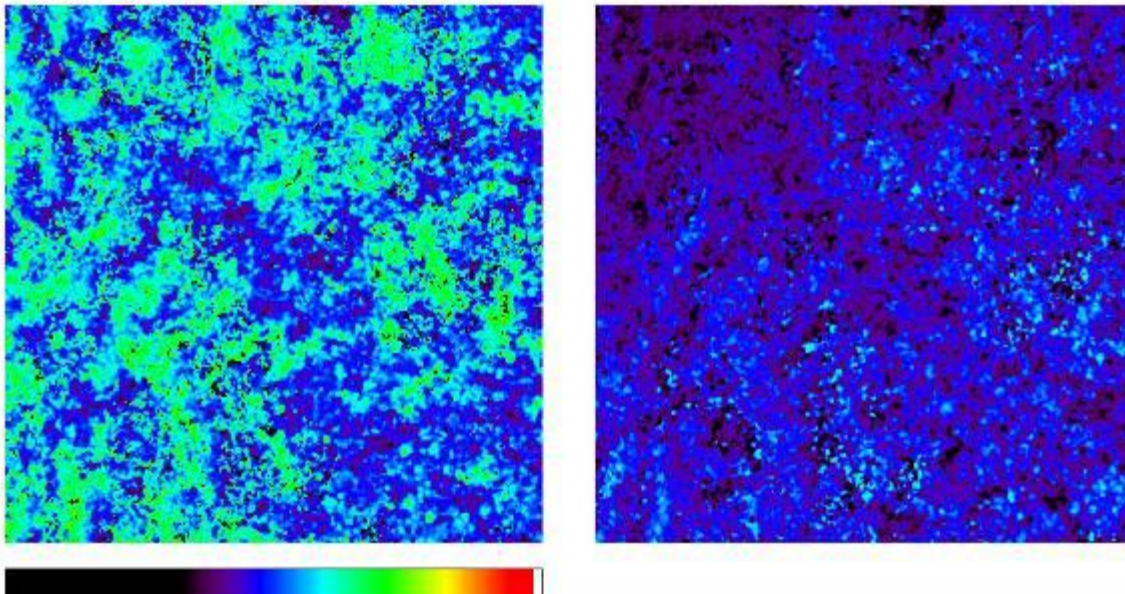


Figure 8-11: PolInSAR vegetation height map from 100 feet vertical baseline on the left, 150feet vertical baseline on the right. The altitude on ambiguity is between 61 and 76m on the left and is between 32 and 49m on the right. The color bar ranges from 0 to 60m.

There is a noticeable shift in the estimated height between the two images. The height shift is between 5 and 10m. The lower areas in the left images are also the lowest areas in the right images.

We compared the estimated height on a pixel basis and we formed a 2D histogram where the X axis is height from tropi0402-tropi0404 the 100feet vertical baseline couple and the Y axis is the height from tropi0402-tropi0405 the 150 feet vertical baseline. This 2D histogram is presented below.

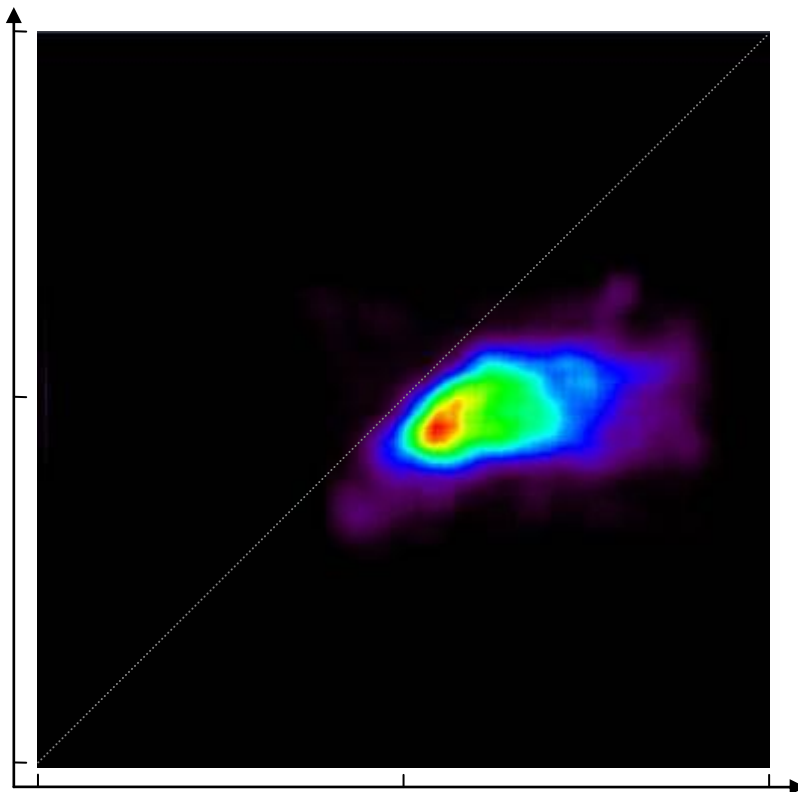


Figure 8-12: 2D histogram between the vegetation estimated heights from tropi0404 and tropi0405. The two axis range between 0 and 60m. The color indicates the population of the 3D histogram with the red color corresponding to the most populated bin.

The 2D histogram shows that when the baseline is not adapted and the height of ambiguity is too small compared to the vegetation height in the area, the PolInSAR estimated height is underestimated and reaches a saturation level close to the altitude of ambiguity. This is to be expected from the algorithm implementation.

This analysis indicates that the choice of the baseline is essential in order to perform meaningful height estimation. It has to be selected such that the altitude of ambiguity is between 1.2 and twice the maximum vegetation height.

### 8.2.6. The LiDAR data

The LiDAR canopy height information was provided by CIRAD and can be obtained directly from the Kourou Ecofog team. It was derived from the raw LiDAR information. This information is not part of the TropiSAR database for the moment.

The LiDAR canopy height information has a level of details not accessible to PolInSAR technique. The pixel posting is 1m for the CEM (Canopy Elevation Model). In order to validate the PolInSAR vegetation height map, it was decided to pre-process the LiDAR data. In order to facilitate the repeated comparison with the Radar data, we projected the LiDAR CEM into the radar image geometry. It is clearly a short cut intended to ease the technical work, whereas a more logical approach would have been to perform the comparison in a geographic projection. This will be done when the algorithms are fine-tuned and ready to produce validated height





maps. But for the time being, the common geometry used for the comparison is the radar geometry. The radar geometry has a 1m posting in range and azimuth making it comparable to the LiDAR postings.

In the initial comparison, we projected the LiDAR data in the radar geometry, based on the DEM information. However, when comparing the projected LiDAR canopy height with the PolInSAR estimated height, we noticed that there was a shift in range. We decided to project the LiDAR data taking into account the canopy height. The height used in the projection is therefore the sum of the ground height and the vegetation height. This is illustrated in the following figure.

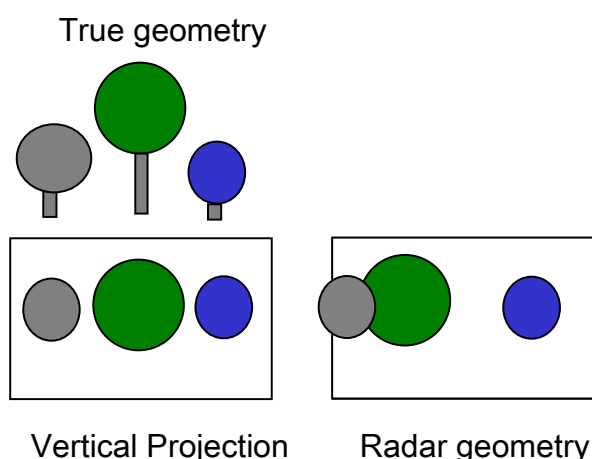


Figure 8-13: Remark about the projection of tree height into the radar geometry. One should take into account the ground height + vegetation height to match the foreshortening observed in the radar image.

Once the LiDAR data is projected, it is filtered. The PolInSAR inversion is conducted over a 19x19 sliding window. The question was how to filter the LiDAR data to match the PolInSAR estimation resolution. This is not the main purpose of this analysis and our approach has no pretention of being complete. However, we did apply a filtering to the LiDAR data and it needs to be reported with care as the averaging option which is chosen can have a significant impact on the output result.

In previous studies, we did not have to address this question as over the Nezer forest, the plots are very uniform with almost no height variation between adjacent trees as they were all planted at the same time. The question about how to deal with a height distribution in the tree population was not relevant to a plantation forest. Other teams [Mette, 2007] who had to work with natural forest proposed to base their analysis on a standard forestry parameter called the H100. The H100 parameter corresponds to the average tree height of the 100 tallest trees per hectare. This is an in-situ measurement parameter. With this parameter, the forest is characterised by the tall trees only. In the case of evaluating forest biomass, this approach is meaningful as the biomass is dominated by the biomass of the largest trees in a plot rather than the average of the living plant height.

The H100 parameter is also a convenient parameter for in-situ measurements. To establish this parameter, the forest staff needs to identify the tallest trees in a plot and limits the height measurements to these trees. From a LiDAR perspective, this is more complicated. The LiDAR has a regular spatial posting, and not one height per tree as in the in-situ measurement. This has the effect of associating more measurement points to the tallest trees as there are



usually larger in crown size. To match exactly the H100 measurements, the analysis of the LiDAR data would have to proceed along the following steps.

- 1) Identify the crown area and extract one height per crown area or tree.
- 2) Identify the N tallest trees in the plot
- 3) Perform the average.

The H100 parameter has a meaning at the plot level as it is designed for a 1ha plot, but not as a spatial parameter. Nevertheless, as pointed out by the DLR team [Mette, 2007], putting more weight on the tall or large trees while averaging makes sense for the common forestry applications.

Following this reasoning, two filtering techniques were tested on the LiDAR data.

- Filter 1: over a sliding window of size  $N \times N$ , assign the value of the maximum height
- Filter 2: over a sliding window of size  $N \times N$ , assign the average height

These two filters are tested on the LiDAR data and the result is presented in Figure 8-14. In the tropical forest, there are a few very tall trees above a dense mean canopy and this strong variability in height is responsible for the important differences in the height maps computed with the different filters. As expected, the difference is small when using a  $3 \times 3$  sliding window. However, when degrading the resolution such as to be compatible to the one associated with the PolInSAR inversion, the differences are striking. When comparing the range of height in the  $3 \times 3$  images and the  $19 \times 19$  images, we observed that the averaging filter preserves the range of height (the map has globally the same behaviour, the same color) whereas the maximum filter overestimates the height. From this analysis, we decided to use the mean height in the tropical forest context rather than the max height.

Note that this conclusion is a direct consequence of the structure of the tropical forest, characterised by a dense forest with a few dominant trees. This is not applicable to temperate or boreal forests, where the tree heights are more clustered and where there are many points where there are no trees.

We selected Filter 2, with a  $19 \times 19$  box size.

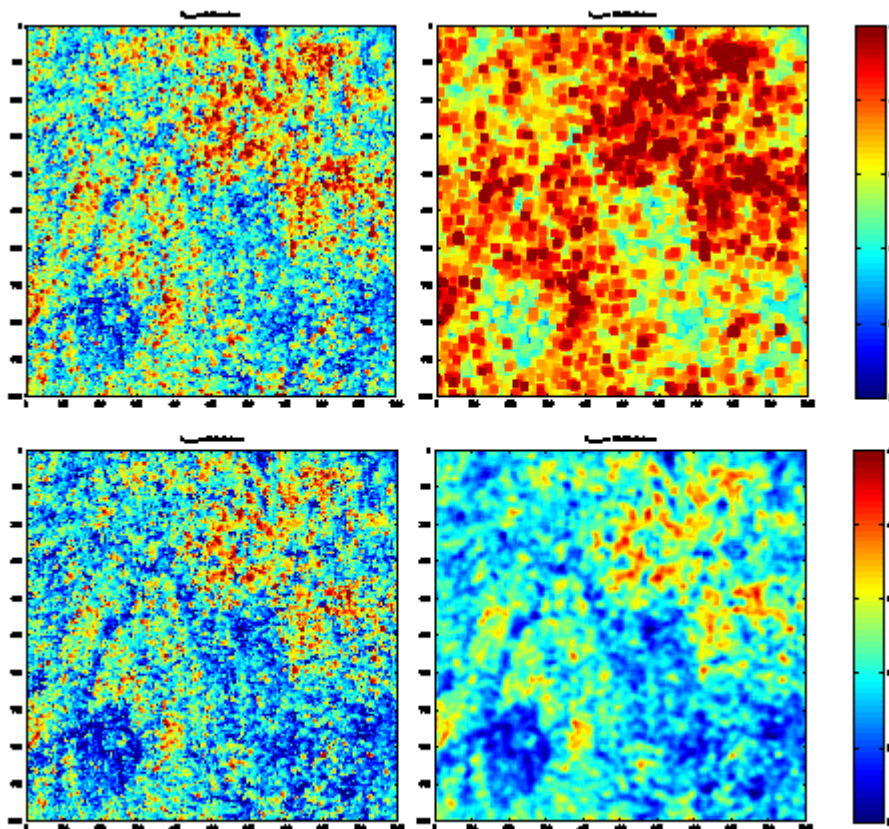


Figure 8-14: LiDAR data: top row : Filter 1 (max) with a 3x3 box, Filter 1(max) with a 19x19 box, bottom row: Filter 2 (mean) with a 3x3 box, Filter 2 (mean) with a 19x19 box. For the PolInSAR estimation evaluation, we selected the mean filter with a 19x19 box (bottom right map). The color bar is similar on all map and ranges from [20-45m].

### 8.2.7. Comparing the PolInSAR inverted height to the LiDAR derived CEM data

Figure 8-15 illustrates the comparison between the LiDAR derived measurements and the vegetation height estimated from PolInSAR technique. The lower middle zone is clearly identified on both dataset so is the lower right region, corresponding to lowland forests subject to occasional inundation. The lower zone at the bottom left of the LiDAR image is not identified as clearly in the PolInSAR height map. This could be linked to the presence of isolated taller trees or the marked topography in the zone. Remember that the height variation between the lower zones and the highest zones is very small in average, around 6m at most.

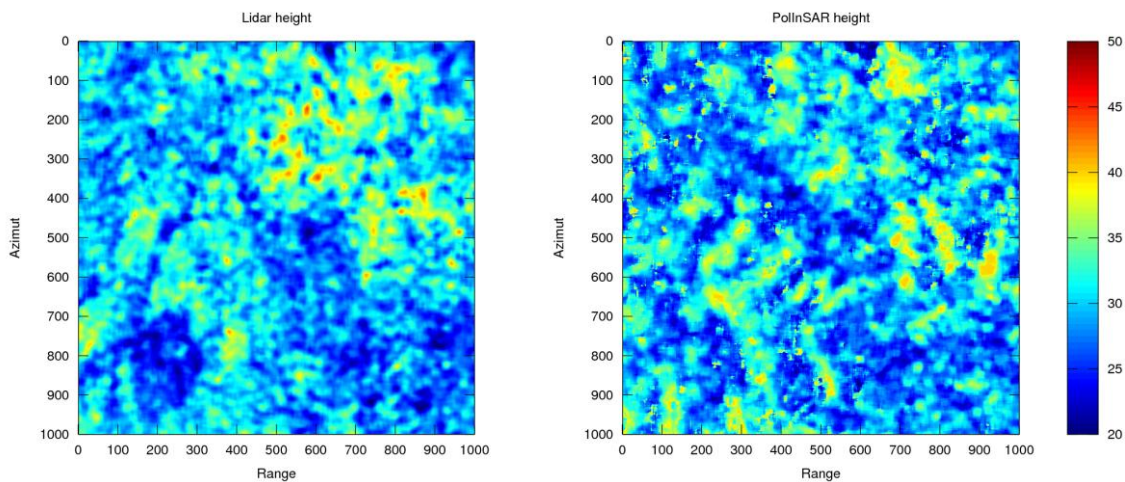


Figure 8-15: Comparing the LiDAR canopy height on the left to the PolInSAR vegetation height on the right.

The comparison can be performed pixel to pixel. A 2D histogram is formed where the X axis is the PolInSAR derived height and the Y axis is the LiDAR canopy height map. The full zone is used to compute the histogram.

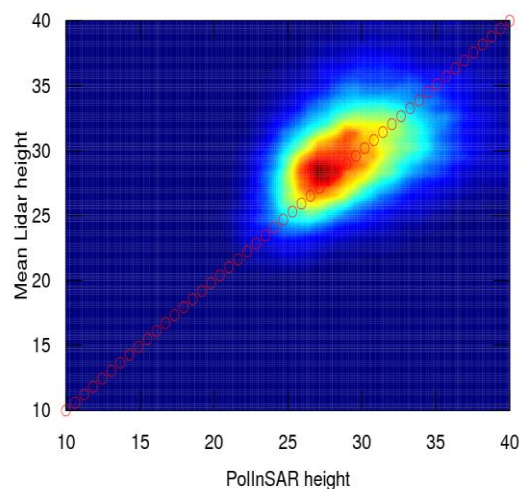


Figure 8-16: 2-D Histogram with the PolInSAR retrieved height as X axis and the LiDAR canopy height as Y axis. The color indicates the number of pixel in the bin where red is the most populated bin. The bias is less than 1m and the RMSE is around 4m.

The histogram indicates that the estimation is unbiased with respect to the LiDAR canopy height information. This is linked to the choice of attenuation. The height extend is similar between the technique.



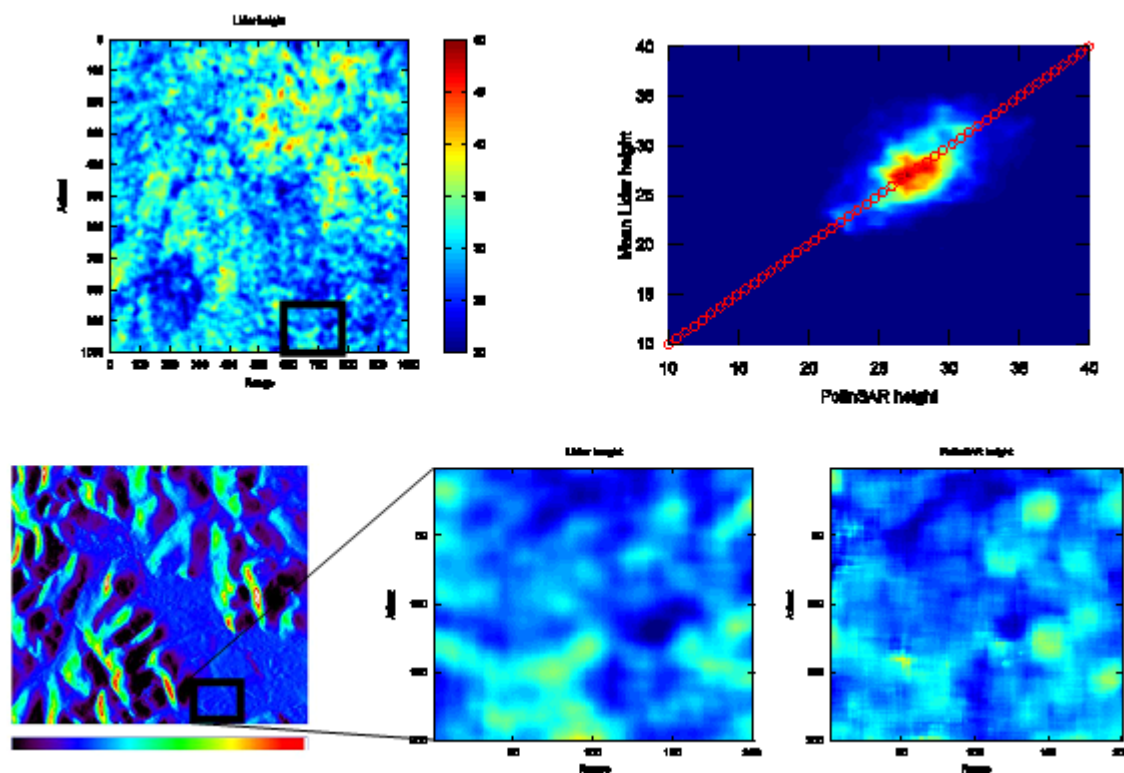


Figure 8-17: Zoom from Figure. 8-16 over a flat area. The RMSE is 3.0m.

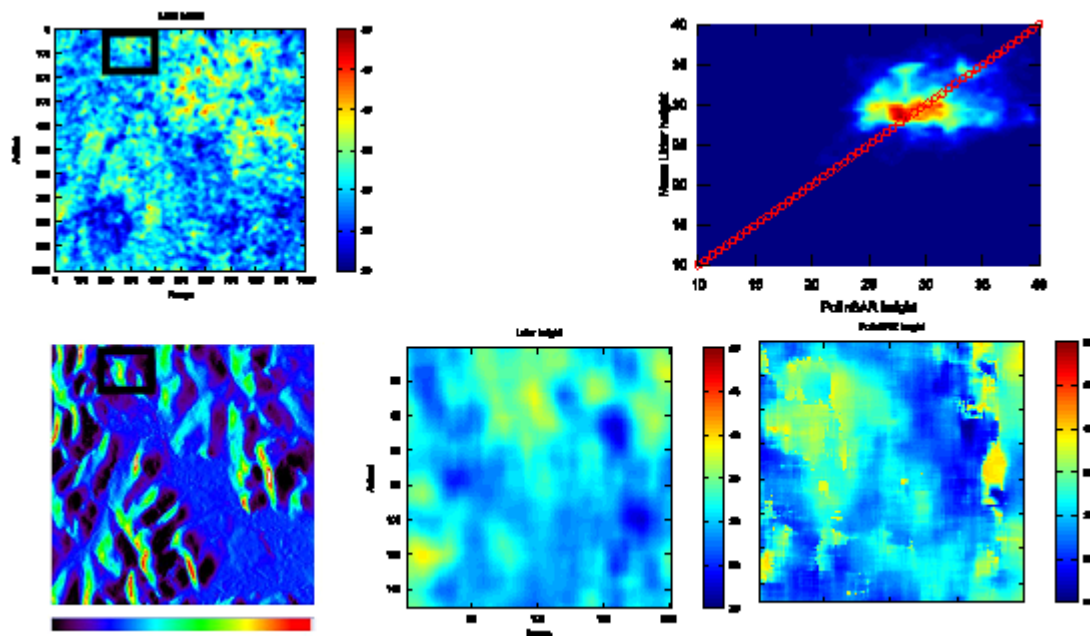


Figure 8-18: Zoom from Figure 8-16 over a relief area. The RMSE is 4.3m.

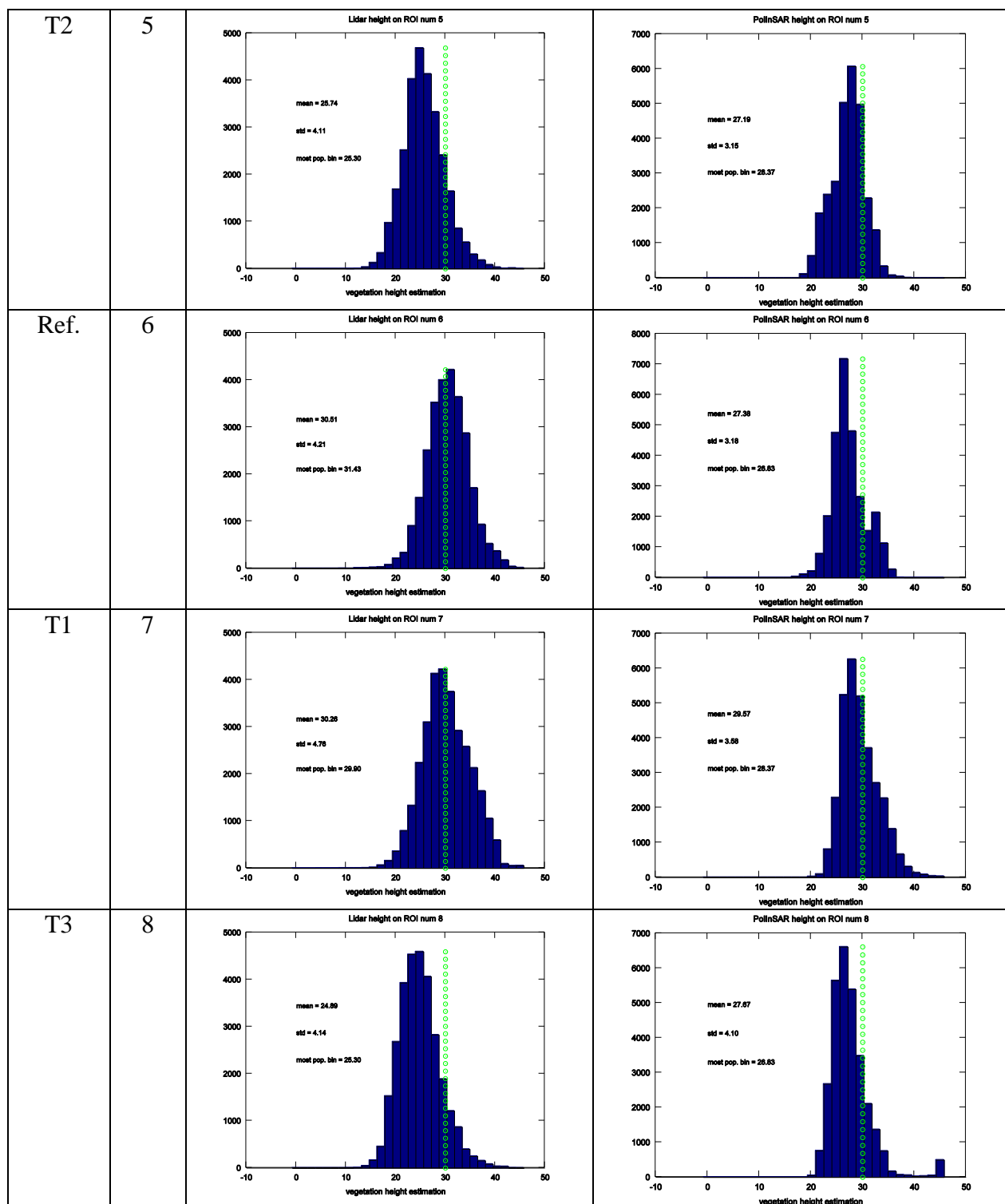
In the area where there is a marked topography (Figure 8-18), the comparison is not as consistent and the inversion algorithm needs to be improved. The PolInSAR height seems to be

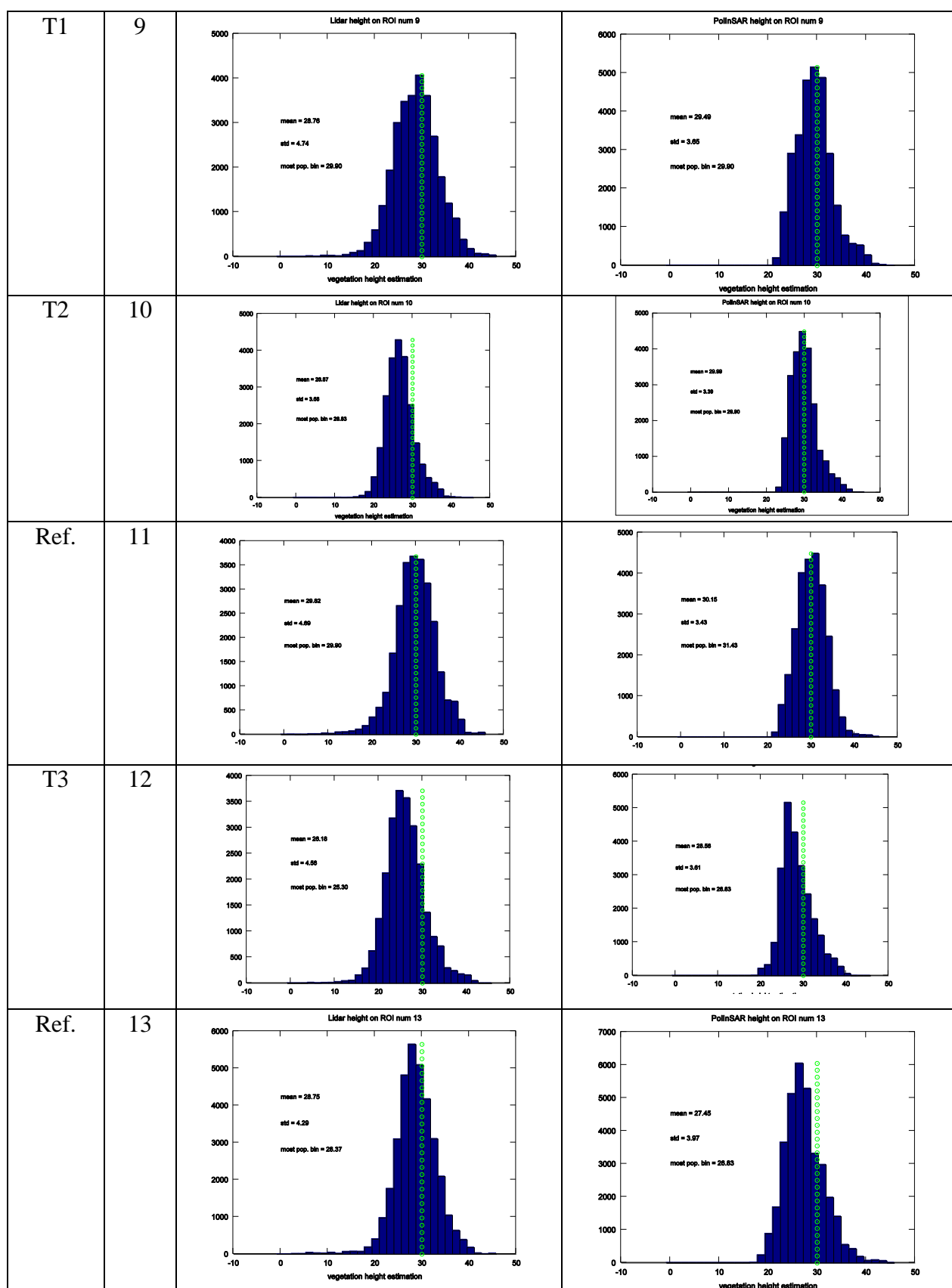


shifted with respect to the LiDAR height. This cannot be explained by an error in localisation in the radar geometry as the slant range geometry is well mastered.

To finalise this evaluation, we will compare height histograms from the 16 plots monitored by CIRAD.

Treat.	ROI #	LiDAR height histogram	PolInSAR Height Histogram
Ref.	1		
T1	2		
T2	3		
T3	4		







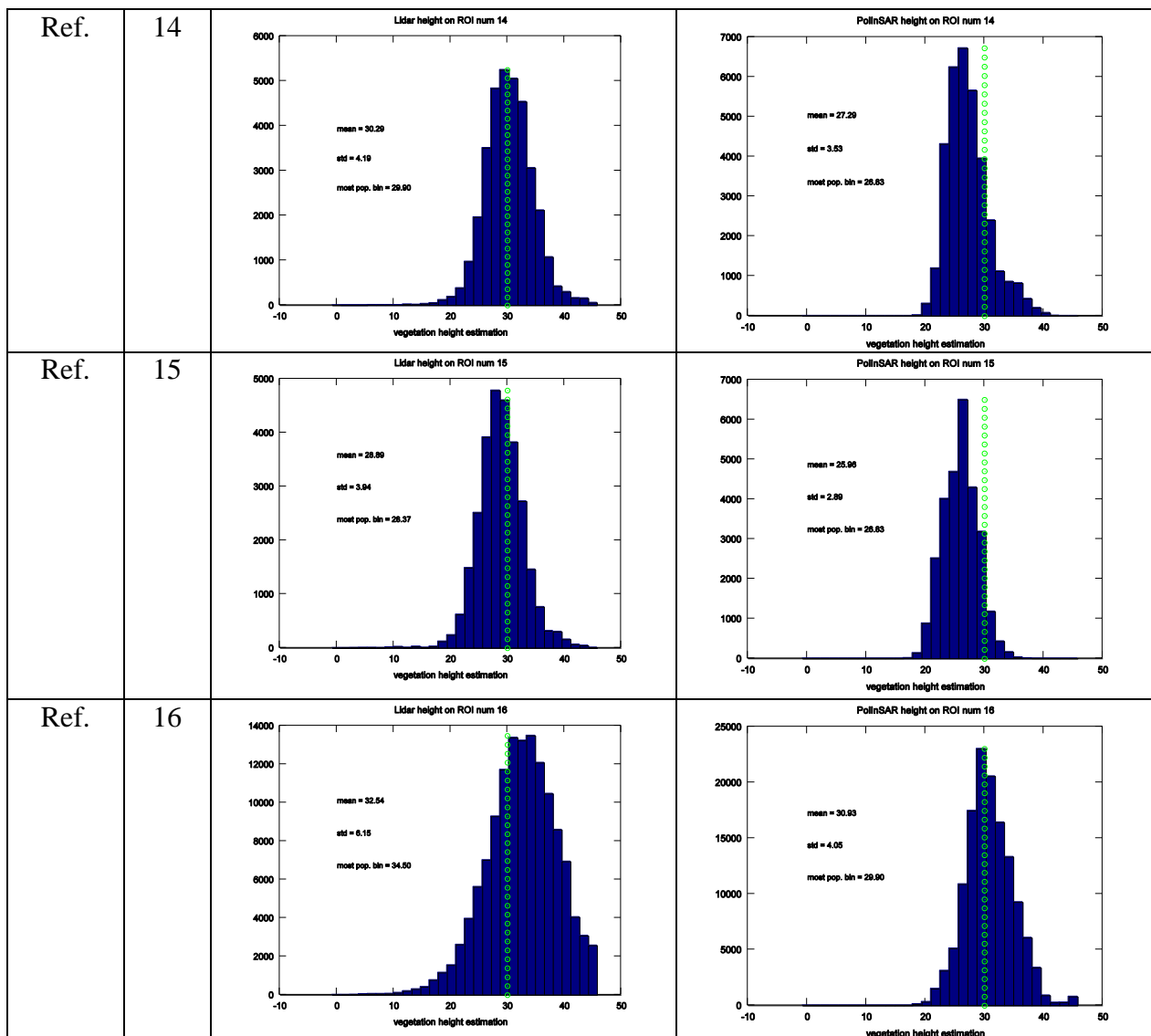


Figure 8-19: PolInSAR mean height versus LiDAR mean height for the sixteen zones.

The main conclusions of this first analysis on PolInSAR data can be summarised with a few key points:

- The experienced temporal decorrelation over 22 days is small at P Band, with a decorrelation around 0.9.
- The first PolInSAR height inversion results are good with an RMS error of less than 5m.
- In the inversion scheme we selected (based on a given attenuation coefficient), the influence of the attenuation was explored for the vertical baseline of 100ft. It does not appear to be a critical parameter and will simply shift the inverted height. The shift is 0.8 m when going from 0.4dB/m to 0.5dB/m.
- The selection of the baseline was observed to be extremely critical. It has a major effect on the inversion.



- Important slope effects were observed and a new version of our algorithm needs to be developed to take this effect into account.

## 9. CONCLUSIONS

The TropiSAR campaign was conducted in French Guiana in the summer 2009 in the framework of the Phase A studies pertaining to the BIOMASS mission, one of the three for Earth Explorer candidates. Its main objectives were the evaluation of P-Band radar imaging over tropical forests for biomass and forest height estimation.

An extensive in-situ database, acquired over several decades, was made available by the Guyafor Project. Two main forest sites have been studied: Nouragues and Paracou. New plots were identified and measured under this contract. All together, the dataset includes 157 ha of forest plots, for which all trees with a diameter larger than 10cm have been tagged, positioned and measured. This totals more than 98000 trees. Over these plots, the biomass ranges from 10t/ha for a Coco plantation to 490t/ha for a plot of undisturbed forest.

Seven SAR flights were conducted with the SETHI system from ONERA during the 23 days of the SAR campaign which lasted from August 10<sup>th</sup> to September 1<sup>st</sup> 2009. The selected waveform is characterised by P and L simultaneous acquisitions with a range resolution of around 1.5m. During these flights, a temporal dataset characterised with a zero spatial baseline was acquired to allow the quantification of the temporal decorrelation, one key parameter for the performance evaluation of the PolInSAR technique in a single-satellite configuration. A PolInSAR and tomographic database was also acquired with vertical baselines of 50, 100, 150, 200 and 250 feet.

The processing of the SAR data included a crosstalk removal step at P-Band resulting from a double bounce effect on the wings. The overall calibration accuracy was found to be  $\pm 0.5$ db, with a NE sigma0 better than -30dB and a cross-talk level better than -25dB. The geometric accuracy of the SAR data was measured to be better than 10m, which is the level of accuracy of the reference points used in the evaluation.

The in-situ error analysis identified three main sources of error in the in-situ measurements: the error in the field measurements, the error in the allometry and the error linked to the size of the measured plot. The field measurements (mostly DBH) are precise and do not impact significantly the biomass estimations. The allometric equation is the major source of uncertainty and it was evaluated to be around 5%. The plot size is of major importance and the estimation accuracy for a plot size of 1 ha is estimated to be 10%. This uncertainty drops to 5% if the plot size exceeds 4 ha. Furthermore, the in-situ biomass estimation does not include the small trees (diameter less than 10cm), the lianas and the dead trees. This creates a bias of the order of 10%.

The TropiSAR backscatter coefficients have been analyzed in terms of polarimetric, temporal and incidence behavior. The following observations were made on the Paracou test site:



- The high correlation between polarized backscatter coefficients, at HH, VV and HV polarizations denote the specific scattering mechanisms of tropical forests as compared to boreal or temperate forests previously under study.
- The backscatter coefficients were observed to have a high temporal stability during the campaign,
- The effect of elevation angle of these dense medium is better compensated by a new normalized coefficient  $\alpha^0$ , as compared to the classical  $\gamma^0$ .
- The topographic effect needs to be accounted for. In the absence of DEM whose resolution is compatible with the SAR data spatial resolution, interpolated SRTM DEM can be used to correct for the topography,
- The relationships between the backscattering coefficients  $\alpha^0_{HV}$  with in situ biomass are in good agreement with the trend derived from previous experiments in other forest sites (temperate, boreal, , However, the sensitivity to biomass in the high range of biomass (300 t/ha) is relatively small, and this requires appropriate analysis and processing prior to biomass inversion.
- The preliminary inversion using HV backscattering coefficients has provided mapping results with RMSD of less than 20%.
- The combination of different SAR measurements derived from intensity and PolInSAR, e.g. using a Bayes inversion approach, was found to improve the inversion performance

The PolInSAR analysis dealt with two different aspects, the temporal decorrelation analysis and the PolInSAR vegetation height estimation. The following conclusions were reached:

- The loss of coherence due to temporal baseline was shown to be small even after 22 days. We observed for one date a more pronounced loss of coherence certainly linked to weather conditions with a recovery in the coherence for the later dates. The coherence variation with respect to temporal baseline is not monotonously decreasing.
- The PolInSAR height inversion based on a single baseline approach was evaluated against the LiDAR derived canopy height model. The overall behaviour of the estimator is good with a RMS error of 5m with zero bias. The attenuation coefficient, which in the case of a single baseline inversion at P-band needs to be set (in tropical forest 0.4dB/m) is shown to have little effect on the inversion. A proper selection of the baseline is essential for good estimation.

As a summary, the preliminary analysis of the TropiSAR has shown that it is possible to retrieve biomass of the dense tropical in French Guiana, using appropriate data analysis and inversion approaches. Current works are undertaken to analyze the data of the Nouragues test site, and to derive information on PolInSAR and tomography which can be used to improve the inversion results.

## 10. REFERENCES

[Akima, 1978], Akima H., 1978. A method of bivariate interpolation and smooth surface fitting for irregularly distributed data points. ACM Trans. on Math. Software 4, pp. 148-159, 1978.



- [Baraloto et al., 2009], Baraloto, C., Paine, T., Patiño, S., Bonal, D., Herault, B., Chave, J., 2009. Fonctionnal trait variation and sampling strategies in species-rich plant communities. *Functional Ecology* In press.
- [Bonal et al. 2000] Bonal, D., Barigah, T.S., Granier, A., Guehl, J.M., 2000. Late-stage canopy tree species with extremely low delta C-13 and high stomatal sensitivity to seasonal soil drought in the tropical rainforest of French Guiana. *Plant Cell and Environment* 23, 445-459.
- [Bonin et al., 2009] Gregory Bonin, Pascale Dubois-Fernandez, Philippe Dreuillet Olivier Ruault du Plessis, Sébastien Angelliaume, Hubert Cantalloube, , Helène Oriot, Colette Coulombeix and the RIM team “the new ONERA multispectral AIRBORNE SAR system in 2009”, Radar Con 2010, Pasadena, May 2009.
- [Bongers et al., 2001] Bongers, F., P. Charles-Dominique, P. M. Forget, and M. Thery, editors. 2001. *Nouragues: dynamics and plant–animal interactions in a Neotropical rainforest*.
- [Boulet & Brunet 1983] Boulet, R. et Brunet, D. (1983), Prospection pédologique en vue de l’implantation des blocs de l’opération CTFT « Forêt Naturelle », Rapport ORSTOM
- [BRIDGE] <http://www.ecofog.gf/BRIDGE/>
- [Brown 1997] Brown, S., Estimating Biomass and Biomass Change of Tropical Forests. FAO, Rome (FAO Forestry Paper 134).
- [Carlos, 2006], Carlos H., 2006. Resampling SRTM 03 data with kriging. *GRASS/OSGeo-News Open Source GIS and Remote Sensing Information*, 4, pp. 21-25, 2006.
- [Chave et al, 2005] Chave, J., Andalo, C., Brown, S., Cairns, M.A., Chambers, J.Q., Eamus, D., Fölster, H., Fromard, F., Higushi, N., Kira, T., Lescure, J.-P., Nelson, B.W., Ogawa, H., Puig, H., Riéra, B., Yamakura, T., 2005. Tree allometry and improved estimation of carbon stocks and balance in tropical forests. *Oecologia* 145, 87-99.
- [Chave et al, 2004] Chave, J., Condit, R., Aguilar, S., Hernandez, A., Lao, S., Perez, R., 2004. Error propagation and scaling for tropical forest biomass estimates. *Philosophical Transactions of the Royal Society of London Series B-Biological Sciences* 359, 409-420.
- [Chave et al, 2003] Chave, J., Condit, R., Lao, S., Caspersen, J.P., Foster, R.B., Hubbel, S.P., 2003. Spatial and temporal variation of biomass in a tropical forest: result from a large census plot in Panama. *J. Ecol.* 91, 240-252.
- [Chave et al, 2009] Chave, J., Coomes, D., Jansen, S., Lewis, S.L., Swenson, N.G., Zanne, A.E., 2009. Towards a worldwide wood economics spectrum. *Ecol. Lett.* 12, 351-366.
- [Chave et al, 2006] Chave, J., Muller-Landau, H.C., Baker, T.R., Easdale, T.A., Ter Steege, H., Webb, C.O., 2006. Regional and phylogenetic variation of wood density across 2456 neotropical tree species. *Ecol. Appl.* 16, 2356-2367.
- [Circe manuel] <http://geodesie.ign.fr/index.php?page=circe>
- [Cloude et al., 2003] Cloude S.R., and K. Papathanassiou, “A three stage inversion process for polarimetric SAR interferometry”, *IEEE Proceedings, Radar, Sonar and Navigation*, vol. 150, issue 03, pp. 125-134, June 2003.
- [de Foresta 1981] de Foresta, H., 1981. Premier temps de la régénération naturelle après exploitation papetière en forêt tropicale humide. ARBOCEL. Guyane française. In, U.S.T.L., Montpellier.





- [Dubois-Fernandez et al., 2009a] P Dubois-Fernandez P, Technical and financial proposal for ESA ESTEC concerning the technical assistance for the deployment of airborne SAR and geophysical measurements during the TropiSAR 2009 experiment, DEMR-TropiSAR-PTF-09-005.1, March 2009
- [Dubois-Fernandez et al., 2009b] P Dubois-Fernandez, T Le Toan, J Chave, “ TropiSAR 2009 Experiment Plan”, TropiSAR-PE-09-V1, June 2009
- [Dubois-Fernandez et al., 2005] Dubois-Fernandez Pascale, Franck Garestier, Isabelle Champion, Philippe Paillou, Final report for ESA study 18501/04/NL/CB, Vegetation characterisation from SAR data, 26/10/05
- [Dubois-Fernandez et al., 2006] Dubois-Fernandez Pascale, Franck Garestier, Isabelle Champion, Xavier Dupuis, Philippe Paillou, “ Forest parameter retrieval from PolInSAR data at L and P band”, PolInSAR2006, Frascati January 2006
- [Dubois-Fernandez et al., 2008] Dubois-Fernandez, P., J.-C. Souyris, and S. Angelliaume F. Garestier. The compact polarimetry alternative for spaceborne SAR at low frequency. *Geoscience and Remote Sensing, IEEE Transactions on*, 46(10):3208–3222, Oct. 2008.
- [Dubois-Fernandez, 2010] P. Dubois-Fernandez, H. Oriot, C. Coulombeix, H. Cantalloube, O. Ruault du Plessis, T. Le Toan, S. Daniel, J. Chave, L. Blanc, M. Davidson, “TropiSAR, a SAR data acquisition campaign in French Guiana”, EUSAR 2010, Aachen, Germany
- [Dubois-Fernandez, 2011] P. Dubois-Fernandez, S. Daniel, A. Arnaubec, T. Le Toan, H. Oriot, J. Chave, L. Blanc, M. Davidson, M. Petit “The TropiSAR Campaign in French Guiana, in-situ & SAR datasets and First PolInSAR Analysis” POLINSAR 2011, Frascati
- [Epron et al. 2006]. Epron, D., A. Bosc, et al. (2006). "Spatial variation of soil respiration across a topographic gradient in a tropical rain forest in French Guiana." *Journal of Tropical Ecology* 22: 565-574.
- [Ferry, 2010] Bruno Ferry<sup>1</sup>, François Morneau<sup>1</sup>, Jean-Daniel Bontemps, Lilian Blanc, Vincent Freycon, "Higher treefall rates on slopes and waterlogged soils result in lower stand biomass and productivity in a tropical rain forest", *Journal of Ecology* Volume 98, Issue 1, pages 106–116, January 2010
- [Frangi et al. 1985] Frangi JL, Lugo AE 1985. Ecosystem dynamics of a subtropical floodplain forest. *Ecol. Monogr.* 55, 351-369.
- [Garestier et al., 2008] Garestier, P.C. Dubois-Fernandez & I. Champion, “Forest Height Inversion Using High Resolution P-Band Pol-InSAR Data”, *IEEE Transactions on Geoscience and Remote Sensing*, vol 46, No. 11, November 2008.
- [Garestier et al., 2010a] Garestier F. and T. Le Toan, 2010, ‘ Forest modelling for height inversion using single baseline InSAR/Pol-InSAR data’, *IEEE Trans. In Geoscience and Remote Sensing*, Vol 48, No 3, 1528-1539, March 2010.
- [Garestier et al., 2010b] Garestier F. and T. Le Toan, 2010, ‘ Estimation of the Backscatter Vertical Profile of a pine forest using single baseline P-band (Pol-) InSAR data’ *IEEE Trans. In Geoscience and Remote Sensing*, Vol 48, No 9, 3340-3348, September 2010.
- [Gourlet-Fleury et al., 2004] Gourlet-Fleury, S., J.-M. Guehl, and O. Laroussinie, editors. 2004. *Ecology and management of a neotropical forest. Lessons drawn from Paracou, a long-term experimental research site in French Guiana.* Elsevier, Paris.



- [Grimaldi & Riéra 2001].. Grimaldi, M. and B. Riera . 2001. Chapter 2: Geography and climate. In F. Bongers (Ed.). *Nouragues: Dynamics and plant-animal interactions in a Neotropical rainforest*, pp. 9–18. Kluwer Academic, Dordrecht, The Netherlands Geography and Climate
- [Hanjsek et al, 2009] Hajnsek, I., F. Kugler, S.-K. Lee, K. P. Papathanassiou, “Tropical-Forest-Parameter Estimation by means of Pol-InSAR: The INDREX II Campaign, IEEE Transactions on Geoscience and Remote Sensing, vol. 47, no. 2, pp. 481 – 493, February 2009
- [Keeratikasikorn et al, 2008], Keeratikasikorn C., Trisirisatayawong I., 2008. Reconstruction of 30m DEM from 90m SRTM DEM with bicubic polynomial interpolation method. *International Archives of the Photogrammetry, Remote Sensing and Spatial Information Sciences*, 37, Part B, pp. 791-794, 2008.
- [Larpin 1989] Larpin, D., 1989. Evolution floristique et structurale d'un recru forestier en Guyane française. *Revue d'Ecologie (Terre et vie)* 44, 209-224.
- [Lawson, 1972], Lawson C.L., 1972. Generation of a triangular grid with application to contour plotting. Tech. Memo. 299, Sect. 914, Jet Propulsion Laboratory, Caltech, Pasadena, California.
- [Le Toan et al, 1992] Le Toan, T., A. Beaudoin, J. Riom, and D. Guyon, 1992, “Relating forest biomass to SAR data”, IEEE Transactions on Geoscience and Remote Sensing, vol. 30, no. 2, pp. 403-411.
- [Le Toan et al., 2010] Le Toan T., S. Quegan, M. Davidson, H. Balzter, P. Paillou, K. Papathanassiou, S. Plummer, S. Saatchi, H. Shugart, L. Ulander : ‘The BIOMASS Mission : Mapping global forest biomass to better understand the terrestrial carbon cycle’, in press, *Remote Sensing of Environment*, October 2010.
- [Marcio et al, 2006], Marcio M., Kuplich T., Storino M., Amaral B., Mendes Jr. J., Lima D., 2006. Modeling small watersheds in Brazilian Amazonia with Shuttle Radar Topographic Mission 90m data. *Computers & Geosciences*, 32, 8, pp. 1169-1181.
- [Mette, 2007] Forest Biomass Estimation from Polarimetric SAR interferometry, PhD dissertation, DLR document
- [Molino & Sabatier 2001] Molino, J. F., and D. Sabatier. 2001. Tree diversity in tropical rain forests: A validation of the intermediate disturbance hypothesis. *Science* 294: 1702-1704.
- [Muller-Landau, 2004] Muller-Landau, H.C., 2004. Interspecific and inter-site variation in wood specific gravity of tropical trees. *Biotropica* 36, 20-32.
- [Nouragues] <http://www.nouragues.cnrs.fr>
- [Oriot et al, 2010] Hélène Oriot, Colette Coulombeix, and Pascale Dubois-Fernandez, “Polarimetric UHF Calibration for SETHI” PIERS 2010, Boston
- [Papathanassiou & Cloude, 2003] Papathanassiou K.P., and S.R. Cloude, “The Effect of Temporal Decorrelation on the Inversion of Forest Parameters from Pol-InSAR Data”, *Proceedings IGARSS'03 (CD-ROM)*, Toulouse, France, 2003
- [Petronelli] Petronelli, personal communication
- [Quegan, 1994] Quegan, S., “A unified algorithm for phase and cross-talk calibration of polarimetric data –Theory and observations,” *IEEE Trans. Geosci. Remote Sensing*, Vol. 32, pp 89-99, 1994.



- [Sabatier et al, 1990] Sabatier, D. et Prévost, M.F. Quelques données sur la composition floristique et la diversité des peuplements forestiers de Guyane française, Bois et Forêts des Tropiques 219, pp. 31-55.
- [Sandberg et al, 2010] G. Sandberg, L. M. H. Ulander, J. E. S. Fransson, J. Holmgren, T. Le Toan, 'L-band versus P-band SAR for biomass retrieval in hemiboreal forest', In press, Remote Sensing of Environment, October 2010.
- [Saatchi et al, 2010] Saatchi, S., Marlier, M., Chazdon, R., Clark, D., and A. Russell, (2010). Impacts of Spatial Variability and Scale on Radar Estimation of Structure and Aboveground Biomass in Tropical Forests, JGR, Biogeosciences, In Review.
- [Raney et al, 1994] Raney, R.K.; Freeman, T.; Hawkins, R.W.; Bamler, R.; , "A plea for radar brightness," Geoscience and Remote Sensing Symposium, 1994. IGARSS '94. Surface and Atmospheric Remote Sensing: Technologies, Data Analysis and Interpretation., International , vol.2, no., pp. 1090- 1092 vol.2, 8-12 Aug. 1994
- [Tebaldini, 2009] Tebaldini « Single and Multipolarimetric SAR tomography of forested areas : a parametric approach », IEEE Trans of GRS, DOI 10.1109/TGRS.2009.2037748,
- [Toriola et al, 1998] Toriola, D., Chareyre, P., Buttler, A., 1998. Distribution of primary forest plant species in a 19-year old secondary forest in French Guiana. J. Trop. Ecol. 14, 323-340.
- [Treuhaft, R et al., 1996] Treuhaft, R.N., S.N. Madsen, M. Moghaddam, and J.J. van Zyl, "Vegetation Characteristics and Underlying Topography from Interferometric Data", Radio Science, vol. 31, pp. 1449-1495, 1996
- [Wiemker, 1996], Wiemker R., 1996. Registration of airborne scanner imagery using Akima local quintic polynomial interpolation. *Second International Airborne Remote Sensing Conference and Exhibition*, San Francisco, California, 24-27 June 1996.
- [Van der Meer 1996] Van Der Meer, P., Bongers, F., 1996. Patterns of tree fall and branch-fall in a tropical rain forest in French Guiana, J. Trop. Ecol. 14, 323-340
- [Van Zyl, 1993] J.J. Van Zyl, "The effect of topography on radar scattering from vegetated areas," IEEE Transactions on, vol. 31, pp. 153-160, Jan 1993.
- [Villard, 2010] L. Villard, P. Borderies and T. Le Toan, "Topography effects on forest radar scattering, consequences on biomass retrieval," in International Geoscience and Remote Sensing Symposium (IGARSS). IEEE, 2010, vol. 20-24.
- [Williamson et al 2010] Williamson, G.B., Wiemann, M.C., 2010. Measuring wood specific gravity... Correctly. Am. J. Bot. 97, 519-524.

## 11. ACKNOWLEDGMENTS

This campaign was realised under joint fundings from ESA, CNES and ONERA and we want to thank Malcolm Davidson, Selma Cherchali and Emmanuel Rosencher for their help and trust.

An acquisition campaign is always an intense and difficult enterprise. The TropiSAR team received great help and welcome from the local people. We want to express our immense gratitude to all, for the constant support we got during the month we were in French Guiana and during the campaign preparation phase.



IRD hosted our computing facilities in a brand new office space, providing the processing team working conditions equivalent to the one they would have had if the campaign had been in Salon de Provence. Particular thanks go to Papa Sonko, Jean-Francois Faure, Marie-Rose Rosianne and Michel Petit.

The Centre Spatial Guyanais was particularly involved in our operation as one of our main forest site, Paracou was next to the launch pad and required special authorisations for overflight in the reserved airspace. Day to day contacts and requests were made by the team to the Security department, under the responsibility of Bernard Chemoul. Thanks to him and his team, in particular Christianne Catherine, Stephane Rousseau.

The CNRS local office with Philippe Gaucher provided invaluable advice and logistic support. Alain Pavé provided interesting insights on the area and Gaelle Fornet helped us in the TropiSAR communication.

Air Guyane provided ground support for the airplane and the radar hardware crew. The kind day to day help was greatly appreciated as it allowed us to work in excellent conditions despite the high temperatures.

Many administrative hurdles had to be resolved and this was possible with the help of the "Prefecture, the Armée de l'Air, the DGAC, the CCI who authorised us to deploy our calibration targets on the airport grounds.

The overall campaign benefited from the large local scientific community involved in studies concerning tropical forests and they were always very supportive and helpful. Trying not to forget any, we want to express our thanks to ONF, CEMAGREF, CIRAD, ONF, Parc National, ESA local office.





## ANNEX A: GEOGRAPHIC AND IMAGE COORDINATES FOR THE REGIONS OF INTEREST

In this annex, a table per site lists for the four corners of each study plots the geographic coordinates, UTM coordinates , altitude, height, and SLC image coordinates.

- PARACOU with respect to the SLC reference image tropi0402, ROI 1 to ROI 16
- ARBOCEL, with respect to the SLC reference image tropi0108 ROI17
- PARACOU with respect to the SLC reference image tropi0506 – New plots  
**Some new plots are not in all images. Therefore, the reference image had to be changed.**
- NOURAGUES with respect to the SLC reference image tropi0201 Petit Plateau
- NOURAGUES with respect to the SLC reference image tropi0201 Grand Plateau
- NOURAGUES with respect to the SLC reference image tropi0303 New plots: Balanfois  
**Some new plots are not in all images. Therefore, the reference image had to be changed.**
- NOURAGUES with respect to the SLC reference image tropi0201 Other new plots

ESA CONTRACT N° 22446/09/NL/CT  
CNES CONTRACT N° 92929 03/08/09



February 2011 V2.1

### PARACOU - reference image: tropi0402

Roi	Corner	UTM coordinate		Altitude	Geographic coordinate		Ellipsoidal height	Radar image coordinate	
		X	Y		Lat	Long		Azimuth	Range
1	SW	285138	582861	7.35000	5.270156	-52.938687	-26.891	1854	1400
	SE	285373	582924	8.43700	5.270732	-52.936569	-25.808	1931	1245
	NE	285307	583165	10.2040	5.272909	-52.937171	-24.038	2115	1312
	NW	285072	583102	18.9660	5.272333	-52.939289	-15.272	2038	1462
2	SW	285075	582532	8.00000	5.267179	-52.939246	-26.242	1586	1410
	SE	285316	582596	4.67800	5.267765	-52.937074	-29.568	1664	1254
	NE	285251	582837	28.2920	5.269942	-52.937667	-5.951	1848	1305
	NW	285010	582774	7.50200	5.269365	-52.939839	-26.737	1770	1481
3	SW	285395	582513	16.6800	5.267016	-52.936359	-17.568	1607	1184
	SE	285636	582577	5.15600	5.267602	-52.934187	-29.096	1686	1041
	NE	285574	582818	14.6460	5.269779	-52.934753	-19.603	1870	1096
	NW	285333	582754	6.69800	5.269194	-52.936925	-27.547	1792	1256
4	SW	285877	582813	19.2430	5.269742	-52.932020	-15.012	1901	899
	SE	286116	582878	30.0710	5.270337	-52.929866	-4.188	1980	751
	NE	286050	583120	33.5460	5.272523	-52.930468	-0.710	2165	809
	NW	285812	583055	20.7140	5.271929	-52.932613	-13.538	2086	961
5	SW	286165	582889	33.5890	5.270438	-52.929425	-0.671	1995	720
	SE	286404	582958	31.8040	5.271068	-52.927271	-2.460	2077	590
	NE	286337	583200	11.4800	5.273254	-52.927882	-22.781	2262	665
	NW	286099	583131	17.2800	5.272624	-52.930027	-16.977	2179	793
6	SW	286457	582936	24.1330	5.270871	-52.926792	-10.132	2066	566
	SE	286696	582995	29.5340	5.271411	-52.924638	-4.735	2140	438
	NE	286634	583239	10.1970	5.273615	-52.925204	-24.069	2327	506
	NW	286395	583180	11.4760	5.273075	-52.927358	-22.786	2252	630



February 2011 V2.1

**PARACOU - reference image: tropi0402**

Roi	Corner	UTM coordinate		Altitude	Geographic coordinate		Ellipsoidal height	Radar image coordinate	
		X	Y		Lat	Long		Azimuth	Range
7	SW	286030	582476	18.0350	5.266700	-52.930631	-16.225	1651	777
	SE	286269	582543	27.9760	5.267312	-52.928477	-6.288	1732	636
	NE	286203	582780	16.7540	5.269453	-52.929079	-17.507	1912	703
	NW	285963	582714	9.80200	5.268850	-52.931242	-24.455	1832	845
8	SW	285954	582028	21.9520	5.262647	-52.931304	-12.309	1286	781
	SE	286193	582097	11.6870	5.263278	-52.929150	-22.578	1368	656
	NE	286130	582337	29.6360	5.265446	-52.929725	-4.626	1552	697
	NW	285891	582268	20.5080	5.264815	-52.931879	-13.750	1470	841
9	SW	286213	581497	22.3170	5.257853	-52.928953	-11.952	894	587
	SE	286452	581565	27.1410	5.258475	-52.926799	-7.132	975	460
	NE	286385	581806	35.5680	5.260652	-52.927410	1.298	1159	507
	NW	286147	581738	20.4890	5.260030	-52.929555	-13.777	1078	645
10	SW	286509	581558	36.7760	5.258413	-52.926285	2.502	976	422
	SE	286749	581620	13.9910	5.258980	-52.924122	-20.287	1053	327
	NE	286687	581863	26.0660	5.261176	-52.924688	-8.209	1239	364
	NW	286447	581801	27.9230	5.260608	-52.926851	-6.348	1162	480
11	SW	286154	581174	13.8000	5.254931	-52.929476	-20.470	630	601
	SE	286394	581240	15.2990	5.255535	-52.927313	-18.975	710	476
	NE	286330	581479	23.1850	5.257694	-52.927897	-11.086	893	521
	NW	286089	581412	29.3880	5.257081	-52.930069	-4.879	812	644
12	SW	286445	581226	11.3030	5.255410	-52.926853	-22.972	705	452
	SE	286685	581294	9.42000	5.256031	-52.924690	-24.859	786	339
	NE	286622	581536	15.6340	5.258217	-52.925265	-18.642	972	381
	NW	286383	581469	16.3250	5.257605	-52.927419	-17.947	891	498



February 2011 V2.1

**PARACOU - reference image: tropi0402**

Roi	Corner	UTM coordinate		Altitude	Geographic coordinate		Ellipsoidal height	Radar image coordinate	
		X	Y		Lat	Long		Azimuth	Range
13	SW	285412	583021	23.4400	5.271610	-52.936220	-10.805	2013	1217
	SE	285646	583095	25.2890	5.272286	-52.934111	-8.960	2099	1067
	NE	285571	583333	10.9890	5.274435	-52.934795	-23.257	2279	1150
	NW	285337	583260	7.66600	5.273769	-52.936903	-26.576	2194	1303
14	SW	285787	583145	12.3080	5.272742	-52.932841	-21.943	2155	991
	SE	286024	583216	38.5950	5.273390	-52.930705	4.340	2238	829
	NE	285953	583454	22.8810	5.275540	-52.931352	-11.372	2419	907
	NW	285716	583384	14.9000	5.274900	-52.933488	-19.349	2336	1057
15	SW	286338	583506	17.0620	5.276021	-52.927881	-17.197	2505	685
	SE	286575	583578	22.5040	5.276679	-52.925746	-11.759	2589	553
	NE	286498	583813	16.3240	5.278801	-52.926447	-17.936	2767	620
	NW	286261	583742	31.5220	5.278153	-52.928583	-2.734	2684	738
16	SW	285201	581199	4.98600	5.255131	-52.938072	-29.266	540	1196
	SE	285680	581343	7.75900	5.256446	-52.933756	-26.501	710	899
	NE	285536	581821	4.84300	5.260764	-52.935068	-29.412	1073	1035
	NW	285056	581678	13.1800	5.259457	-52.939393	-21.067	904	1335

**ARBOCEL - reference image: tropi0108**

Roi	Corner	UTM coordinate		Altitude	Geographic coordinate		Ellipsoidal height	Radar image coordinate	
		X	Y		Lat	Long		Azimuth	Range
17	SW	272885	586449	46.00	5.30223948	-53.04930497	12.023	2727	457
	SE	273017	586664	46.00	5.30418718	-53.04812083	12.022	2929	449
	NE	272806	586792	46.00	5.30533809	-53.05002773	12.027	2939	585
	NW	272673	586578	46.00	5.30339939	-53.05122091	12.028	2737	594





February 2011 V2.1

**PARACOU: Other plots - reference image: tropi0506**

Roi	Corner	UTM coordinate		Altitude	Geographic coordinate		Ellipsoidal height	Radar image coordinate	
		X	Y		Lat	Long		Azimuth	Range
Plantation of <i>Pinus caribaea</i> P1	SW	287397	589925	15.0	5.334087	-52.918509	-19.229	77289	615
	SE	287461	589896	15.0	5.333827	-52.917931	-19.230	7713	577
	NE	287491	589958	15.0	5.334389	-52.917662	-19.230	7766	565
	NW	287428	589988	15.0	5.334658	-52.918231	-19.229	7782	602
Plantation of <i>Pinus caribaea</i> P2	SW	287232	589729	17.5	5.332311	-52.919992	-16.728	7554	690
	SE	287296	589701	17.5	5.332059	-52.919414	-16.729	7539	651
	NE	287326	589762	17.5	5.332612	-52.919145	-16.729	7591	639
	NW	287262	589793	17.5	5.332890	-52.919723	-16.728	7608	678
Plantation of <i>Cocos nucifera</i>	SW	286226	587669	21.0	5.313657	-52.929008	-13.228	5801	1125
	SE	286275	587661	21.0	5.313586	-52.928566	-13.229	5800	1092
	NE	286283	587711	21.0	5.314038	-52.928495	-13.229	5841	1091
	NW	286233	587718	21.0	5.314100	-52.928947	-13.228	5841	1125
Secondary forest	SW	286079	587805	25.5	5.314883	-52.930338	-8.725	5892	1233
	SE	286119	587797	25.5	5.314811	-52.929977	-8.725	5890	1205
	NE	286132	587864	25.5	5.315418	-52.929862	-8.725	5945	1203
	NW	286091	587872	25.5	5.315489	-52.930232	-8.724	5947	1231
Seasonally flooded forests P1	SW	-	-	-	-	-	-	-	-
	SE	284145	583825	27.0	5.278843	-52.947670	-7.217	2506	2224
	NE	-	-	-	-	-	-	-	-
	NW	284141	583823	27.0	5.278825	-52.947706	-7.217	2504	2227
Seasonally flooded forests P2	SW	-	-	-	-	-	-	-	-
	SE	283763	584059	22.0	5.280948	-52.951122	-12.209	2648	2555
	NE	-	-	-	-	-	-	-	-
	NW	283762	584058	22.0	5.280939	-52.951131	-12.209	2647	2556



February 2011 V2.1

**NOURAGUES: Petit Plateau - reference image: tropi0201**

Roi	Corner	UTM coordinate		Altitude	Geographic coordinate		Ellipsoidal height	Radar image coordinate	
		X	Y		Lat	Long		Azimuth	Range
<b>PPE20</b>	SW	312959	451609	117.610	4.084006	-52.684899	83.523	1127	201
	SE	313050	451566	117.830	4.083619	-52.684078	83.742	1162	245
	NE	313098	451648	110.910	4.084362	-52.683648	76.821	1097	276
	NW	313010	451688	113.300	4.084722	-52.684441	79.212	1064	230
<b>PPF20</b>	SW	313050	451566	117.830	4.083619	-52.684078	83.742	1162	245
	SE	313142	451523	114.960	4.083232	-52.683249	80.872	1198	294
	NE	313187	451608	108.140	4.084002	-52.682845	74.050	1130	324
	NW	313098	451648	110.910	4.084362	-52.683648	76.821	1097	276
<b>PPG20</b>	SW	313142	451523	114.960	4.083232	-52.683249	80.872	1198	294
	SE	313233	451480	119.970	4.082845	-52.682429	85.881	1234	337
	NE	313275	451567	112.850	4.083633	-52.682052	78.759	1164	366
	NW	313187	451608	108.140	4.084002	-52.682845	74.050	1130	324
<b>PPH20</b>	SW	313233	451480	119.970	4.082845	-52.682429	85.881	1234	337
	SE	313325	451437	125.840	4.082458	-52.681599	91.750	1269	381
	NE	313364	451528	116.340	4.083282	-52.681250	82.249	1197	411
	NW	313275	451568	112.690	4.083642	-52.682052	78.599	1164	366
<b>PPE21</b>	SW	312908	451531	108.660	4.083300	-52.685357	74.575	1189	184
	SE	313003	451485	117.800	4.082886	-52.684500	83.714	1227	221
	NE	313050	451566	117.830	4.083619	-52.684078	83.742	1162	245
	NW	312959	451609	117.610	4.084006	-52.684899	83.523	1127	201
<b>PPF21</b>	SW	313003	451485	117.800	4.082886	-52.684500	83.714	1227	221
	SE	313097	451439	113.660	4.082472	-52.683653	79.573	1265	271
	NE	313142	451523	114.960	4.083232	-52.683249	80.872	1198	294
	NW	313050	451566	117.830	4.083619	-52.684078	83.742	1162	245

**NOURAGUES: Petit Plateau - reference image: tropi0201**

Roi	Corner	UTM coordinate		Altitude	Geographic coordinate		Ellipsoidal height	Radar image coordinate	
		X	Y		Lat	Long		Azimuth	Range
PPG21	SW	313097	451439	113.660	4.082472	-52.683653	79.573	1265	271
	SE	313191	451393	114.820	4.082058	-52.682805	80.732	1303	318
	NE	313233	451480	119.970	4.082845	-52.682429	85.881	1234	337
	NW	313142	451523	114.960	4.083232	-52.683249	80.872	1198	294
PPH21	SW	313191	451393	114.820	4.082058	-52.682805	80.732	1303	318
	SE	313285	451347	126.940	4.081643	-52.681958	92.851	1341	357
	NE	313325	451437	125.840	4.082458	-52.681599	91.750	1269	381
	NW	313233	451480	119.970	4.082845	-52.682429	85.881	1234	337
PPE22	SW	312858	451452	102.210	4.082585	-52.685805	68.126	1251	165
	SE	312955	451403	116.640	4.082144	-52.684931	82.555	1292	198
	NE	313003	451485	117.800	4.082886	-52.684500	83.714	1227	221
	NW	312908	451531	108.660	4.083300	-52.685357	74.575	1189	184
PPF22	SW	312955	451403	116.640	4.082144	-52.684931	82.555	1292	198
	SE	313052	451355	112.300	4.081711	-52.684056	78.214	1332	249
	NE	313097	451439	113.660	4.082472	-52.683653	79.573	1265	271
	NW	313003	451485	117.800	4.082886	-52.684500	83.714	1227	221
PPG22	SW	313052	451355	112.300	4.081711	-52.684056	78.214	1332	249
	SE	313149	451306	111.770	4.081270	-52.683182	77.683	1372	298
	NE	313191	451393	114.820	4.082058	-52.682805	80.732	1303	318
	NW	313097	451439	113.660	4.082472	-52.683653	79.573	1265	271
PPH22	SW	313149	451306	111.770	4.081270	-52.683182	77.683	1372	298
	SE	313246	451257	129.290	4.080829	-52.682308	95.203	1413	334
	NE	313285	451347	126.940	4.081643	-52.681958	92.851	1341	357
	NW	313191	451393	114.820	4.082058	-52.682805	80.732	1303	318



February 2011 V2.1

**NOURAGUES: Grand Plateau - reference image: tropi0201**

Roi	Corner	UTM coordinate		Altitude	Geographic coordinate		Ellipsoidal height	Radar image coordinate	
		X	Y		Lat	Long		Azimuth	Range
GPM10	SW	314050	452168	86.2400	4.089082	-52.675084	52.134	691	848
	SE	314140	452113	100.870	4.088586	-52.674273	66.763	737	894
	NE	314182	452192	95.9200	4.089302	-52.673896	61.812	674	926
	NW	314093	452247	80.4900	4.089797	-52.674698	46.382	628	881
GPM11	SW	314007	452088	92.5400	4.088358	-52.675470	58.435	755	815
	SE	314097	452035	104.700	4.087880	-52.674658	70.594	799	863
	NE	314140	452113	100.870	4.088586	-52.674273	66.763	737	894
	NW	314050	452168	86.2400	4.089082	-52.675084	52.134	691	848
GPM12	SW	313965	452008	95.8100	4.087634	-52.675847	61.706	819	785
	SE	314055	451956	105.170	4.087165	-52.675035	71.065	862	835
	NE	314097	452035	104.700	4.087880	-52.674658	70.594	799	863
	NW	314007	452088	92.5400	4.088358	-52.675470	58.435	755	815
GPM13	SW	313922	451928	93.9400	4.086909	-52.676232	59.837	882	759
	SE	314012	451877	106.060	4.086450	-52.675421	71.957	925	806
	NE	314055	451956	105.170	4.087165	-52.675035	71.065	862	835
	NW	313965	452008	95.8100	4.087634	-52.675847	61.706	819	786
GPM14	SW	313879	451849	94.6900	4.086194	-52.676618	60.589	945	731
	SE	313970	451799	109.550	4.085744	-52.675798	75.448	987	776
	NE	314012	451877	106.060	4.086450	-52.675421	71.957	925	806
	NW	313922	451928	93.9400	4.086909	-52.676232	59.837	882	759
GPM15	SW	313836	451769	95.4800	4.085470	-52.677004	61.380	1009	704
	SE	313927	451720	107.790	4.085029	-52.676183	73.689	1050	750
	NE	313970	451799	109.550	4.085744	-52.675798	75.448	987	776
	NW	313879	451849	94.6900	4.086194	-52.676618	60.589	945	731





February 2011 V2.1

**NOURAGUES: Grand Plateau - reference image: tropi0201**

Roi	Corner	UTM coordinate		Altitude	Geographic coordinate		Ellipsoidal height	Radar image coordinate	
		X	Y		Lat	Long		Azimuth	Range
GPM16	SW	313793	451689	97.7500	4.084746	-52.677390	63.651	1073	675
	SE	313885	451641	111.260	4.084313	-52.676560	77.161	1112	720
	NE	313927	451720	107.790	4.085029	-52.676183	73.689	1050	750
	NW	313836	451769	95.4800	4.085470	-52.677004	61.380	1009	704
GPM17	SW	313751	451609	94.8000	4.084021	-52.677766	60.703	1134	651
	SE	313842	451563	101.050	4.083607	-52.676946	66.952	1175	701
	NE	313885	451641	111.260	4.084313	-52.676560	77.161	1112	720
	NW	313793	451689	97.7500	4.084746	-52.677390	63.651	1073	675
GPM18	SW	313708	451529	83.3800	4.083297	-52.678152	49.284	1200	634
	SE	313800	451484	95.2200	4.082892	-52.677323	61.123	1238	679
	NE	313842	451563	101.050	4.083607	-52.676946	66.952	1175	701
	NW	313751	451609	94.8000	4.084021	-52.677766	60.703	1137	651
GPM19	SW	313622	451370	71.4500	4.081858	-52.678924	37.356	1327	592
	SE	313715	451327	84.7100	4.081471	-52.678085	50.616	1363	635
	NE	313800	451484	95.2200	4.082892	-52.677323	61.123	1238	679
	NW	313708	451529	83.3800	4.083297	-52.678152	49.284	1200	634



February 2011 V2.1

**NOURAGUES: Balanfois - reference image: tropi0303**

Roi	Corner	UTM coordinate		Altitude	Geographic coordinate		Ellipsoidal height	Radar image coordinate	
		X	Y		Lat	Long		Azimuth	Range
NB 1	SW	312518	449721	169.420	4.066925	-52.688835	135.356	2663	407
	SE	312627	449718	170.860	4.066900	-52.687853	136.795	2666	469
	NE	312618	449821	170.810	4.067831	-52.687936	136.744	2584	464
	NW	312524	449823	169.750	4.067848	-52.688782	135.685	2581	411
NB 2	SW	312524	449823	169.750	4.067848	-52.688782	135.685	2581	411
	SE	312618	449821	170.810	4.067831	-52.687936	136.744	2584	464
	NE	312624	449918	170.010	4.068709	-52.687884	135.943	2506	469
	NW	312522	449920	168.660	4.068725	-52.688802	134.594	2503	411

**NOURAGUES: Other plots - reference image: tropi0201**

Roi	Corner	UTM coordinate		Altitude	Geographic coordinate		Ellipsoidal height	Radar image coordinate	
		X	Y		Lat	Long		Azimuth	Range
Lhor plot	SW	313664	447037	83.2900	4.042675	-52.678464	49.236	4807	567
	SE	313764	447042	74.4400	4.042723	-52.677564	40.385	4804	633
	NE	313754	447124	91.0000	4.043464	-52.677655	56.944	4738	614
	NW	313664	447118	95.5000	4.043408	-52.678466	61.445	4742	558
New Plot	SW	313830	447438	145.240	4.046305	-52.676977	111.180	4487	619
	SE	313931	447426	143.770	4.046198	-52.676067	109.708	4498	682
	NE	313931	447535	146.470	4.047184	-52.676069	112.407	4411	681
	NW	313838	447528	142.780	4.047119	-52.676907	108.719	4415	627
Parare	SW	313127	446504	63.2600	4.037846	-52.683290	29.218	5229	292
	SE	313327	446504	90.6200	4.037849	-52.681489	56.576	5231	370
	NE	313327	446804	63.9800	4.040562	-52.681495	29.933	4990	395
	NW	313127	446804	106.890	4.040558	-52.683296	72.845	4988	256



## ANNEX B: TROPISAR SAR DATA FORMAT

### 1. VERSION OF THE DOCUMENT

Version	Ver	Modification	Date of delivery
0	V1.	Initial version	30/03/2010
1	V1.	Modification of the incidence angle calculation	07/10/2010
2	V1.	Integration of the geocoded products	19/11/2010

### 2. THE DIFFERENT DATA LEVELS

#### 2.1. LEVEL 1 data: SLC

Level 1 format is in the nominal-slant-range geometry and values are radar cross-section values (m<sup>2</sup>), not compensated for the incident angle. The data set contains:

- 4 SLC (single look complex) images (HH, HV, VH and VV in 4 data files) (columns=increasing range, lines=along track), calibrated, in Sigma (RCS) value, associated with a rectangular weighting window:  
**tropi0104\_Pcons\_Hh\_slc.dat, tropi0104\_Pcons\_Hv\_slc.dat, tropi0104\_Pcons\_Vh\_slc.dat, tropi0104\_Pcons\_Vv\_slc.dat**
- 4 header files; The header contains also information about the image format, its geometry (the nominal trajectory, the squint angle and the pixel dimensions), its resolution. It also contains information such as weighting and **surface of resolution**:  
**tropi0104\_Pcons\_Hh\_slc.ent, tropi0104\_Pcons\_Hv\_slc.ent, tropi0104\_Pcons\_Vh\_slc.ent, tropi0104\_Pcons\_Vv\_slc.ent**
- 1 ascii file containing the necessary information allowing to precisely geo-locate each of the image pixel. It consists in a table with 5 columns: i,j,h,lat, long, where i,j are the SLC image coordinates, h the altitude of the pixel, lat, long the geographical coordinates. The increment in the i, j, h are computed to maintain the localisation error under a level provided by the operator.  
**tropi0104\_Pcons\_slc.grille:**



- 1 ROI file in an ENVI format, which can be read directly from ENVI and identifies the different regions of interest where in-situ measurements are available; **tropi0104\_Pcons\_slc.roi**
- When applicable, a file containing the altitude of ambiguity image of the same size as the referenceSLC data. The level 1 SLC interferometric dataset images are computed with a common nominal trajectory, and with the same squint angle. **tropi0402\_0403\_Ha.1, tropi0402\_0403\_Ha.inf**

## 2.2. LEVEL 1-B: SLC projected to a master geometry

Level 1-B format is corresponding to the projection of an SLC image (computed in its own intrinsic geometry) into a reference geometry associated with the master image for tomographic and PolInSAR study. The data set contains:

- 4 files containing the complex images (HH HV VH VV each in one file) in its native slant range geometry  
**tropi0403\_Pprop\_Hh\_slc.dat, tropi0403\_Pprop\_Hv\_slc.dat, tropi0403\_Pprop\_Vh\_slc.dat, tropi0403\_Pprop\_Vv\_slc.dat**
- 4 header files; The header contains also information about the image format, its geometry (the processing trajectory, the squint angle and the pixel dimensions), its resolution. **tropi0403\_Pprop\_Hh\_slc.ent, tropi0403\_Pprop\_Hv\_slc.ent, tropi0403\_Pprop\_Vh\_slc.ent, tropi0403\_Pprop\_Vv\_slc.ent**
- 1 ascii file containing the necessary information allowing to precisely locate on a map each of the image pixel. It consists in a table with 5 columns: i,j,h,lat, long, where i,j are the SLC image coordinates, h the altitude of the pixel, lat, long the geographical coordinates. The increment in the i, j, h are computed to maintain the localisation error under a level provided by the operator.  
**tropi0403\_Pprop\_slc.grille**
- 1 ROI file in an ENVI format, which can be read directly from ENVI and identifies the different region of interest where the ground measurements are available; **tropi0403\_Pprop\_slc.roi**

The data set of these data projected in the reference master geometry contains:

- 4 files containing the complex images (HH HV VH VV each in one file) in the reference master slant range geometry **tropi0403\_Pproj\_Hh\_slc.dat, tropi0403\_Pproj\_Hv\_slc.dat, tropi0403\_Pproj\_Vh\_slc.dat, tropi0403\_Pproj\_Vv\_slc.dat**
- 4 header files; The header contains information about the reference image, its geometry (the nominal trajectory, the squint angle and the pixel dimensions), its resolution. Note that it is simply a copy of the header of the reference master image. The information concerning the flight altitude, etc... of the trop0403 image can be found in **tropi0403\_Pprop\_Hh\_slc.ent, tropi0403\_Pproj\_Hh\_slc.ent, tropi0403\_Pproj\_Hv\_slc.ent, tropi0403\_Pproj\_Vh\_slc.ent, tropi0403\_Pproj\_Vv\_slc.ent**





- There is no “grille” file associated with this image as it is the same geometry as the reference image (tropi0402 in the Paracou case)
- When applicable, a file containing the altitude of ambiguity image of the same size as the referenceSLC data The level 1 SLC interferometric dataset images are computed with a common nominal trajectory, and with the same squint angle  
**tropi0402cons\_0403proj\_traj0403.1,tropi0402cons\_0403proj\_traj0403inf**
- 2 trajectories: the reference trajectory and the image trajectory:  
**tropi0402\_Pcons\_slc.trj, tropi0403\_Pprop\_slc.trj**

### 2.3. LEVEL 1-C: Ground projected images

Level 1-C format is in a ground projected geometry (WGS84), compensated for incident angle (Sigma0) on a square grid. This data set contains:

- 4 files containing the float images (HH HV VH VV each in one file)  
**tropi0402\_Pcons\_Hh\_proj\_wgs84.dat,**  
**tropi0402\_Pcons\_Hv\_proj\_wgs84.dat,**  
**tropi0402\_Pcons\_Vh\_proj\_wgs84.dat,**  
**tropi0402\_Pcons\_Vv\_proj\_wgs84.dat**
- 4 header files containing information as format (number of lines and columns, type of data) projection (center, orientation, geoïd, grid size), resolution, incident angle, aspect angle etc. **tropi0402\_Pcons\_Hh\_proj\_wgs84.ent,**  
**tropi0402\_Pcons\_Hv\_proj\_wgs84.ent,**  
**tropi0402\_Pcons\_Vh\_proj\_wgs84.ent, tropi0402\_Pcons\_Vv\_proj\_wgs84.ent**
- Projection are in WGS84.

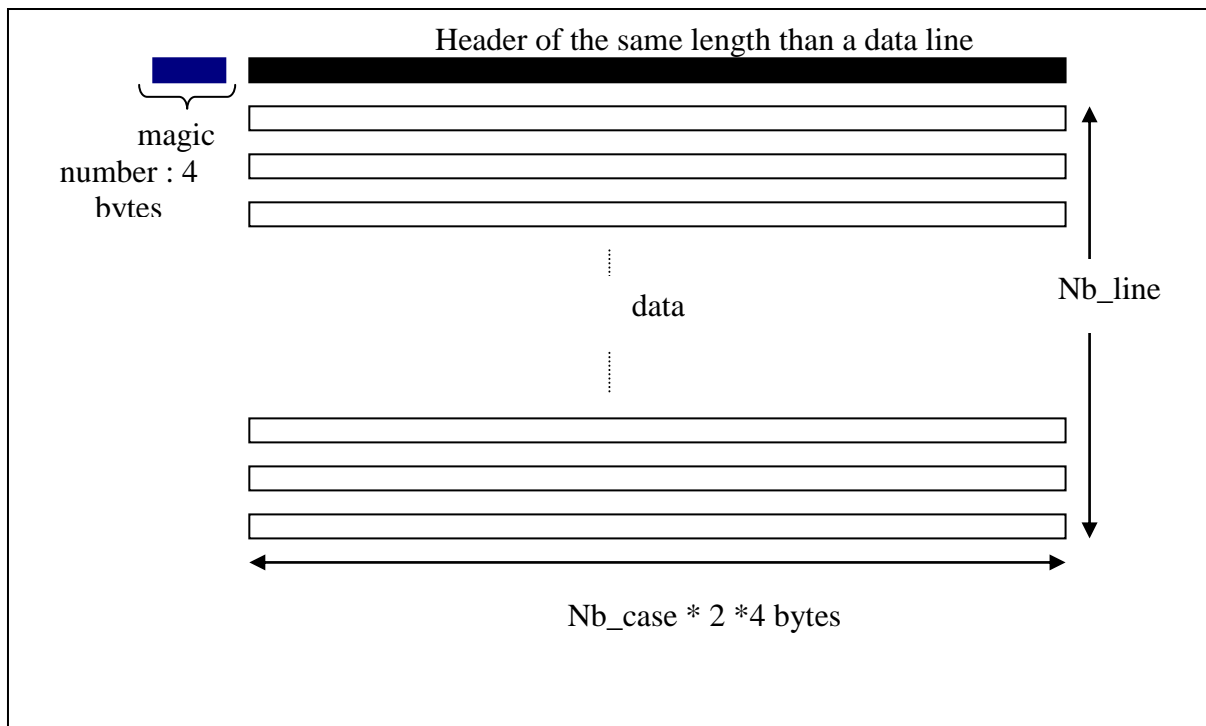
The images are projected in a WGS84 UTM zone 22 grid with 1m pixel spacing. The format is unsigned short integer and the coded value corresponds to Sigma0 in linear format (amplitude). The header provides the UTM coordinates of the origin point.

## 3. MORE ABOUT THE SLC DATA

### 3.1. The SLC data format

The SLC file is composed of :

- A magic number to check the bit-order (little or big endian) coded as a long integer:  
33554433
- A header line with a size of “Nb\_case” coded in complex
- The data coded in complex.



### 3.2. IDL code to read a SLC file

```

Openr,1,'file_name.dat'
Nbcas=4000 & Nbligne= 7570 (from .ent file)
; The header line is composed of the magic number (4 bytes) followed by
;      Nbcas*4*2 bytes
;The data is composed of Nbligne lines, each composed of Nbcas
;      complex numbers, coded on 2*4 bytes.
header=bytarr(4+Nbcas*4*2) & readu,1,header
Data = complexarr(Nbcas,Nbligne) & readu,1,data
Close,1

```

### 3.3. The header file (\*.ent)

In the following, the header file is printed in blue and the explanation in black. The information outlined in red is essential for the analysis.

```

#      [fichier en-tete produit par img_to_ramses version 3610]
# Nom du look :
Look.dat=      tropi0402Cor3_UHF_Hh_slc.dat
# Structure du fichier et codage des pixels :
# 4 octets precedent la premiere ligne : ils correspondent a un nombre magique [
I4= 33554433]

```

Magic number indicates the code as big-endian or small-endian

```

# [dans ordre LSBfirst = big-endian]
Format_valeurs_look=      cmplx_real_4

```



The data are coded in “complex single precision” [real part, imaginary part, real part, imaginary part ...]

*Nb case par ligne look= 5800*

number of pixels along the slant range axis

*Nb\_ligne\_look= 8895 + 1 ligne en-tete en binaire (entiers 16 bit)*

number of lines along the azimuth axis ...be careful, the “+1” corresponds to the header line!

*Espacement\_entre\_pixel= 0.000000 m*

Obsolete; was used in a previous format

*Intercale\_radial\_look= 1.000000 m [radial]*

Pixel size along the slant range axis

*Intercale\_proj\_look= 1.414214 m [projete]*

Pixel size along the slant range axis, projected on the ground

$\text{Intercale\_proj\_look} = \text{Intercale\_radial\_look} / \sin(\text{mean\_incidence\_angle})$

*Interligne\_azimut\_look= 1.245000 m [0.009830 s x 126.648340 m/s] [valeur constante]*

Pixel size along the azimuth axis. It is constant in the image.

*Vitesse\_moyenne= 126.648340 m/s*

Average Aircraft velocity

*Espacement\_temporel= 0.009830 s [valeur moyenne]*

Obsolete

*Frequence\_image= 101.725574 Hz [valeur moyenne]*

Obsolete

*Longueur\_signal= 270038 rampes*

*Frequence\_recurrence\_signal= 2500.000000 Hz*

Pulse repetition frequency

*# Caracteristiques radar et geometriques du look :*

*Config= TROPISAR\_UHFHaut\_recalHO2*

Name of the waveform

*Canal= tot4*

Name of the channel with tot1=Vv, tot2=Vh, tot3=Hv, tot4=Hh

*Bande\_traitee= 125.037520 MHz*

Processed radar Bandwidth

*Frequence\_distance= 397.500000 MHz*

Center frequency

*Frequence\_doppler= 0.000000 Hz [-90.000000 degre dans le plan slant]  
[-89.960594 degre dans le plan horizontal]*

Center doppler frequency

*Bande\_de\_base= non*

*Angle\_derive= -6.198338 degres*

Yaw angle (associated with the acquisition)

*Distance\_radar\_1ere\_case= 3800.000000 m*

Near range distance

*Hauteur\_radar\_sol\_moyenne= 4014.921748 m [Altitude capteur= 3905.963245 m]*



**This height is referenced with respect to the Clark 80 ellipsoid (different than the IAG GRS80 associated with the WGS84 system)**

*Hauteur.source=*           *fixe*  
*Depression=*               *45.0000000 degrees*  
*Route\_nominale=*         *8.058066 degrees*  
*Pente\_nominale=*         *-0.052536 degrees*  
*Angle\_gite=*               *0.895814 degrees*  
*Angle\_assiette=*         *6.116899 degrees*

Information about the trajectory and the aircraft attitude

*# Origine des donnees trajectographiques :*  
*#Trajecto.source=*         *indeterminee*  
*#Hauteur.source=*         *indeterminee*  
*# [voir le fichier de compte-rendu tropi0402\_UHF\_IGI\_BL\_CONS.trc de la trajectoire tropi0402\_UHF\_IGI\_BL\_CONS.traj utilisee pour le calcul]*  
*# [ATTENTION : l'info Latitude/Longitude ci-dessous n'est pas utilisable sans le fichier trajectoire tropi0402\_UHFhaut\_T4\_CONS\_slc.trj associe a cette image]*  
*Latitude\_origine=*         *5.229619 degrees*  
*Longitude\_origine=*       *-52.906471 degrees*  
*#Heure\_origine=*           *non documente*

Information sur la trajectoire utilisée

*# Parametres nominaux de Qualite Image :*  
*# Attention, les rÃ©solutions non apodisees sont en fait des frequences de coupure*  
*Resol\_dist\_rad=*           *1.198810 m [non apodisee, non projete]*  
*Resol\_dist\_proj=*         *1.695373 m [non apodisee, projete]*  
*Resol\_dopp=*               *1.500000 m [non apodisee]*  
*Apodisation\_distance=*   *rectangulaire*  
*Apodisation\_doppler=*    *rectangulaire*  
*Resol\_dist\_rad\_apod=*     *1.062017 m [apodisee, non projete]*  
*Resol\_dist\_proj\_apod=*    *1.501919 m [apodisee, projete]*  
*Resol\_dopp\_apod=*         *1.328839 m [apodisee]*  
*Surface\_resolution=*       *2.088350 mÂ²*

The resolution surface is important to compute the sigma0 values.

*Date\_calcul=*             *Fri Feb 19 2010*

### 3.4. Computing the incidence angle

The incidence angle for the pixel (i,j) can be computed from the following equation:

$$\theta = \cos^{-1}(\text{hauteur\_radar\_sol\_moyenne}/(\text{dis tance\_radar\_lere\_case} + i * \text{int ercase\_radial\_look}))$$

### 3.5. Computing Sigma0

The data in is radar cross section. In order to transform the data in Sigma0, one must use the following equation:





$$\sigma_0 = 10 \cdot \log_{10} \left( \frac{1}{N_{ROI}} \sum (x^2 + y^2) \sin \theta / \text{Surface\_resolution} \right) \text{ dB}$$

### 3.6. Reading the file .grille

#### Transforming pixel position to latitude and longitude

Being able to link precisely one pixel on the image to one geographic location is essential. So is the reverse. In order to provide this correspondence independently of the altitude of the point (which we do not know precisely as we do not have a precise DEM), we provide with the each SAR SLC dataset a file providing a transformation grid, called “\*.grille”. The grid file allows to link a position in the image (x,y) associated with a height to a precise latitude and longitude. It can also be used to associate an image position and a height to a geographic position.

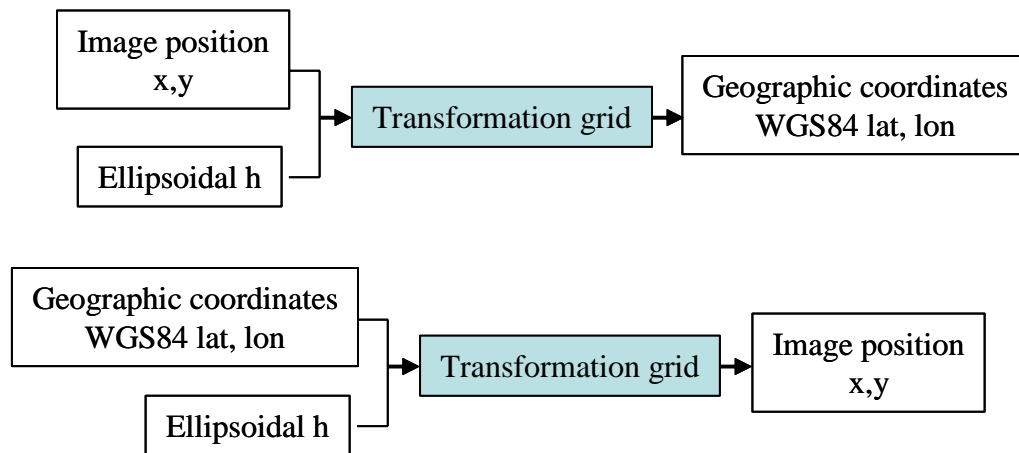


Table 3-1: Geocoding process

This transformation grid file is a text file. The file starts with a short description indicating the relevant reference system, the desired accuracy. For this project, we have chosen 1.5m as accuracy. This value was used to compute the maximum step size in the three dimensions, range, azimuth and height such that the error resulting from a simple linear interpolation between the grid points will create an error below the requested accuracy. The first lines describe also the range of altitude as well as the number of steps in the line dimension (29 in the range direction), in the azimuth direction (129) in the altitude direction (58). The file contains then 29x129x58 lines listing x,y,h,lon,lat where x,y are the image pixel position in range and azimuth, h is the ellipsoidal height with respect to the GRS80 ellipsoid, and lon, lat are the longitude and latitude (E, N) in WGS84 system.

% Grille de georeferencement de l image tropi0402\_Pcons\_Hh\_slc.1 calculee pour une precision de 1.500000 m entre alt = - 103.758803 m et alt = 301.638805 m

% format : ligne colonne altitude longitude latitude (longitude = latitude=0 si pas de donnee )

% Les coordonnees geographiques sont exprimees en WGS84, les altitudes sont donnees par rapport a l'ellipsoide de GRS

80

nb\_lig 29  
nb\_col 129



nb\_alt 58

10 0 -103.7588 -52.9161292218770 5.2460086137288

10 0 -103.5015 -52.9161376843845 5.2460097385163

...

Table 3-2: beginning of a transformation grid file (grille)

In order to use the grid, one way is to identify the two height levels framing the desired height. On each height layer, the desired localisation information is computed via a linear interpolation and a final interpolation is performed in the height direction to compute the localisation information.

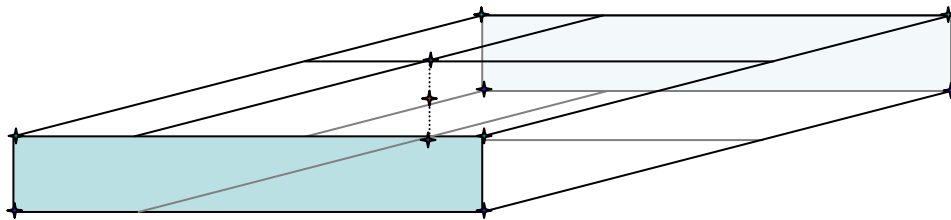
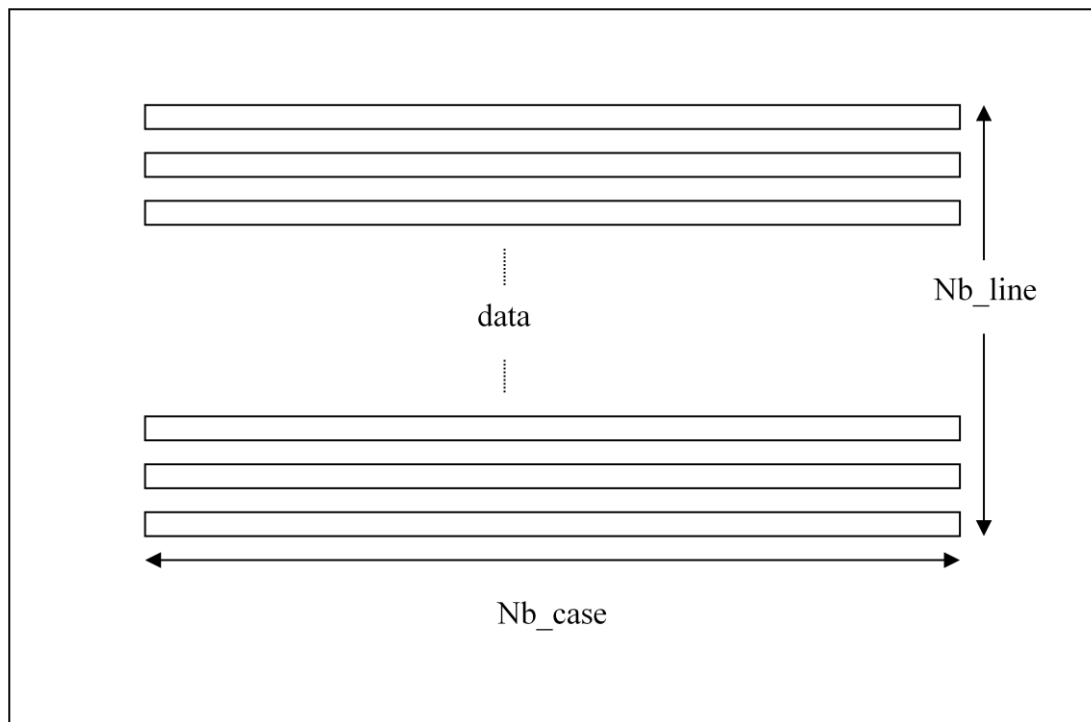


Figure 3-1 : Computing the geographic position of the  $i,j,h$  pixel in red. First identifying the upper and lower layers, then on each layer, from the green points, compute the geographic position of the blue points, interpolate between the two blue points.

### 3.7. Reading the altitude of ambiguity file

This file has the same size as the SLC image and it contains  $Nb\_pixel \times Nb\_ligne$  floats and no header line.



### 3.8. Text file about the ROI information

The text file describe all information about the geographic and radar coordinate of ROI verteses for each reference radar image site: tropi0402 for Paracou is described in ROI\_Paracou\_tropi0402.txt, tropi0201 for Nouragues 1 in ROI\_Nouragues1\_tropi0201.txt, tropi0607 for Nouragues1bis in ROI\_Nouragues1bis\_tropi0607.txt, tropi0303 for Nouragues2 in ROI\_Nouragues2\_tropi0303.txt and tropi0108 for Arbocel in ROI\_Arbocel\_tropi0108.txt.

All of these text file follow the same pattern:



\*Résultat de la transformation de type Standard entre:

\*SYSTEME : Guyane : RGFG95  
 \*COORDONNÉES : Planes  
 \*ELLIPSOÏDE : GRS 1980  
 \*PROJECTION : UTM Nord fuseau 22 (RGFG95)

Header with description of the geographic transformation system

\*SYSTEME : Guyane : RGFG95  
 \*COORDONNÉES : Géographiques  
 \*ELLIPSOÏDE : GRS 1980  
 \*MERIDIEN : Greenwich  
 \*UNITE : Degrés décimaux

\*SYSTEME ALTIMETRIQUE : NGG 1977 (Guyane)

\* Latitude Longitude Hauteur Azimut Range → Indication of the table

\* ROIPPE20  
 4.084722 -52.684441 79.211998 1063.953356 230.310661  
 4.084686 -52.684369 78.762001 1067.265357 234.609542  
 4.084650 -52.684288 77.092003 1070.590142 240.485241  
 4.084614 -52.684207 74.751999 1073.915152 246.933384

N coordinate lines corresponding to points along the boundary vertices

...  
 4.084577 -52.684540 78.942001 1076.665861 224.999980  
 4.084649 -52.684495 79.092003 1070.302995 227.396208  
 4.084722 -52.684441 79.211998 1063.953356 230.310661

All ROIs

\* ROIPPF20  
 4.084362 -52.683648 76.820999 1097.172142 276.027889  
 4.084326 -52.683576 77.611000 1100.483691 279.376910  
 4.084290 -52.683494 77.981003 1103.807734 283.598865

\* ROIPPF21

...

\* ROIGPM11

...

## 4. MORE ABOUT THE GEOCODED DATA

### 4.1. Header file (\*.ent)

In the following, the header file is printed in blue and the explanation in black. The information outlined in red is essential for the analysis.

*# Nom de la carte :*

*Carte.dat= tropi0509\_Pprop\_Hh\_proj\_wgs84.dat*

*# Structure du fichier et codage des pixels*

*# [dans ordre LSBfirst = big-endian]*

*Format\_valeurs\_carte= int\_2*

*Codage\_valeurs\_carte= lin*

The data are coded in unsigned short

*Nb\_case\_par\_ligne\_look= 19271*

number of pixels along the slant range axis

*Nb\_ligne\_look= 10880*

number of lines along the azimuth axis

*Espacement\_entre\_pixel= 1.000000 m*

pixel spacing





.....

*# Parametres nominaux d'amplitude sigma0 :*

*Echelle= linéaire*  
*Pas d'echelle= 0.000400379*  
*Max echelle= 26.2388 (valeur correspondant à +65535)*  
*Min echelle= 0*  
*Max l= 26.2392*

*# Georeferencement des coins de la zone image : [en fait de l'image]*

*ligne colonne Coord géographique WGS84*

*x y Lat Long Alti*  
*[°] degrees [°] degrees [m]*

*Point origine : 0 0 4.5349216376 -52.0697455955 -39.729*

## 4.2. Reading the geocoded data

The header file associated with the geocoded image contains as the first two lines the number of columns and number of lines of the file. It also contains the localisation position of the NW corner and (0,0) pixel of the image, the pixel spacing (in both E-W and N-S directions). The data file does not contain any header and is simply an array of size nb\_case x Nb\_line of unsigned integer ranging from [0,65535]. When no data is available, the pixel has a 0 value.

One can compute the normalised radar cross-section with the following equation:

$$\sigma_0 = 10 \cdot \log_{10} \left( \frac{1}{N_{ROI}} \sum (x * pas\_d\_echelle)^2 \right) \text{ dB}$$

## 4.3. IDL code to read a proj\_WGS84 file from a Linux machine

```
file_image=envi_pickfile(filter='*.dat')
t_y=Nb_ligne_look
t_x=Nb_case_par_ligne_look
openr,1,file_image
out=uintarr(t_y,t_x)
readu,1,out
out=swap_endian(out)
close,1
envi_enter_data,out,bname='map'
```

## 4.4. Localisation of a geocoded image pixel

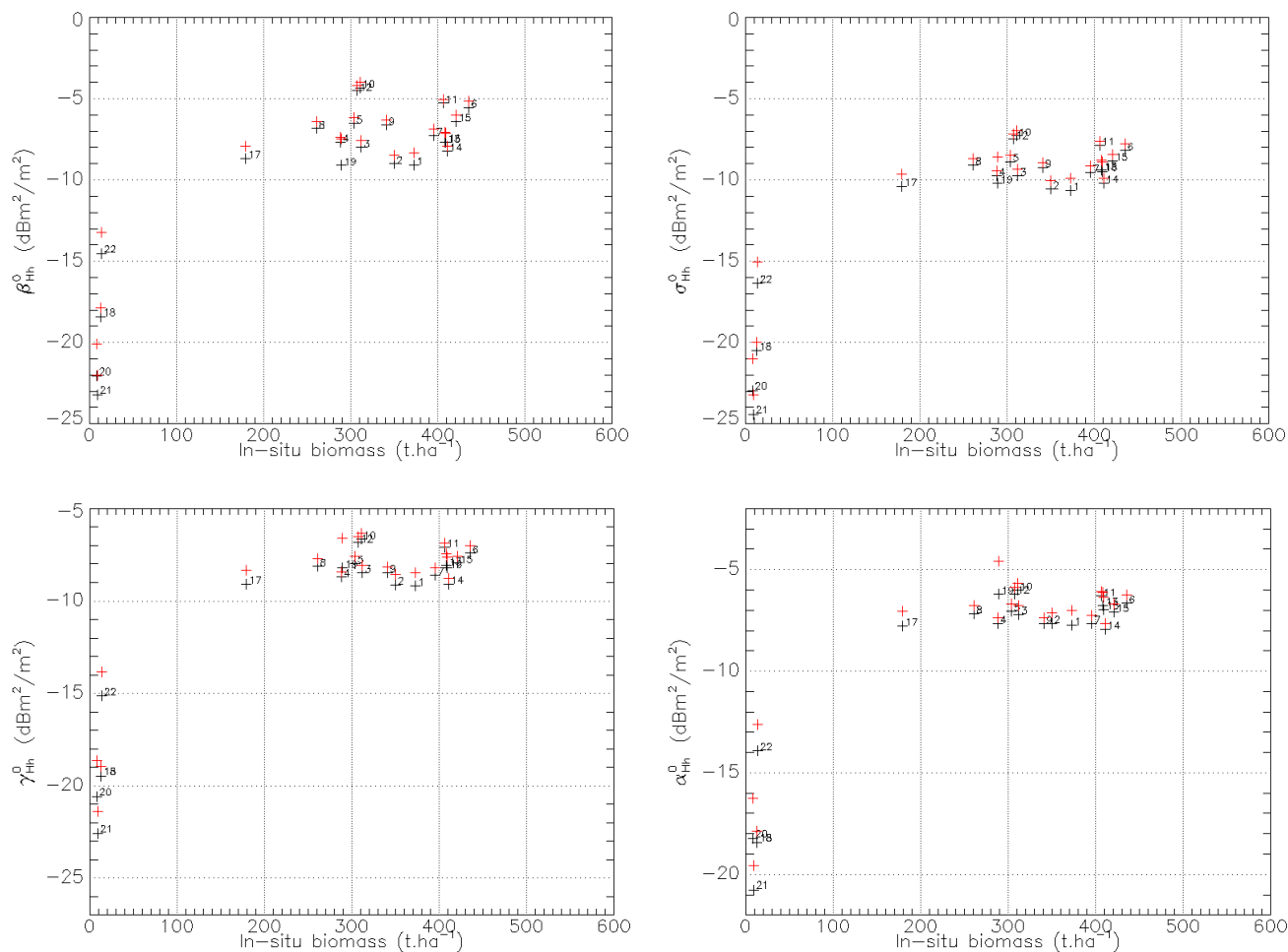
Consider a image pixel (i ,j) and the UTM coordinates in Zone 22 of the (0,0) pixel being E0, N0 (computed from the lat, long geographic coordinates with CIRCE). Then the E,N position of the pixel can be computed as:

$E=E0+i*\text{pixel\_spacing}$  and  $N=N0-j*\text{pixel\_spacing}$



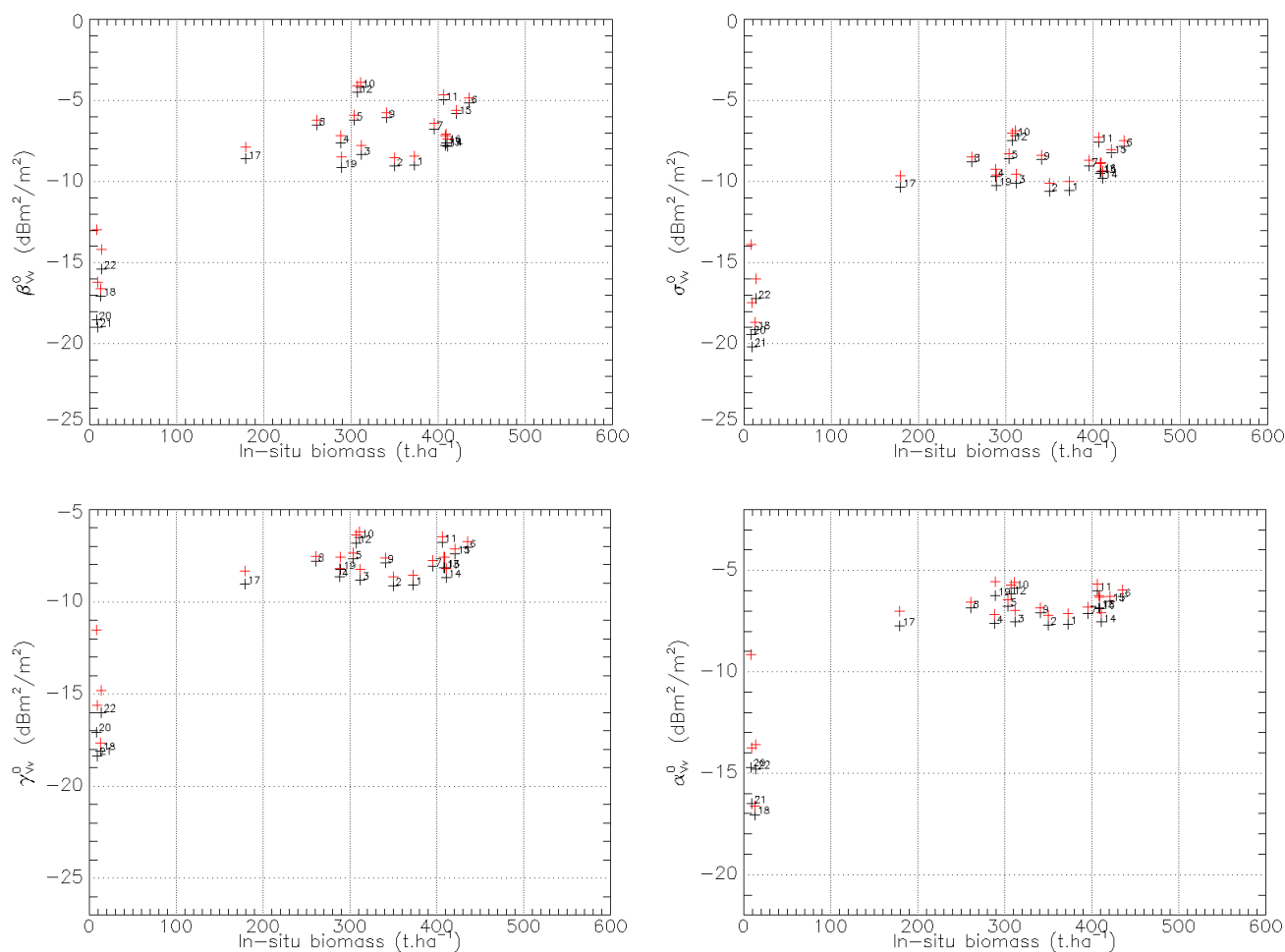
## ANNEX C: BACKSCATTER INTENSITIES VERSUS IN-SITU BIOMASS

**HH-polarized backscattering intensities ( $\beta^0$ ,  $\sigma^0$ ,  $\gamma^0$ , and  $\alpha^0$ ) as function of in-situ biomass for each stand of the Paracou test site.**



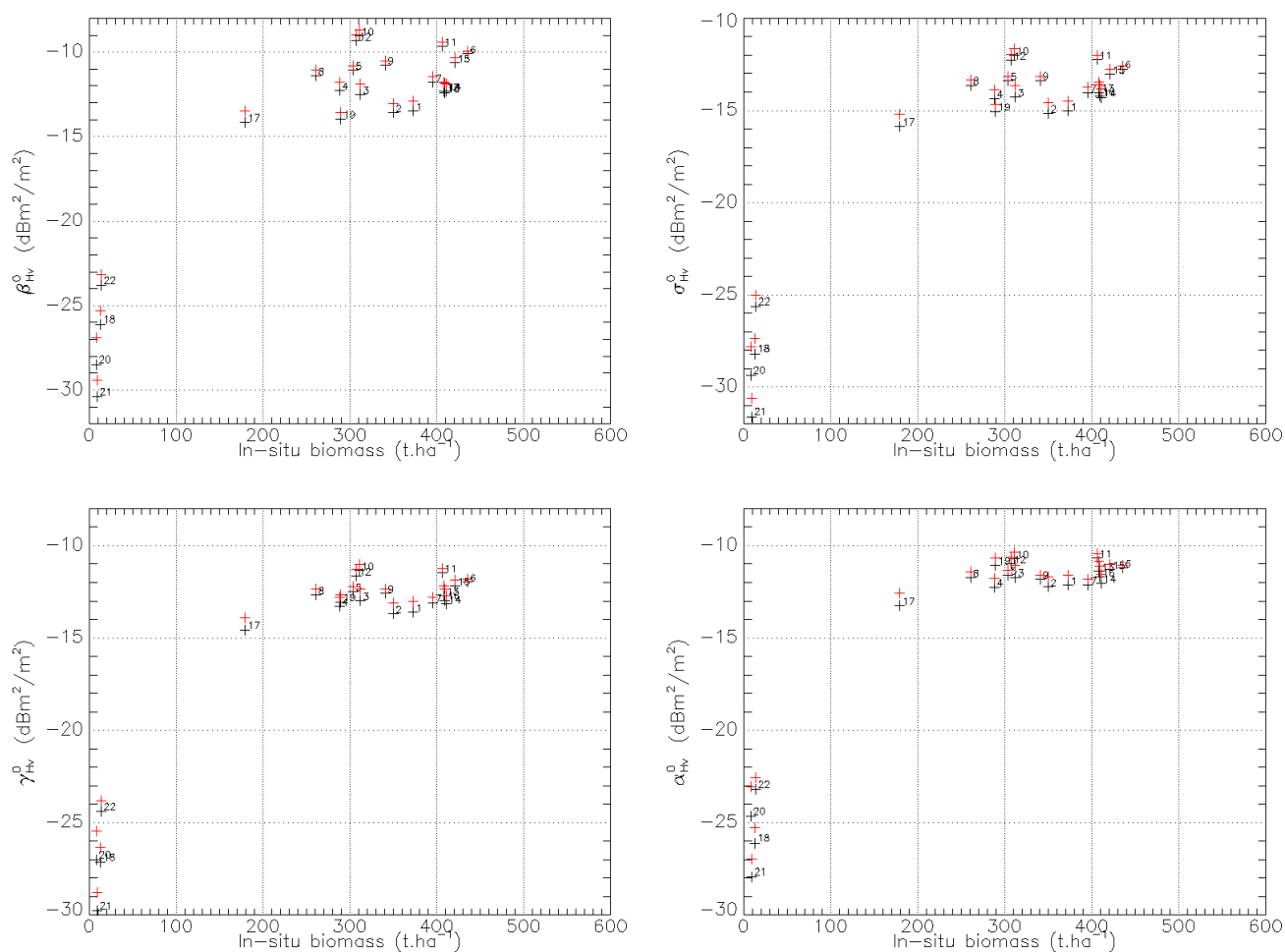


**VV-polarized backscattering intensities ( $\beta^0$ ,  $\sigma^0$ ,  $\gamma^0$ , and  $\alpha^0$ ) as function of in-situ biomass for each stand of the Paracou test site.**





**HV-polarized backscattering intensities ( $\beta^0$ ,  $\sigma^0$ ,  $\gamma^0$ , and  $\alpha^0$ ) as function of in-situ biomass for each stand of the Paracou test site.**







## ANNEX D: ARBORESCENCE OF THE SAR DATABASE

The TropiSAR database is composed of 4 directories:

TropiSAR\_Report:

- TROPISAR\_FINAL\_REPORT\_V2.1.pdf (17/02/2011)
- TROPISAR\_Format\_V1.2.pdf (23/11/2010)

TropiSAR\_In-situ:

- Maps
  - Arbocel/Arbocel\_map.pdf
  - Nouragues/xxx\_map.pdf
  - Paracou/xxx\_map.pdf
- Biomass values
  - Arbocel/Biomass\_Arbocel.xls
  - Nouragues/Biomass\_xxx.xls
  - Paracou/Biomass\_Px.xls
- Summary\_In-situ.xls

TropiSAR\_ROI\_Analysis:

- TropiSAR\_Nouragues.xls
- TropiSAR\_Paracou.xls

TropiSAR\_SARdata:

- Arbocel
  - P-Band
- Nouragues
  - Nouragues1
    - P-Band
      - temporal\_data
      - tomo\_data
  - Nouragues1bis
    - P-Band
  - Nouragues2
    - P-Band
- Paracou
  - P-Band
    - temporal\_data
    - tomo\_data
  - L-Band
    - temporal\_data
    - tomo\_data
- Kaw
  - P-Band
  - L-Band

